Title

A Diaminopropane-Appended Metal-Organic Framework Enabling Efficient CO_2 Capture from Coal Flue Gas via a Mixed Adsorption Mechanism.

Journal

Journal of the American Chemical Society, 139(38)

ISSN

0002-7863

Authors

Milner, Phillip J
Siegelman, Rebecca L
Forse, Alexander C
et al.

Publication Date

2017-09-01

DOI

10.1021/jacs.7b07612

Peer reviewed

JACS
JOURNAL OF THE AMERICAN CHEMICAL SOCIETY
Article
pubs.acs.org/JACS

A Diaminopropane-Appended Metal–Organic Framework Enabling Efficient CO_2 Capture from Coal Flue Gas via a Mixed Adsorption Mechanism

Phillip J. Milner,[†] Rebecca L. Siegelman,[†] Alexander C. Forse,[†,‡,#] Miguel I. Gonzalez,[†] Tomče Runčevski,[†,§] Jeffrey D. Martell,[†] Jeffrey A. Reimer,[#] and Jeffrey R. Long*[,†,#,§]

[†]Department of Chemistry, [‡]Berkeley Energy and Climate Institute, and [#]Department of Chemical and Biomolecular Engineering, University of California—Berkeley, Berkeley, California 94720, United States

[§]Materials Sciences Division, Lawrence Berkeley National Laboratory, Berkeley, California 94720, United States

Supporting Information

ABSTRACT: A new diamine-functionalized metal–organic framework comprised of 2,2-dimethyl-1,3-diaminopropane (dmpn) appended to the Mg^{2+} sites lining the channels of Mg_2(dobpdc) (dobpdc^{4-} = 4,4′-dioxidobiphenyl-3,3′-dicarboxylate) is characterized for the removal of CO_2 from the flue gas emissions of coal-fired power plants. Unique to members of this promising class of adsorbents, dmpn–Mg_2(dobpdc) displays facile step-shaped adsorption of CO_2 from coal flue gas at 40 °C and near complete CO_2 desorption upon heating to 100 °C, enabling a high CO_2 working capacity (2.42 mmol/g, 9.1 wt %) with a modest 60 °C temperature swing. Evaluation of the thermodynamic parameters of adsorption for dmpn–Mg_2(dobpdc) suggests that the narrow temperature swing of its CO_2 adsorption steps is due to the high magnitude of its differential enthalpy of adsorption (Δh_{ads} = −73 ± 1 kJ/mol), with a larger than expected entropic penalty for CO_2 adsorption (Δs_{ads} = −204 ± 4 J/mol·K) positioning the step in the optimal range for carbon capture from coal flue gas. In addition, thermogravimetric analysis and breakthrough experiments indicate that, in contrast to many adsorbents, dmpn–Mg_2(dobpdc) captures CO_2 effectively in the presence of water and can be subjected to 1000 humid adsorption/desorption cycles with minimal degradation. Solid-state ^{13}C NMR spectra and single-crystal X-ray diffraction structures of the Zn analogue reveal that this material adsorbs CO_2 via formation of both ammonium carbamates and carbamic acid pairs, the latter of which are crystallographically verified for the first time in a porous material. Taken together, these properties render dmpn–Mg_2(dobpdc) one of the most promising adsorbents for carbon capture applications.

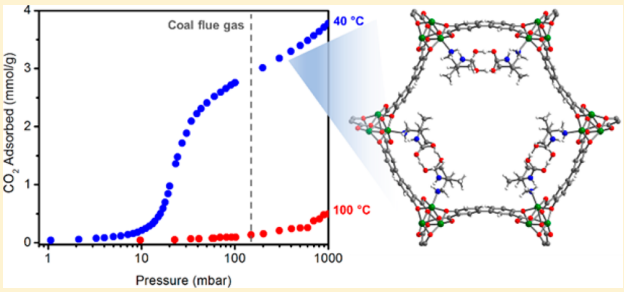

INTRODUCTION

Rising atmospheric levels of greenhouse gases, primarily CO_2, are linked to global climate change.[1] In particular, the combustion of coal for energy generation accounts for approximately 30% of global CO_2 emissions.[2] Despite this, coal is projected to remain a major energy source in the near future, especially in rapidly industrializing nations.[2,3] Therefore, postcombustion carbon capture and sequestration (CCS) from coal flue gas, which consists of CO_2 (15–16%), O_2 (3–4%), H_2O (5–7%), N_2 (70–75%), and trace impurities (e.g., SO_x, NO_x) at ambient pressure,[4] is a key strategy needed to reduce global CO_2 emissions during the transition to cleaner energy sources.[1,5] Because 60–70% of the cost of CCS is accrued during the CO_2 separation stage, the development of improved adsorbents for carbon capture stands to limit substantially the rise in cost of electricity upon implementation of CCS.[6] Specifically, a temperature swing adsorption (TSA) process requires an adsorbent that (i) selectively adsorbs CO_2 under typical coal flue gas conditions (150 mbar of CO_2 at 40 °C), (ii) captures 90% of the CO_2 from the stream, (iii) is regenerable at low temperatures under pure CO_2 to minimize regeneration costs, (iv) displays fast adsorption/desorption kinetics, and (v) possesses long-term stability to both water and adsorption/desorption cycling.[6b,7]

The most widely employed sorbents for CCS are aqueous solutions of organic amines, such as monoethanolamine (MEA), which selectively react with CO_2 to form ammonium carbamate and/or bicarbonate species.[6a,8] However, amine solutions are prone to oxidative and thermal degradation[8a,9] and suffer from low CO_2 working capacities, contributing to an untenable increase in the cost of electricity if employed for CCS.[6,10] To address these issues, solid adsorbents, including porous carbons, silicas, zeolites, and metal–organic frameworks, have been investigated as promising alternatives due to their high thermal stabilities and potentially lower regeneration

Received: July 20, 2017
Published: September 14, 2017

DOI: 10.1021/jacs.7b07612
J. Am. Chem. Soc. 2017, 139, 13541–13553

energies.[5a,7,11] Extensive studies have revealed that most of these adsorbents are not applicable for CCS due to hydrolytic instability and/or competitive binding of water to the CO_2 adsorption sites.[11a,c−g,12,13] On the other hand, amine-functionalized adsorbents[11b,d,f,g,14] can offer both high CO_2 selectivity and enhanced performance under humid conditions,[12b,14b,15] but they often exhibit slow adsorption kinetics[12b] and require high regeneration temperatures. Thus, there remains an ongoing need for new adsorbents that perform well under humid conditions and can be regenerated at moderate temperatures under pure CO_2.

Recently, we[16] and others[17] have investigated a new class of amine-functionalized adsorbents prepared by appending diamines to the open metal sites of metal−organic frameworks. Remarkably, alkylethylenediamine-appended variants of Mg_2(dobpdc) (dobpdc^{4-} = 4,4′-dioxidobiphenyl-3,3′-dicarboxylate),[16a−c,17a−c] a metal−organic framework possessing hexagonal one-dimensional channels lined with coordinatively unsaturated Mg^{2+} sites, adsorb CO_2 via a unique cooperative mechanism involving the formation of ammonium carbamate chains (Figure 1).[16a,b] This cooperative adsorption leads to

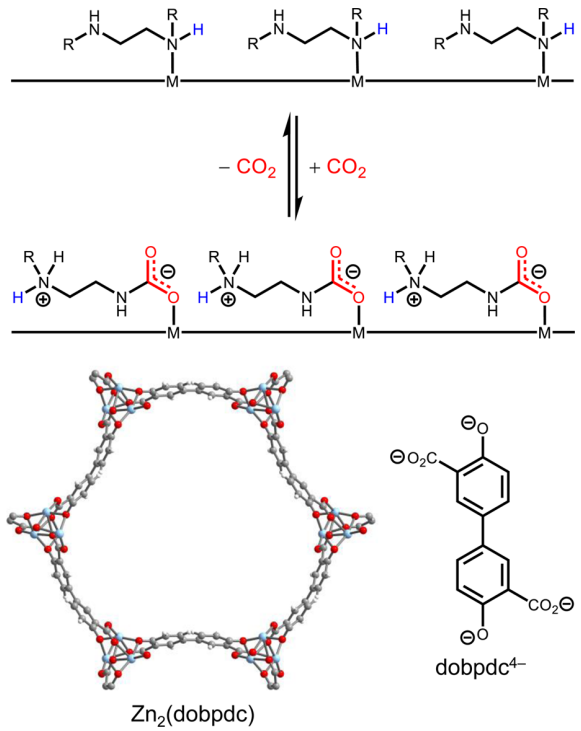

Figure 1. General structure of alkylethylenediamine-appended variants of M_2(dobpdc) (dobpdc^{4-} = 4,4′-dioxidobiphenyl-3,3′-dicarboxylate), represented by the single-crystal X-ray diffraction structure of the Zn framework, which cooperatively adsorb CO_2 via the formation of ammonium carbamate chains. Light blue, blue, red, gray, and white spheres represent Zn, N, O, C, and H, respectively.

step-shaped isotherms that enable high working capacities in a TSA process (Figure 2).[16a,b] In addition, previous mixed-gas equilibrium adsorption measurements indicate that these materials maintain their high capacity for CO_2 under humid conditions, a critical challenge for carbon capture.[12b,16b,17a]

Owing to their highly exothermic differential enthalpies of adsorption, Mg_2(dobpdc) variants appended with *primary−secondary* (1°, 2°),[16a] *secondary−secondary* (2°, 2°),[16a−c] and

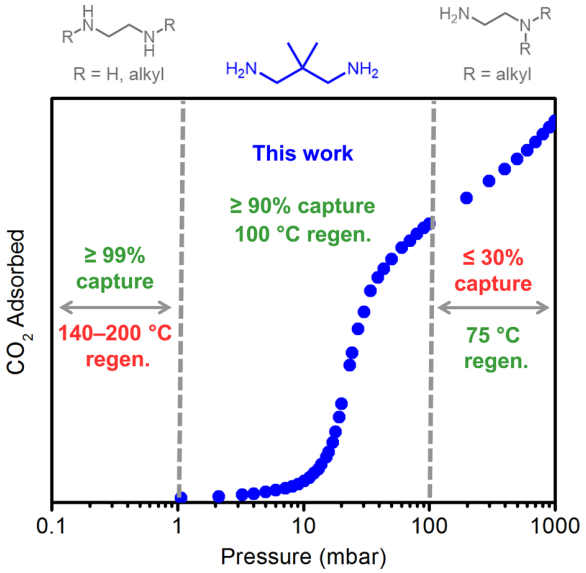

Figure 2. Summary of 40 °C CO_2 step pressures and regeneration temperatures under 1 bar of CO_2 for alkyldiamine-appended variants of Mg_2(dobpdc).

most *primary−primary* (1°, 1°)[17a,c] alkylethylenediamines display step-shaped adsorption of CO_2 at very low partial pressures (≤1 mbar of CO_2 at 40 °C) (Figure 2). As a result of their low step pressures, these adsorbents are well-suited for carbon capture from dilute streams such as air.[16a,c,17c] However, this strong adsorption results in high desorption temperatures under pure CO_2 (140−200 °C), which greatly increases the regeneration costs associated with the use of these adsorbents. In contrast, *primary−tertiary* (1°, 3°) diamine-appended variants of Mg_2(dobpdc) can be regenerated at lower temperatures (75 °C), but due to their relatively high step pressures (≥100 mbar, 40 °C) they would capture only ≤30% of the CO_2 from a coal flue gas stream (Figure 2).[16a,17b] A promising adsorbent would display step-shaped adsorption at ∼15 mbar of CO_2 at 40 °C to enable 90% capture from a coal flue gas stream containing 150 mbar of CO_2 and minimal adsorption under 1 bar of CO_2 at ≤100 °C to enable regeneration of the CO_2-saturated bed with lower grade steam. More specifically, the ideal adsorbent would possess a free energy of adsorption (Δg_{ads}) as close as possible to that required for a CO_2 adsorption step (p_{step}) at 15 mbar at 40 °C [−10.9 kJ/mol, as determined from $\Delta g_{ads} = RT \ln(p_{step}/p_0)$ with p_0 = 1 bar],[16a] which will enable effective capture of CO_2 while the energy required for desorption is minimized. None of the alkylethylenediamine-appended variants of Mg_2(dobpdc) reported to date meet these criteria.[16a−c,17a−c] Herein, we demonstrate that Mg_2(dobpdc) appended with 2,2-dimethyl-1,3-diaminopropane (dmpn, Figure 2) possesses these desirable attributes, along with excellent long-term stability and performance under humid conditions. Altogether, these characteristics make dmpn−Mg_2(dobpdc) one of the most promising adsorbents identified to date for CCS from coal flue gas.

■ EXPERIMENTAL SECTION

General Procedures. All synthetic manipulations were carried out under air unless noted otherwise. All diamines and solvents were purchased from commercial sources and used without further purification. The ligand H_4dobpdc was purchased from Hangzhou Trylead Chemical Technology Co. The metal−organic frameworks

DOI: 10.1021/jacs.7b07612
J. Am. Chem. Soc. 2017, 139, 13541−13553

M_2(dobpdc) (M = Mg, Mn, Co, Ni, Zn) were prepared according to modified literature procedures, as detailed in the Supporting Information (SI).[16a,b] Powder X-ray diffraction patterns (Figure S1, SI) and 77 K N_2 adsorption isotherms (Figure S2, SI) for these materials are consistent with those from the literature.[16a,b] ^{1}H NMR spectra for digestion experiments were collected on a Bruker AMX 300 MHz NMR spectrometer and referenced to residual DMSO (δ 2.50 ppm). Attenuated total reflectance (ATR) infrared (IR) spectra were collected on a PerkinElmer Spectrum 400 Fourier transform (FT) IR spectrometer. Differential scanning calorimetry (DSC) measurements were carried out using a TA Instruments Q200 differential scanning calorimeter. Laboratory powder X-ray diffraction patterns were collected using a Bruker AXS D8 Advance diffractometer using Cu Kα radiation (λ = 1.5418 Å).

Synthesis of Diamine-Appended M_2(dobpdc) (M = Mg, Ni) Compounds.[16a] A 20 mL scintillation vial was charged with 4 mL of toluene and 1 mL of the diamine (for 2,2-dimethyl-1,3-diaminopropane, the diamine was melted prior to use). Methanol-solvated M_2(dobpdc) (~20 mg, M = Mg or Ni) was filtered and washed with successive aliquots of toluene (2 × 10 mL). [Note: M_2(dobpdc) should not be allowed to dry completely as this can in some cases lead to decomposition of the framework.[16c]] Next, M_2(dobpdc) was added to the diamine solution, and the vial was swirled several times and allowed to stand at room temperature for 24 h. The mixture was then filtered, and the resulting powder was thoroughly washed with toluene (3 × 20 mL) and allowed to dry for 2 min, yielding ~30 mg of the diamine-appended metal−organic framework. In all cases, ^{1}H NMR digestion experiments (Supporting Information, section S5) confirmed that the ratios of diamine to Mg^{2+} sites were >100% (Table S2, SI), indicative of solvation by excess diamine. Activation of the samples at 130−150 °C for 20−30 min under flowing N_2 was sufficient to remove the excess diamine from the pores. A modified procedure[15b] was used to prepare small-scale samples of dmpn-appended M_2(dobpdc) (M = Mn, Co, Zn) (see the Supporting Information for details). Powder X-ray diffraction patterns, infrared spectra, pure CO_2 adsorption/desorption isobars, and thermogravimetric N_2 decomposition curves for all new diamine-appended metal−organic frameworks prepared in this work are included in sections 2−4 of the Supporting Information.

Single-Crystal and Powder X-ray Diffraction Structures. Details of powder X-ray diffraction refinements are included in section 10 of the Supporting Information. Single crystals of Zn_2(dobpdc) and diamine-appended analogues were prepared according to modified literature procedures.[16a] Additional details and structures are included in section 11 of the Supporting Information.

Gas Adsorption Measurements. Adsorption isotherms of N_2, O_2, CO_2, and H_2O were obtained by volumetric methods using a Micromeritics ASAP 2020 gas adsorption analyzer. All gases were 99.998% pure or higher. Deionized water was subjected to three freeze−pump−thaw cycles prior to adsorption measurements. Isotherms conducted at 25, 30, 40, 50, 60, and 75 °C were measured using a circulating water bath. Isotherms at 100 °C were measured using a heated sand bath equipped with a programmable temperature controller. Samples were regenerated at 100 °C under dynamic vacuum (<10 μbar) for 2−4 h between isotherms. The isotherm data points were considered equilibrated after <0.01% pressure change occurred over a 15 s interval.

Calculations of Differential Enthalpies and Entropies of Adsorption. Isotherms were fit by linear interpolation. Using the isotherm fits, the exact pressures (p_q) corresponding to specific CO_2 loadings (q) were determined at different temperatures (T). The Clausius−Clapeyron relationship (eq 1) was used to calculate the differential enthalpies of adsorption (Δh_{ads}) based on the slopes of the linear trendlines fit to $\ln(p_q)$ vs $1/T$ at constant values of q. The y-intercepts of these linear trendlines are equal to $-\Delta s_{ads}/R$ at each loading (with p_0 = 1 bar),[18] and thus were used to determine the corresponding differential entropies of adsorption.

$$\ln(p_q) = \left(\frac{\Delta h_{ads}}{R}\right)\left(\frac{1}{T}\right) + c \quad (1)$$

Thermogravimetric Analysis and Cycling Measurements. Dry thermogravimetric analysis (TGA) experiments were conducted using a TA Instruments TGA Q5000. Humid TGA experiments were conducted using a TA Instruments TGA Q50. The incident gas stream was humidified by passing it through two water bubblers in series, leading to an estimated water content of 1.3% at 25 °C (as determined by comparison to water isotherms). Isobars were measured using a temperature ramp rate of 1 °C/min. Custom CO_2/N_2 blends (50%, 30%, 15%, 10%, and 5% CO_2 in N_2) were purchased from Praxair. Samples were activated at 130 or 150 °C under flowing N_2 for 20−30 min (until the mass stabilized) prior to switching the gas stream. Masses are uncorrected for buoyancy effects. Decomposition experiments were carried out under dry N_2 using a temperature ramp rate of 1.5 °C/min.

Breakthrough Measurements. See section 7 of the Supporting Information for complete experimental details.

Solid-State Magic Angle Spinning (MAS) ^{13}C NMR Experiments. For NMR experiments performed on samples dosed with $^{13}CO_2$ (Sigma-Aldrich, 99 atom % ^{13}C, <3 atom % ^{18}O), samples were first activated under flowing N_2 at the temperatures indicated in Table S2 (SI) for 30 min, cooled to room temperature, and transferred to a N_2-filled glovebag. The samples were then packed into rotors. Uncapped rotors were then evacuated for at least 30 min inside a home-built gas-dosing manifold before dosing with $^{13}CO_2$, after which the samples were allowed to equilibrate for 30 min (see Supporting Information, section 8, for further details). All NMR spectra were recorded at 7.1 T using a DOTY magic angle spinning probe with a 4 mm silicon nitride rotor. A Tecmag Discovery spectrometer capable of double-resonance experiments was used. ^{13}C NMR spectra were acquired by cross-polarization from ^{1}H with a contact time of 1 ms and with continuous-wave ^{1}H decoupling during the acquisition period. All ^{13}C NMR spectra were referenced using the tertiary carbon atom of adamantane with a chemical shift of 38.5 ppm (secondary reference). Sample dosing and NMR experiments were carried out at ambient temperature.

■ RESULTS AND DISCUSSION

Discovery and Evaluation of dmpn−Mg_2(dobpdc). Our previous work demonstrated that modifying the nitrogen substituents of diamines allows for rational tuning of the CO_2 step pressure for alkylethylenediamine-appended variants of Mg_2(dobpdc).[16a] However, as summarized in Figure 2, changing the substitution patterns on the nitrogen atoms led to step pressures that were either too high (≥100 mbar) or too low (≤1 mbar) for the efficient removal of CO_2 from coal flue gas. Therefore, we examined whether changing the substituents on the backbone of the diamine—specifically, switching from ethylenediamines to diaminopropanes—could tune the step pressure to ~15 mbar at 40 °C. To this end, we appended 1,3-diaminopropane (pn; Figure 3) to Mg_2(dobpdc), which produced an adsorbent displaying step-shaped adsorption of CO_2 with a similar step pressure (~0.5 mbar, 40 °C) as compared to other strongly adsorbing diamine-appended variants of Mg_2(dobpdc) (Figure 3a).[16a−c,17a,c] However, in distinct contrast to variants of Mg_2(dobpdc) functionalized with *primary−primary* ethylenediamines (Figure S21, SI),[17a,c] pn−Mg_2(dobpdc) displays almost no hysteresis upon CO_2 desorption, allowing for its near complete regeneration at 130 °C under pure CO_2 (Figure 3b). The addition of a methyl group (2-methyl-1,3-diaminopropane, mpn) to the diamine backbone does not have a significant effect on the CO_2 adsorption step pressure or temperature compared to those of pn−Mg_2(dobpdc) (Figure 3).

Unexpectedly, with the addition of a second methyl group to the diamine backbone, 2,2-dimethyl-1,3-diaminopropane (dmpn) led to a drastic change in the adsorption properties

DOI: 10.1021/jacs.7b07612
J. Am. Chem. Soc. 2017, 139, 13541−13553

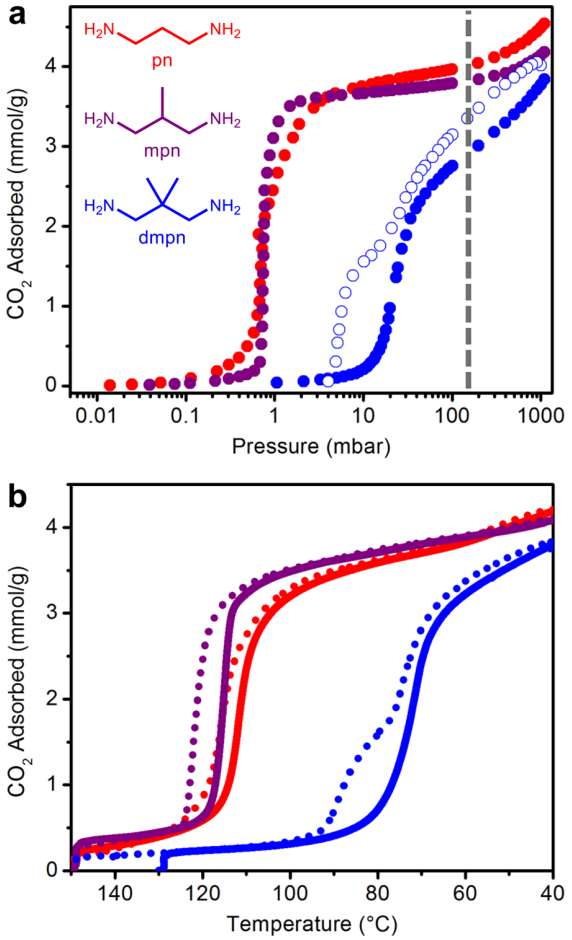

Figure 3. (a) Isotherms for the adsorption of CO_2 at 40 °C CO_2 in pn−, mpn−, and dmpn−Mg_2(dobpdc) (desorption data shown with open circles). The dashed line indicates the approximate partial pressure of CO_2 in coal flue gas (150 mbar). (b) Adsorption (solid) and desorption (dotted) isobars of pn− (red), mpn− purple), and dmpn−Mg_2(dobpdc) (blue) under pure CO_2, as measured by thermogravimetric analysis.

(Figure 3). For this adsorbent, the CO_2 adsorption step at 40 °C is broadened and shifted to a pressure of ∼15 mbar, which is suitable for ∼90% capture of CO_2 from coal flue gas (Figure 3a). In addition, near-complete CO_2 desorption can be achieved at 95 °C under pure CO_2 (Figure 3b), although an unusual hysteresis profile is apparent during desorption. This low CO_2 desorption temperature is particularly advantageous because the regeneration temperature of the adsorbent strongly affects the efficiency of a carbon capture process.[19] During the preparation of this paper, a similar substituent effect was disclosed for ethylenediamine-appended variants of Mg_2(dobpdc).[17a] Although the adsorbent functionalized with the ethylenediamine analogue of dmpn, 1,1-dimethyl-1,2-ethylenediamine (den; referred to herein as dmen), displays a similar pure CO_2 adsorption step temperature, it possesses a lower CO_2 capacity and a higher CO_2 desorption temperature of 116 °C due to significant hysteresis (see section 3 of the Supporting Information for details).[17a]

The ability of dmpn−Mg_2(dobpdc) to effectively capture CO_2 at 40 °C while showing minimal adsorption under 1 bar CO_2 at 95 °C led us to further examine its potential for carbon capture from coal flue gas. Accordingly, CO_2 adsorption isotherms were collected at a range of temperatures from 25 to 100 °C (Figure 4). At temperatures ≤75 °C, step-shaped

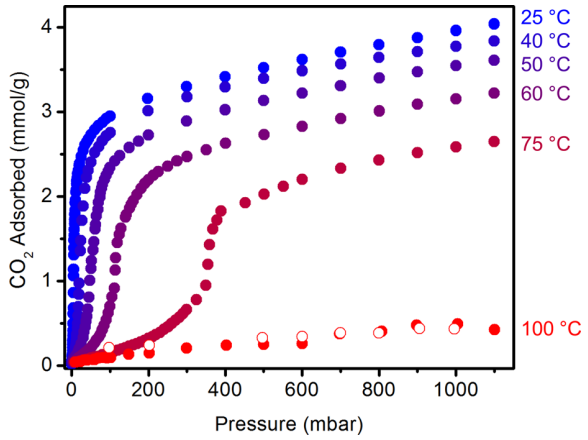

Figure 4. Isotherms for the adsorption of CO_2 at 25, 40, 50, 60, 75, and 100 °C in dmpn−Mg_2(dobpdc) (desorption data at 100 °C shown with open circles).

adsorption of CO_2 is apparent, with the step occurring at higher pressures as the temperature increases. Consistent with the isobaric data (Figure 3b), the CO_2 isotherm for dmpn−Mg_2(dobpdc) at 100 °C is nearly flat up to a pressure of 1 bar. On the basis of the single-component isotherm data of dmpn−Mg_2(dobpdc), adsorption at 150 mbar of CO_2 at 40 °C (2.91 mmol/g, 11 wt %) and desorption under 1 bar of CO_2 at 100 °C (0.49 mmol/g, 1.9 wt %) produce a high working capacity of 2.42 mmol/g (9.1 wt %) with only a 60 °C temperature swing. Using the crystallographic density of activated dmpn−Mg_2(dobpdc) (0.94 g/cm^3), this corresponds to an approximate volumetric working capacity of 2.28 mmol/cm^3 (51 v/v).

Surprisingly, the height and sharpness of the CO_2 adsorption steps were also affected by temperature, with sharper, taller steps observed at lower temperatures and broader, shorter steps observed at higher temperatures. Similar behavior was observed in isobaric adsorption measurements of dmpn−Mg_2(dobpdc) using gas streams with decreasing partial pressures of CO_2 (Figure S10, SI). In contrast, other adsorbents in this family,[16a−c,17a−c] such as closely related mpn−Mg_2(dobpdc), exhibit CO_2 adsorption steps of equivalent height regardless of the temperature in isothermal measurements (Figure S12, SI) or the partial pressure of CO_2 in isobaric measurements (Figure S15, SI). The fundamentally different response of the CO_2 adsorption step heights of dmpn−Mg_2(dobpdc) to changing conditions compared to other diamine-appended variants of Mg_2(dobpdc) suggests that it adsorbs CO_2 by a different mechanism, as will be discussed in detail below.

The CO_2 adsorption isotherms at 40, 50, and 60 °C in Figure 4 were fit empirically using linear interpolation (Figure S7, SI), which allowed the differential enthalpy of adsorption to be determined at each CO_2 loading using the Clausius−Clapeyron relationship (Figure S8, SI). At a CO_2 loading of 1 mmol/g (i.e., in the adsorption step), a differential enthalpy of adsorption (Δh_{ads}) of −74 ± 1 kJ/mol was determined for dmpn−Mg_2(dobpdc), which is comparable to that of other diamine-appended variants of Mg_2(dobpdc)[16a] as well as mpn−Mg_2(dobpdc) (−71 ± 4 kJ/mol, Figure S13, SI) and pn−Mg_2(dobpdc) (−76 ± 2 kJ/mol, Figure S17, SI). Using the low reversible heat capacity (1.5 J/g·°C) of dmpn−Mg_2(dobpdc)

DOI: 10.1021/jacs.7b07612
J. Am. Chem. Soc. 2017, 139, 13541−13553

(Figure S28, SI), an approximate regeneration energy of 2.1 MJ/kg CO_2 was calculated (see section 6 of the Supporting Information for details). This value is approximately half that required to regenerate a 30% monoethanolamine solution (4.8 MJ/kg CO_2),[20] less than that for zeolite 5A (approximately 3.2 MJ/kg CO_2),[21] and similar to that of *N,N′*-dimethylethylenediamine−Mg_2(dobpdc) (2.3 MJ/kg CO_2).[16b] However, all of these adsorbents must be heated to significantly higher temperatures (120,[20] 150,[21] and 140 °C,[16a] respectively) than dmpn−Mg_2(dobpdc) (100 °C) to fully desorb CO_2. Notably, dmpn−Mg_2(dobpdc) also adsorbs only negligible amounts of N_2 (0.017 mmol/g at 750 mbar) and O_2 (0.002 mmol/g at 40 mbar) at 40 °C, leading to excellent CO_2/N_2 (882) and CO_2/O_2 (517) noncompetitive selectivities at the partial pressures relevant for a coal flue gas stream (Figure S11 and Table S1, SI).[11d]

The similar differential enthalpies of CO_2 adsorption in dmpn−, mpn−, and pn−Mg_2(dobpdc) are surprising given the significantly higher step pressure of dmpn−Mg_2(dobpdc), as our previous work suggested that the differential enthalpy should dictate the CO_2 step pressure.[16a,b] We previously observed that the differential enthalpies and entropies of adsorption at a loading of 1 mmol/g (i.e., in the step) are linearly correlated for alkylethylenediamine-functionalized variants of Mg_2(dobpdc) (gray circles, Figure 5; see Table S3 for individual values).[16a] In this plot, isothermal CO_2 step pressures decrease moving toward the upper right corner, as indicated by both stronger CO_2 binding (more negative Δh_{ads}) and reduced CO_2 and diamine mobility (more negative Δs_{ads}) in the adsorbed phase. Both mpn−Mg_2(dobpdc) and pn−Mg_2(dobpdc) obey this relationship and possess 40 °C step pressures (~0.5 mbar) similar to those of adsorbents with comparable differential enthalpies of adsorption.[16a,b]

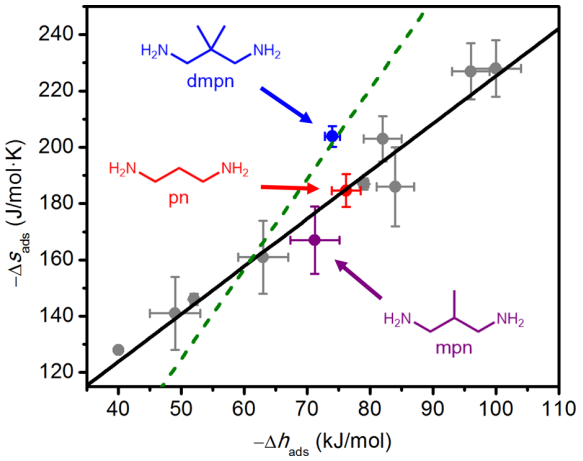

Figure 5. Correlation between the negative differential enthalpy ($-\Delta h_{ads}$) and negative differential entropy ($-\Delta s_{ads}$) of CO_2 adsorption in diamine-appended variants of Mg_2(dobpdc). The adsorbents mpn−Mg_2(dobpdc) (purple circle), pn−Mg_2(dobpdc) (red circle), and previously reported ethylenediamine-appended variants (gray circles)[16a,17a] follow a linear relationship, whereas dmpn−Mg_2(dobpdc) (blue circle) is an outlier. The dashed green line indicates the combinations of Δh_{ads} and Δs_{ads} that yield Δg_{ads} = −10.9 kJ/mol, corresponding to p_{step} = 15 mbar at 40 °C, thus enabling a 90% capture rate from a coal flue gas stream.

Performing the same analysis for dmpn−Mg_2(dobpdc), however, revealed it to be an outlier from this trend (black line, Figure 5), as it possesses a more negative differential entropy of adsorption (Δs_{ads} = −204 ± 4 J/mol·K) than expected given its highly exothermic differential enthalpy of adsorption (Δh_{ads} = −74 ± 1 kJ/mol). This increase in the entropic penalty for CO_2 adsorption in dmpn−Mg_2(dobpdc) over what would be predicted from the linear trendline followed by other alkyldiamines (−181 J/mol·K) leads to a Δg_{ads} at 40 °C of −10 ± 2 kJ/mol. Importantly, this value is within the error of the Δg_{ads} calculated to be necessary to achieve step-shaped adsorption of CO_2 at 15 mbar and 40 °C (−10.9 kJ/mol), as indicated by its position on the dashed green line in Figure 5. Although dmen−Mg_2(dobpdc)[17a] also lies on this line, it exhibits a less negative Δh_{ads} (−63 ± 4 kJ/mol) than dmpn−Mg_2(dobpdc) (−74 ± 1 kJ/mol), which contributes to the larger temperature swing (ΔT = 76 °C) required to move the adsorption step past 1 bar of CO_2 (eq 1). The significant change in the differential entropy of adsorption between dmpn−Mg_2(dobpdc) and mpn−Mg_2(dobpdc) and pn−Mg_2(dobpdc) predominantly accounts for the difference in step pressures between these adsorbents at 40 °C (Figure 3a). Notably, this represents a rare instance in which the adsorption properties of a material have been tuned by changing the differential entropy of adsorption.

Performance under Humid Flue Gas Conditions. Although dmpn−Mg_2(dobpdc) shows promising properties in single-component measurements, assessing its performance for carbon capture under humid conditions is imperative due to the high water content (5−7%) of coal flue gas. In general, materials bearing open metal coordination sites adsorb water and CO_2 at the same binding sites, with more favorable adsorption of water, generally leading water to outcompete CO_2 in multicomponent measurements.[12a,b,22] In contrast, isothermal measurements confirm that the average differential heat of adsorption for water in dmpn−Mg_2(dobpdc) is −47 ± 1 kJ/mol (Figures S29 and S30, SI), which is less negative than that for CO_2 (−73 ± 1 kJ/mol) due to the different binding modes of these two adsorbates. However, these single-component measurements do not necessarily reflect the ability of dmpn−Mg_2(dobpdc) to competitively adsorb CO_2 under humid conditions.

Multicomponent measurements of CO_2 adsorption in the presence of water are more informative for evaluating the potential of dmpn−Mg_2(dobpdc) for carbon capture.[12b] Therefore, we performed humid thermogravimetric analysis (TGA) measurements by bubbling the incident gas stream through water to study the ability of dmpn−Mg_2(dobpdc) to adsorb CO_2 under humid conditions (Figure 6). One drawback of these measurements is that the exact composition of gases adsorbed cannot be reliably determined, although comparison of the mass changes observed with different gas streams provides insight into the behavior of the adsorbent under dry and humid conditions. Consistent with isothermal data (Figure S11, SI), dmpn−Mg_2(dobpdc) adsorbs a negligible amount of dry N_2 at 40 °C (dark blue, Figure 6). Therefore, N_2 coadsorption can assumed to be negligible in these multicomponent measurements. Cooling dmpn−Mg_2(dobpdc) below 60 °C under a humid N_2 stream led to an increase in mass relative to the dry N_2 isobar. The difference between the dry and humid N_2 cooling isobars should primarily be due to water adsorption and suggests that 1.58 g of water per 100 g of adsorbent (0.22 molecules per diamine) are taken up at 40 °C in the absence of CO_2.[23] Importantly, step-shaped adsorption of H_2O was not observed in this assay, suggesting that any step-

DOI: 10.1021/jacs.7b07612
J. Am. Chem. Soc. 2017, 139, 13541−13553

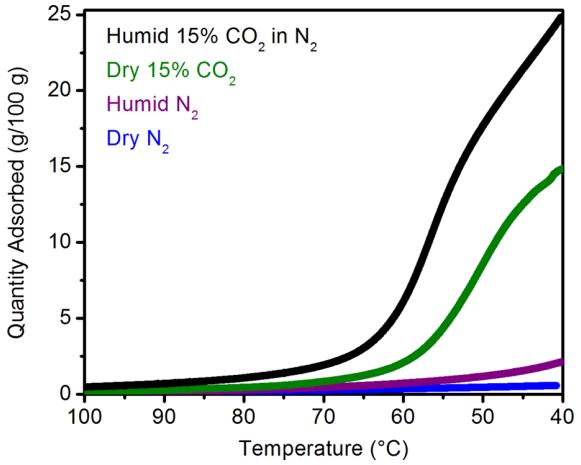

Figure 6. Humid 15% CO_2 in N_2 (black), dry 15% CO_2 in N_2 (green), humid N_2 (purple), and dry N_2 (dark blue) isobars for dmpn−Mg_2(dobpdc), as determined by thermogravimetric analysis (TGA).

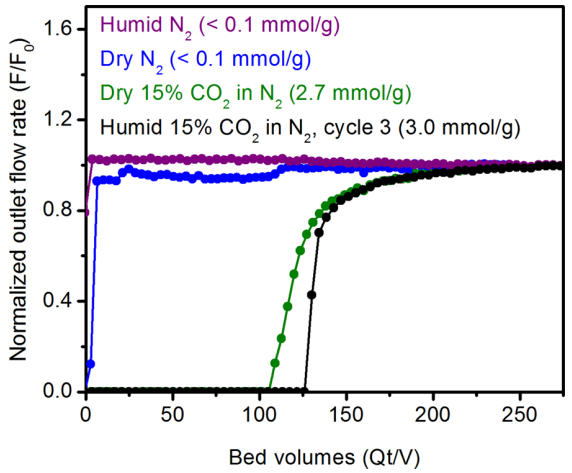

Figure 7. Dry and humid 15% CO_2 in N_2 breakthrough measurements with dmpn−Mg_2(dobpdc). Breakthrough of N_2 under dry (blue) and humid (purple) conditions occurred nearly immediately, followed by clean breakthrough of CO_2 under both dry (green) and humid (black) conditions.

shaped adsorption observed with humidified CO_2 streams results from CO_2 adsorption.

Cooling dmpn−Mg_2(dobpdc) under a stream of dry 15% CO_2 in N_2 led to step-shaped adsorption of CO_2 (green, Figure 6), with a CO_2 uptake of 14.3 g/100 g (3.24 mmol/g) at 40 °C. This is comparable to the 2.91 mmol/g of CO_2 adsorbed at 150 mbar in the 40 °C isotherm (Figure 3a). Significantly, step-shaped adsorption was also observed upon cooling dmpn−Mg_2(dobpdc) under humid 15% CO_2 in N_2 (light blue), suggesting that CO_2 capture in dmpn−Mg_2(dobpdc) occurs readily in the presence of water. The apparent CO_2 adsorption step of dmpn−Mg_2(dobpdc) shifted to a slightly higher temperature under the humid gas stream, indicating that water promotes CO_2 adsorption. The same increase in apparent CO_2 adsorption step temperature was observed with humidified pure CO_2 and 5% CO_2 in N_2 streams (Figures S32 and S33, SI). This effect is likely due to water stabilizing the CO_2 adsorbed phase through hydrogen-bonding or ion−dipole interactions, as has been observed with other amine-functionalized materials.[15,24] Consistent with this hypothesis, dmpn−Mg_2(dobpdc) exhibits a greater increase in mass after the adsorption step under humid conditions compared to dry conditions. This increased uptake suggests that dmpn−Mg_2(dobpdc) coadsorbs significantly more water after CO_2 adsorption, leading to an additional uptake of 9.98 g/100 g (5.55 mmol/g if all water, see below) at 40 °C under humid 15% CO_2 in N_2 compared to the dry stream (Figure 6). Together, these findings indicate favorable interactions between water and adsorbed CO_2 in dmpn−Mg_2(dobpdc), which could lead to enhanced uptake of low partial pressures of CO_2 under humid conditions.

To corroborate these promising TGA results, we also performed breakthrough experiments using 0.63 g of semi-spherical dmpn−Mg_2(dobpdc) pellets (350−700 μm diameter) in a stainless steel column with a total packed adsorbent volume of 2.19 cm^3 (Figure 7; see section 7 of the Supporting Information for further details). First, breakthrough measurements with a dry 15% CO_2 in N_2 stream were carried out. Near immediate breakthrough of N_2 was observed (blue circles, capacity: <0.1 mmol/g), followed by sharp breakthrough of CO_2 (green circles, capacity: 2.7 mmol/g) after approximately 30 min at a flow rate of 10 sccm. The incident stream was then switched to He that had been bubbled through water at room temperature, and the dmpn−Mg_2(dobpdc) was humidified at 40 °C until water breakthrough was detected at the end of the column. Several breakthrough adsorption cycles at 40 °C were then carried out on the water-saturated bed using a stream of 15% CO_2 in N_2 that was humidified by bubbling through CO_2-saturated water at room temperature (∼2% water). Similar to the dry breakthrough results, the facile separation of N_2 (purple circles, capacity: <0.1 mmol/g) and CO_2 could be achieved under humid conditions. Moreover, the CO_2 breakthrough curve became sharper in the presence of water (black circles), leading to a slightly higher CO_2 capacity of 3.0 mmol/g compared to the dry breakthrough measurements. These breakthrough measurements confirm that dmpn−Mg_2(dobpdc) shows superior adsorption of CO_2 under humid conditions compared to dry conditions, making it effective for the removal of CO_2 from a coal flue gas stream.

Another critical factor for employing dmpn−Mg_2(dobpdc) is its long-term stability to adsorption/desorption cycling under humid conditions. This stability was examined by subjecting dmpn−Mg_2(dobpdc) to 1000 simulated adsorption (humid 15% CO_2 in N_2, 5 min, 40 °C) and desorption (humid CO_2, 1 min, 100 °C) cycles, the results of which are summarized in Figure 8. The adsorption and desorption capacities (black circles), as well as the CO_2/H_2O cycling capacity (blue circles), remained constant during the last 200 cycles (see Figure S36 for the raw cycling data, SI). In addition, the adsorbent maintained crystallinity and a high diamine loading of 97% after both 300 and 1000 cycles, confirming that dmpn−Mg_2(dobpdc) is stable to both diamine loss and degradation upon long-term cycling in the presence of water. Some permanently adsorbed species (∼7.4 g/100 g, ∼4.1 mmol/g if all water) slowly built up during the first 100 cycles, though a high cycling capacity of ∼10 g/100 g (∼2.3 mmol/g if all CO_2) was still achieved over the last 200 cycles with only a 60 °C temperature swing.[25] Very short adsorption (5 min) and desorption (1 min) intervals could be used in this cycling experiment, reflecting the fast CO_2/H_2O adsorption and desorption kinetics of dmpn−Mg_2(dobpdc). Overall, the dry and humid adsorption measurements indicate that dmpn−

DOI: 10.1021/jacs.7b07612
J. Am. Chem. Soc. 2017, 139, 13541−13553

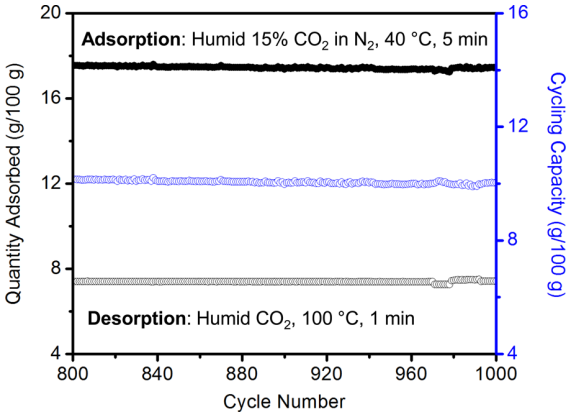

Figure 8. Adsorption maxima (filled black circles), desorption minima (open black circles), and cycling capacities (open blue circles) of the last 200 of 1000 humid cycles of dmpn−Mg_2(dobpdc), as determined by thermogravimetric analysis (TGA). The baseline value of 0 g/100 g is defined as the mass after activation under humid 15% CO_2 in N_2 for 20 min at 130 °C prior to the first cycle.

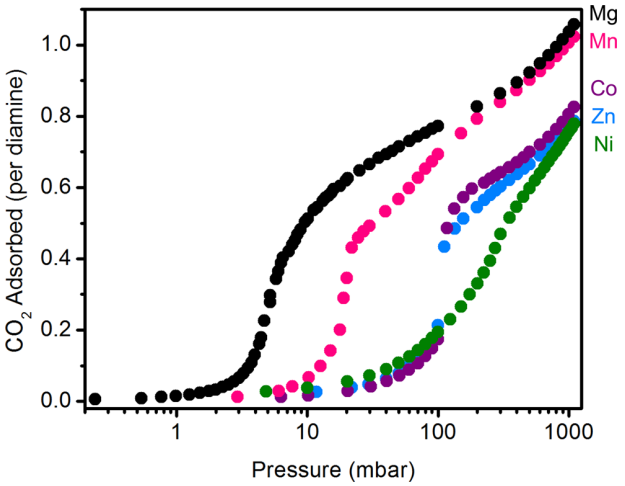

Figure 9. Metal effect on CO_2 adsorption at 25 °C for dmpn−M_2(dobpdc) (M = Mg, Mn, Co, Zn, Ni). Black, pink, purple, light blue, and green represent Mg, Mn, Co, Zn, and Ni, respectively.

Mg_2(dobpdc) is an excellent adsorbent for carbon capture from coal flue gas.

Mechanism of CO_2 Adsorption. *Metal Effect on CO_2 Adsorption Step Pressure.* We initially hypothesized that the CO_2 adsorption step in dmpn−Mg_2(dobpdc) originated from the cooperative formation of ammonium carbamate chains, similar to the behavior previously reported for related frameworks.[16a,b] However, the unusual CO_2 adsorption profile (Figures 3 and 4) and deviation from the linear relationship between Δh_{ads} and Δs_{ads} followed by other adsorbents in this family (Figure 5) suggested a change in the adsorption mechanism for dmpn−Mg_2(dobpdc). One diagnostic feature of ammonium carbamate chain formation is a metal effect on the CO_2 adsorption step pressure, because this mechanism involves breaking a M−N bond and forming a M−O bond.[16b] To probe any potential metal effect on the CO_2 adsorption step, dmpn−M_2(dobpdc) (M = Mn, Co, Ni, Zn) were synthesized and compared to the Mg analogue (see section 4 of the Supporting Information for details). The CO_2 adsorption isotherms for dmpn−M_2(dobpdc) (M = Mg, Mn, Co, Zn) at 25 °C confirm that these adsorbents undergo step-shaped adsorption of CO_2 (Figure 9). The distinctive isotherm shapes of dmpn−M_2(dobpdc) (M = Mn, Co, Zn) are similar to that of the Mg analogue, suggesting that these materials adsorb CO_2 via a similar uptake mechanism. Consistent with cleavage of the M−N bond during CO_2 adsorption, the CO_2 adsorption step pressures increase in the order Mg < Mn < Co ≈ Zn, which is the same order previously observed for M_2(dobpdc) variants appended with *N,N′*-dimethylethylenediamine[16b] and trends with increasing M−N bond strength.[26] In addition, the diagnostic C−N stretch of an ammonium carbamate at ∼1330 cm^{-1} was observed in the IR spectra of CO_2-dosed samples of dmpn−M_2(dobpdc) (M = Mg, Mn, Co, Zn) (Figures S41 and 42, SI).[15a,16a,b] Taken together, these findings support the formation of ammonium carbamate chains in dmpn−M_2(dobpdc) (M = Mg, Mn, Co, Zn). Notably, as with alkylethylenediamine-appended variants,[16b] dmpn−Ni_2(dobpdc) did not display step-shaped adsorption of CO_2 and thus likely adsorbs CO_2 via a distinct mechanism.

Solid-State ^{13}C NMR Experiments. To further probe the CO_2 adsorption mechanism in dmpn−Mg_2(dobpdc), magic angle spinning (MAS) solid-state ^{13}C NMR measurements with isotopically enriched $^{13}CO_2$ were carried out (Figures 10 and 11). Using $^{13}CO_2$ improved the signal-to-noise ratio of these spectra and allowed for short acquisition times (∼30 min).[27] In addition, a custom dosing manifold enabled the preparation of samples dosed with different pressures of $^{13}CO_2$ and thus for the examination of the uptake mechanism at different points in the CO_2 adsorption isotherms (see section 8 of the Supporting Information for details).

To serve as a point of reference, the ^{13}C NMR spectrum of $^{13}CO_2$-dosed dmen−Mg_2(dobpdc)[17a] (Figure 10) was collected, as the single-crystal X-ray diffraction structure of dmen−Zn_2(dobpdc) confirms that it forms ammonium carbamate chains (Figure S47, SI). Consistent with the literature,[17a] the ^{13}C NMR spectrum of dmen−Mg_2(dobpdc) displays a new resonance at 163.7 ppm upon exposure to $^{13}CO_2$ (Figure 10a). This same resonance was observed at both moderate (129 mbar) and high (989 mbar) pressures of $^{13}CO_2$. Previous solid-state NMR studies of amine-appended silicas assign resonances with this chemical shift to the carbonyl carbon of an ammonium carbamate species.[28] The remainder of the spectrum features assignable resonances from the framework and diamine comparable to the spectrum obtained before $^{13}CO_2$ dosing (Figure S39, SI), supporting the formation of one dominant ammonium carbamate species upon exposure to $^{13}CO_2$.

The ^{13}C NMR spectra of pn−Mg_2(dobpdc)−$^{13}CO_2$ and mpn−Mg_2(dobpdc)−$^{13}CO_2$ are similar to that of dmen−Mg_2(dobpdc)−$^{13}CO_2$, with a single dominant resonance observed at 162.7 and 162.8 ppm, respectively (Figure 10b,c). In both cases, the same dominant chemisorbed species was observed at low and high pressures of $^{13}CO_2$, although a slight shoulder was observed at ∼159 ppm in the spectrum of pn−Mg_2(dobpdc) at 980 mbar of $^{13}CO_2$. In addition, the IR spectra of CO_2-dosed samples of mpn− and pn−Mg_2(dobpdc) display new stretches at ∼1330 cm^{-1} corresponding to the C−N stretch of an ammonium carbamate species (Figure S41, SI).[15a,16a,b] Taken together, these findings suggest that mpn− and pn−Mg_2(dobpdc) predominantly form ammonium carbamate chains upon CO_2 adsorption. Unfortunately, we have thus far been unable to structurally characterize the CO_2-

DOI: 10.1021/jacs.7b07612
J. Am. Chem. Soc. 2017, 139, 13541−13553

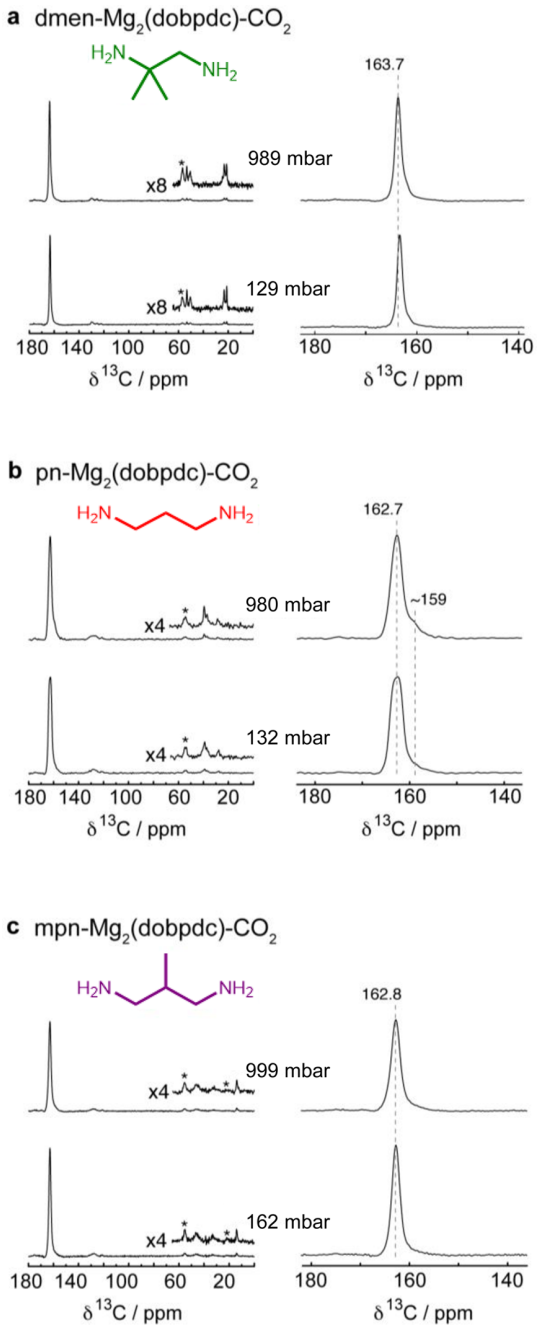

Figure 10. Room-temperature ^{13}C MAS NMR (7.1 T) spectra for (a) dmen−Mg_2(dobpdc), (b) pn−Mg_2(dobpdc), and (c) mpn−Mg_2(dobpdc) dosed with two different pressures of $^{13}CO_2$. Spectra were acquired by cross-polarization from ^{1}H. Sample spinning rates were 8 kHz in all cases.

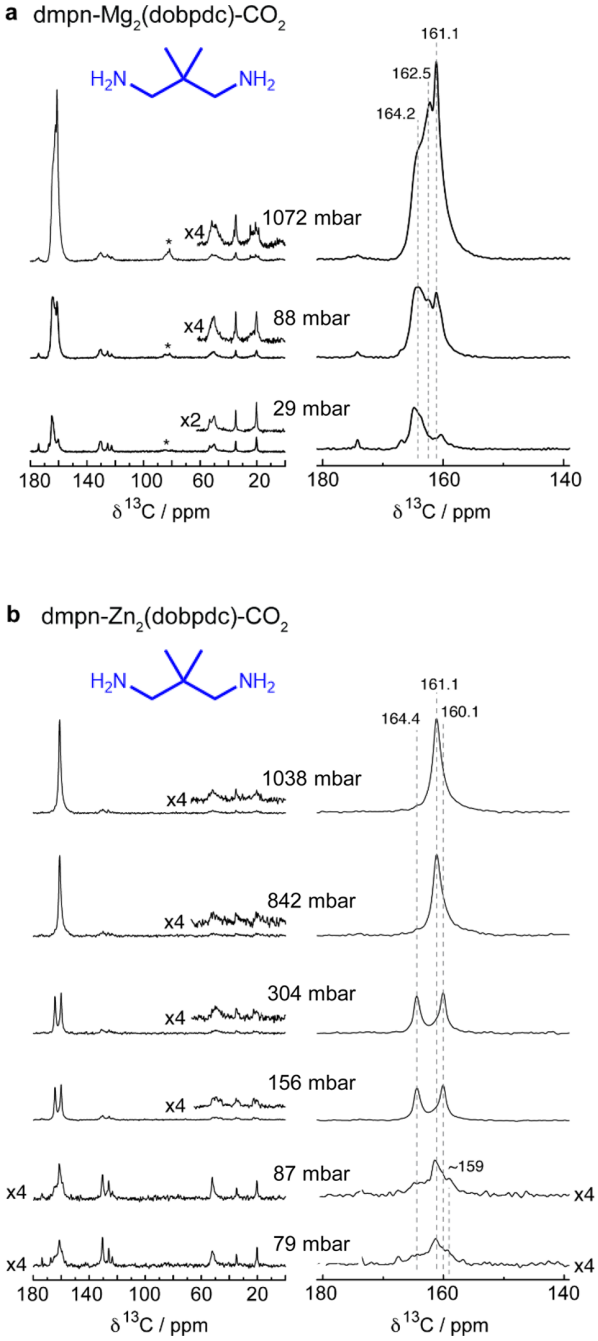

Figure 11. Room-temperature ^{13}C MAS NMR (7.1 T) spectra for (a) dmpn−Mg_2(dobpdc) and (b) dmpn−Zn_2(dobpdc) dosed with various pressures of $^{13}CO_2$. Spectra were acquired by cross-polarization from ^{1}H. Sample spinning rates were 8 kHz for dmpn−Mg_2(dobpdc) (a) and 7, 10, 11, 10, 10, and 11 kHz for spectra at 79, 87, 156, 304, 842, and 1038 mbar, respectively, for dmpn−Zn_2(dobpdc) (b).

adsorbed phases of mpn− or pn−M_2(dobpdc) variants to confirm this hypothesis.

In contrast, the ^{13}C NMR spectrum of dmpn−Mg_2(dobpdc)−$^{13}CO_2$ is significantly more complex, with at least two resonances corresponding to the carbonyl carbon atoms of chemisorbed species observed at 164.2 and 161.1 ppm under 29 mbar of $^{13}CO_2$ (Figure 11a). At higher pressures (88 and 1072 mbar), three resonances result from chemisorbed $^{13}CO_2$. Additional splitting of the amine resonances is also apparent, particularly at 1072 mbar, supporting the formation of multiple chemisorbed species. By comparison with the ^{13}C NMR spectra shown in Figure 10, as well as with the literature,[28] we assign the downfield resonance at 164.2 ppm that dominates immediately after the CO_2 adsorption step (29 mbar) as arising from ammonium carbamate chains. Due to the low step pressure of dmpn−Mg_2(dobpdc) at room temperature (∼5 mbar), we have thus far been unable to obtain ^{13}C NMR spectra at $^{13}CO_2$ pressures below the adsorption step.

DOI: 10.1021/jacs.7b07612
J. Am. Chem. Soc. 2017, 139, 13541−13553

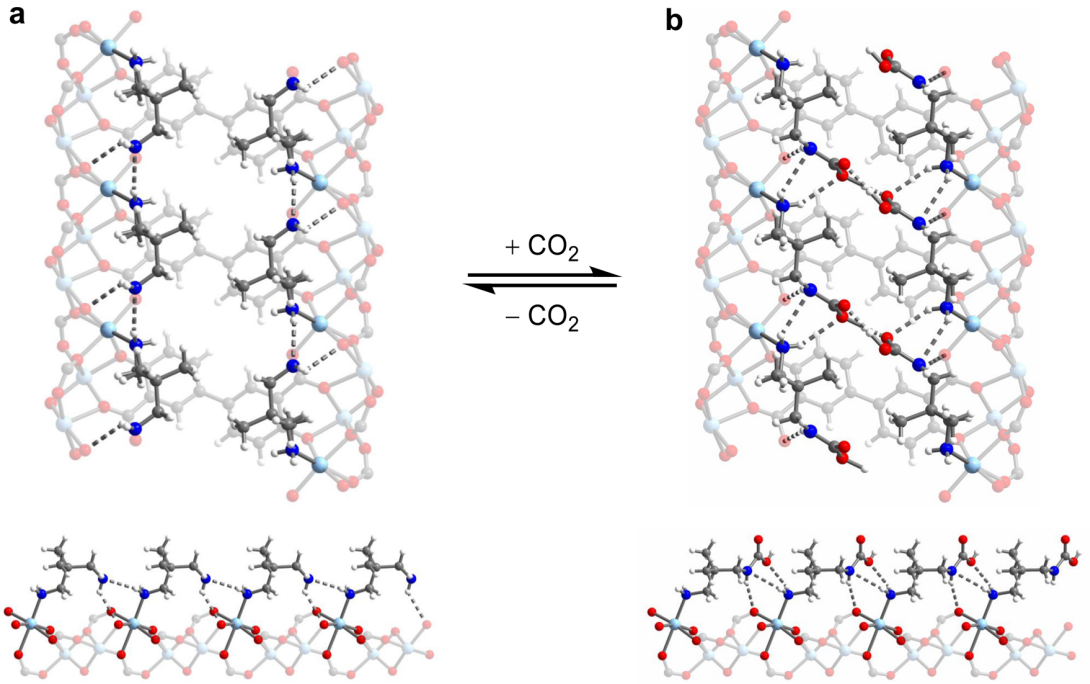

Figure 12. Single-crystal X-ray diffraction structures of dmpn−Zn_2(dobpdc) at 100 K, with two views shown. (a) The structure of diethyl ether-solvated dmpn−Zn_2(dobpdc) shows hydrogen bonding between adjacent diamines [N···N distance = 3.26(3) Å]. (b) After activation and dosing with 1 bar of CO_2, dmpn−Zn_2(dobpdc) forms bridging carbamic acid pairs. Extensive hydrogen bonding of carbamic acids to the framework and between adjacent carbamic acid pairs is observed. The hydrogen atoms between the carbamic acid pairs could not be located crystallographically and are shown here as visual aids. The structure of dmpn−Mg_2(dobpdc)−CO_2 was obtained at 100 K. Light blue, blue, red, gray, and white spheres represent Zn, N, O, C, and H, respectively.

The higher step pressure of dmpn−Zn_2(dobpdc) (∼100 mbar, 25 °C) compared to that of dmpn−Mg_2(dobpdc) (∼5 mbar, 25 °C) allowed for the acquisition of ^{13}C NMR spectra before and after the adsorption step (Figure 11b). At partial pressures of $^{13}CO_2$ below the adsorption step (79 and 87 mbar), a number of weak, broad resonances arise from chemisorbed $^{13}CO_2$ (160−165 ppm). These relatively weak signals result from the minor amounts of $^{13}CO_2$ (≤0.5 mmol/g) adsorbed at these pressures (Figure 9). Increasing the $^{13}CO_2$ pressure past the CO_2 adsorption step (156 and 304 mbar) results in two sharp resonances at 164.4 and 160.1 ppm and splitting of the resonances corresponding to the framework and diamine into several peaks. By comparison with the literature[28] and the other ^{13}C NMR spectra presented in Figure 10, we assign the downfield resonance at 164.4 ppm in these spectra to ammonium carbamate chains. Indeed, density functional theory (DFT) calculations using a putative ammonium carbamate chain structure for dmpn−Zn_2(dobpdc)−CO_2 yielded a predicted chemical shift of 165.3 ppm (Figure S40, SI). Thus, the NMR experiments indicate that the ammonium carbamate species observed by both ^{13}C NMR and IR spectroscopy is partly responsible for the adsorption step at ∼100 mbar at 25 °C.

Interestingly, at higher pressures of $^{13}CO_2$ (842 and 1038 mbar), the two resonances observed at intermediate pressures greatly decrease in intensity, leading a hitherto unidentified species (161.1 ppm) to dominate at 1038 mbar. In contrast, for dmpn−Mg_2(dobpdc) the assigned ammonium carbamate chains (164.2 ppm) are apparent even at high pressures of $^{13}CO_2$ (1072 mbar), reflecting their more stable nature compared to those of the Zn analogue.[16b] Although it is perhaps unsurprising that dmpn−M_2(dobpdc) (M = Mg, Mn, Co, Zn) analogues form ammonium carbamate species upon CO_2 adsorption in view of the reactivity of related diamine-appended metal−organic frameworks,[16a,b] the identity of the other chemisorbed species in the ^{13}C NMR spectra of dmpn−M_2(dobpdc) (M = Mg, Zn) was not immediately apparent.

Single-Crystal X-ray Diffraction Studies. We turned to single-crystal X-ray diffraction in order to identify the species observed at 161.1 ppm that dominates the ^{13}C NMR spectrum of dmpn−Zn_2(dobpdc) at higher pressures of $^{13}CO_2$ (Figure 11). The structure of diethyl ether-solvated dmpn−Zn_2(dobpdc) was first obtained in the absence of CO_2 (Figure 12a). Importantly, considerable unobstructed pore volume remains after diamine grafting (Figure S45, SI), consistent with the high Brunauer−Emmett−Teller (BET) surface area of 948 ± 3 m^2/g determined for dmpn−Mg_2(dobpdc) from the N_2 adsorption isotherm at 77 K (Figure S6, SI). This should allow for rapid diffusion of CO_2 into and out of the pores. Interestingly, the presence of an extensive hydrogen-bonding network between adjacent diamines can be inferred from the close N···N contacts of 3.26(3) Å. In addition, the powder X-ray diffraction pattern of dmpn−Mn_2(dobpdc) is consistent with the presence of a similar hydrogen-bonding network (see section 10 of the Supporting Information). Likewise, the single-crystal structure of toluene-solvated mpn−Zn_2(dobpdc) shows two distinct conformations involving hydrogen bonding between amines; the minor conformer involves hydrogen bonding along the *c*-axis, as in Figure 12a [30.8(13)% occupancy], whereas the major conformer [57.1(13)% occupancy] involves intramolecular hydrogen bonding between the terminal and metal-bound amines of a single diamine

DOI: 10.1021/jacs.7b07612
J. Am. Chem. Soc. 2017, 139, 13541−13553

(Figure S46, SI). These interactions are not available to alkylethylenediamine-appended variants of Zn_2(dobpdc) because adjacent diamines are unable to reach one another down the *c*-axis[16a,b] and likely contribute significantly to the observed stability of dmpn−Mg_2(dobpdc) to adsorption/desorption cycling (Figure 8).

Remarkably, dosing activated single crystals of dmpn−Zn_2(dobpdc) with 1 bar of CO_2 allowed us to obtain the X-ray diffraction structure corresponding to the unidentified species observed by solid-state ^{13}C NMR spectroscopy (Figure 11). In contrast to all other diamine-appended metal organic frameworks studied to date,[16a,b] dmpn−Zn_2(dobpdc) was found to form carbamic acid pairs bridging diagonally adjacent diamines upon exposure to CO_2 (Figures 12b and 13). While the bridging hydrogen atoms could not be located in the structure, their presence was inferred from the close O···O contacts of 2.38(4) and 2.88(4) Å, respectively. These pairs are connected by hydrogen-bonding interactions along the *c*-axis and thus form an extended ladderlike structure running down the pores of the framework (Figure 12b). Importantly, significant unoccupied pore volume remains even after CO_2 adsorption, enabling facile gas transport through the pores (Figure 13). Although previous DFT calculations suggested that the formation of carbamic acid pairs would not be expected to proceed cooperatively,[29] the presence of hydrogen-bonding interactions along the *c*-axis in this structure may impart some degree of cooperativity. However, such interactions are also present in the absence of CO_2 (Figure 12a), and therefore, any cooperative effects are likely offset by similar hydrogen-bonding interactions between adjacent carbamic acid pairs, between carbamic acid pairs and adjacent free amines, and between adjacent free amines. Therefore, the carbamic acid pairs likely dominate in the poststep regimes of the CO_2 isotherms of dmpn−M_2(dobpdc) (M = Mg, Mn, Co, Zn), with insertion to form ammonium carbamate chains occurring predominantly near the CO_2 adsorption step. The combination of a primarily noncooperative adsorption isotherm for the carbamic acid pairs and a step-shaped adsorption isotherm for the ammonium carbamate chains likely gives rise to the distinct isotherm shapes of dmpn-functionalized analogues of M_2(dobpdc). Notably, dmpn−Ni_2(dobpdc), which possesses M−N bonds that are too strong to allow for CO_2 insertion to form ammonium carbamate chains,[16b] likely adsorbs CO_2 exclusively via the formation of carbamic acid pairs and exhibits a noncooperative adsorption profile.

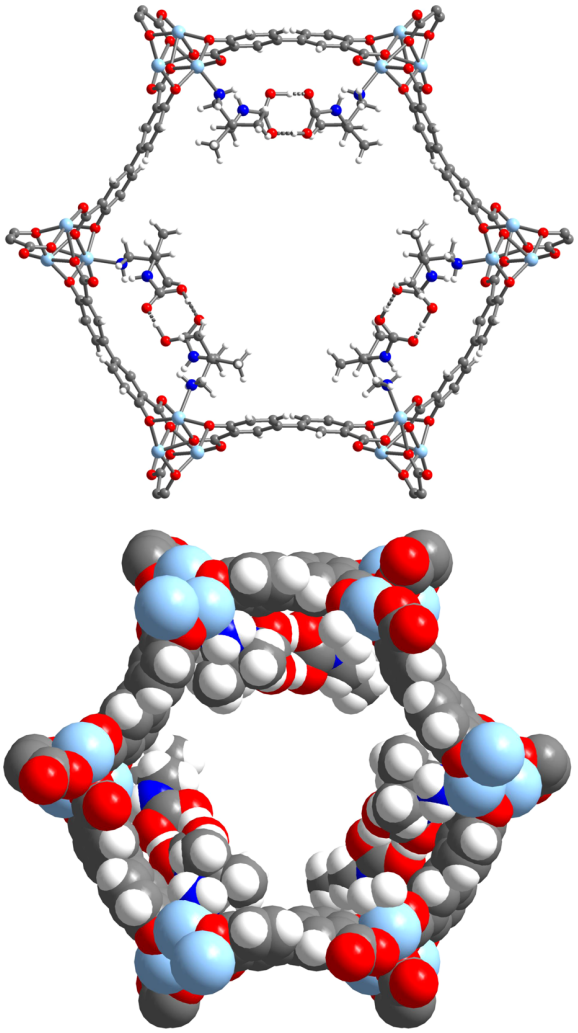

Figure 13. View down the *c*-axis of the single-crystal X-ray diffraction structure of the carbamic acid pairs formed upon CO_2 adsorption in dmpn−Zn_2(dobpdc) at 100 K. The hydrogen atoms between the carbamic acid pairs could not be located crystallographically and are shown here as visual aids. Light blue, blue, red, gray, and white spheres represent Zn, N, O, C, and H, respectively.

Although carbamic acid pairs have not been experimentally observed in a diamine-appended metal−organic framework until now, previous DFT calculations found that carbamic acid pairs of a different geometry were comparable in energy to the experimentally observed ammonium carbamate chains with *N*,*N*′-dimethylethylenediamine in place of dmpn.[16b,29] The formation of hydrogen-bond-stabilized carbamic acids upon reaction with CO_2 has also been proposed in certain amine-functionalized adsorbents,[15a,b,30] but this adsorption mechanism has recently been called into doubt[31] due to the known instability of carbamic acids.[32] Therefore, to the best of our knowledge, the present results constitute the first crystallographic observation of carbamic acid pair formation in a porous solid[33−35] and thus serve as corroborating evidence for the formation of carbamic acid species stabilized by hydrogen bonding in other adsorbents. Consistent with this assessment, the solid-state ^{13}C NMR resonances previously ascribed to carbamic acid species were observed at ∼160 ppm,[28] similar in chemical shift to the resonance at 161.1 ppm we assign to carbamic acid pairs in the ^{13}C NMR spectra of dmpn−Zn_2(dobpdc) (Figure 11). In addition, DFT calculations using the single-crystal X-ray diffraction structure (Figure 12b) afforded a predicted chemical shift of 161.1 ppm for the observed carbamic acid pairs (see section 8 of the Supporting Information for details). On the basis of this assignment, the species observed at intermediate pressures (156 and 304 mbar) at 160.1 ppm in the ^{13}C NMR spectra of dmpn−Zn_2(dobpdc) is possibly an unpaired carbamic acid intermediate. Together, the ^{13}C NMR and X-ray diffraction experiments corroborate that dmpn−M_2(dobpdc) (M = Mg, Mn, Co, Zn) form a complex mixture of ammonium carbamate and carbamic acid species upon CO_2 adsorption.

■ CONCLUSION

Through careful consideration of the thermodynamics of CO_2 adsorption in diamine-appended metal−organic frameworks, we have developed a new adsorbent, dmpn−Mg_2(dobpdc), that

DOI: 10.1021/jacs.7b07612
J. Am. Chem. Soc. 2017, 139, 13541−13553

is well-tuned for the efficient capture of CO_2 from coal flue gas. Specifically, the highly negative differential enthalpy of adsorption (Δh_{ads} = −74 ± 1 kJ/mol) facilitates the effective capture of CO_2 at 40 °C and near complete regeneration at 100 °C under 1 bar of CO_2, whereas the larger than expected entropic penalty for CO_2 adsorption (Δs_{ads} = −204 ± 4 J/mol·K) moves the step to a higher pressure at a given temperature. With this new adsorbent, a narrow temperature swing (ΔT = 60 °C) can be used to achieve a high CO_2 working capacity of 2.42 mmol/g (9.1 wt %) in a TSA process, which should help to dramatically lower the energy penalty associated with carbon capture and sequestration. Importantly, dmpn−Mg_2(dobpdc) also exhibits exceptional long-term stability and maintains its performance under humid conditions. Efforts are now underway to evaluate the use of dmpn−Mg_2(dobpdc) for large-scale CO_2 capture applications.

The NMR studies presented herein suggest that the mechanistic possibilities for the uptake of CO_2 in diaminopropane-appended metal−organic frameworks are more complex than with ethylenediamines, as the latter appear to adsorb CO_2 solely via cooperative formation of ammonium carbamate chains (Figure 10a).[16a,b] In particular, the addition of a single methyl group to the diamine backbone (from mpn to dmpn) drastically changes the CO_2 adsorption step pressure (Figure 3a), differential entropy of adsorption (Figure 5), and CO_2 adsorption mechanism (Figures 10−12). Relatedly, single-crystal X-ray diffraction and ^{13}C NMR experiments demonstrate for the first time that carbamic acid pair formation is feasible and can occur competitively with ammonium carbamate chain formation in a diamine-appended metal−organic framework. Additional structural and NMR investigations are underway to fully understand the effect of diaminopropane structure, metal, CO_2 partial pressure, temperature, and humidity on the mechanisms of CO_2 adsorption in dmpn−Mg_2(dobpdc). One critical area for further experimental and theoretical investigation is the relationship between bridging carbamic acid pairs and ammonium carbamate chains, particularly regarding the cooperative adsorption of CO_2. Given the exceptional promise of dmpn−Mg_2(dobpdc) for the efficient capture from coal flue gas, these studies should prove valuable for developing next-generation adsorbents for carbon capture applications.

■ ASSOCIATED CONTENT

Supporting Information

The Supporting Information is available free of charge on the ACS Publications website at DOI: 10.1021/jacs.7b07612.

CIF file for Zn_2(dobpdc)(dmpn)$_{0.65}$(dmpn−CO_2)$_{0.77}$ (CIF)
CIF file for Zn_2(dobpdc)(dmpn)$_{1.3}$ (CIF)
CIF file for Zn_2(dobpdc)(mpn)$_{1.76}$(C_7H_8)$_{0.62}$ (CIF)
CIF file for Zn_2(dobpdc)(dmen)$_{0.98}$(dmen−CO_2)$_{0.76}$ (CIF)
CIF file for Zn_2(dobpdc)(dmen)$_{1.61}$·(H_2O)$_{0.70}$ (CIF)
Full characterization of all new adsorbents and additional experimental details (PDF)

■ AUTHOR INFORMATION

Corresponding Author

*jrlong@berkeley.edu

ORCID

Jeffrey R. Long: 0000-0002-5324-1321

Notes

The authors declare the following competing financial interest(s): J.R.L. has a financial interest in Mosaic Materials, Inc., a start-up company working to commercialize metal−organic frameworks for gas separations, including CO_2 capture applications. The University of California, Berkeley has applied for a patent on some of the technology discussed herein, on which J.R.L., P.J.M., and R.L.S. are listed as inventors.

■ ACKNOWLEDGMENTS

We acknowledge ExxonMobil Research and Engineering Company for funding the initial synthesis and characterization of pn−, mpn−, and dmpn−Mg_2(dobpdc) as part of a carbon capture research project. Crystallographic and solid-state NMR studies were supported through the Center for Gas Separations Relevant to Clean Energy Technologies, an Energy Frontier Research Center funded by the U.S. Department of Energy (DoE), Office of Science, Office of Basic Energy Sciences, under Award DE-SC0001015. The collection and analysis of adsorption data for dmpn−Mg_2(dobpdc) for CCS applications was supported by the U.S./China Clean Energy Research Center for Water-Energy Technologies (CERC-WET). We thank the National Institute of General Medical Sciences of the National Institutes of Health for a postdoctoral fellowship for P.J.M. (F32GM120799). The content is solely the responsibility of the authors and does not necessarily represent the official views of the National Institutes of Health. We thank the Philomathia Foundation and Berkeley Energy and Climate Institute for a fellowship for A.C.F. We thank the Miller Institute for Basic Research in Science for a postdoctoral fellowship for J.D.M. This work utilized the resources of both the Advanced Light Source at Lawrence Berkeley National Laboratory, a user facility supported by the Director, Office of Science, Office of Basic Energy Sciences, of the DoE under Contract No. DE-AC02-05CH11231, and the Advanced Photon Source, DoE Office of Science User Facility operated for the DoE Office of Science by Argonne National Laboratory under Contract No. DE-AC02-06CH11357. Collection of adsorption data for dmen−Mg_2(dobpdc), men−Mg_2(dobpdc), and en−Mg_2(dobpdc) (Supporting Information, section 3) was funded by the Advanced Research Projects Agency—Energy (ARPA-E) of the DoE. Dr. Jarad Mason and Dr. Thomas McDonald are acknowledged for assistance in collecting the CO_2 isotherms of dmen−Mg_2(dobpdc). DFT calculations of ^{13}C NMR chemical shifts were supported by the National Institutes of Health (S10OD023523) via the Molecular Graphics and Computation Facility (College of Chemistry, UC Berkeley). Douglas Reed, Henry Jiang, Julia Oktawiec, Michael Ziebel, Dr. Jun Xu, and Thomas Osborn Popp (UC Berkeley), as well as Dr. Simon C. Weston (ExxonMobil), are acknowledged for experimental assistance and/or helpful discussions. A.C.F. thanks Dr. Richard Bounds for assistance with the design and manufacture of the custom vacuum manifold used for dosing NMR samples with $^{13}CO_2$.

■ REFERENCES

(1) Pachauri, R. K.; Meyer, L. A. *Climate Change 2014: Synthesis Report. Contribution of Working Groups I, II and III to the Fifth Assessment Report of the Intergovernmental Panel on Climate Change*; IPCC: Geneva, Switzerland, 2014; p 1−151.
(2) Quadrelli, R.; Peterson, S. *Energy Policy* **2007**, *35*, 5938.
(3) Akpan, U. F.; Akpan, G. E. *Int. J. Energy Econ. Policy* **2012**, *2*, 21.

DOI: 10.1021/jacs.7b07612
J. Am. Chem. Soc. 2017, 139, 13541−13553

(4) Granite, E. J.; Pennline, H. W. *Ind. Eng. Chem. Res.* **2002**, *41*, 5470.

(5) (a) Senftle, T. P.; Carter, E. A. *Acc. Chem. Res.* **2017**, *50*, 472. (b) Chu, S. *Science* **2009**, *325*, 1599. (c) Haszeldine, R. S. *Science* **2009**, *325*, 1647.

(6) (a) Bhown, A. S.; Freeman, B. C. *Environ. Sci. Technol.* **2011**, *45*, 8624. (b) House, K. Z.; Harvey, C. F.; Aziz, M. J.; Schrag, D. P. *Energy Environ. Sci.* **2009**, *2*, 193.

(7) Drage, T. C.; Snape, C. E.; Stevens, L. A.; Wood, J.; Wang, J.; Cooper, A. I.; Dawson, R.; Guo, X.; Satterley, C.; Irons, R. *J. Mater. Chem.* **2012**, *22*, 2815.

(8) (a) Boot-Handford, M. E.; Abanades, J. C.; Anthony, E. J.; Blunt, M. J.; Brandani, S.; MacDowell, N.; Fernández, J. R.; Ferrari, M.-C.; Gross, R.; Hallett, J. P.; Haszeldine, R. S.; Heptonstall, P.; Lyngfelt, A.; Makuch, Z.; Mangano, E.; Porter, R. T. J.; Pourkashanian, M.; Rochelle, G. T.; Shah, N.; Yao, J. G.; Fennell, P. S. *Energy Environ. Sci.* **2014**, *7*, 130. (b) Rochelle, G. T. *Science* **2009**, *325*, 1652.

(9) (a) Fredriksen, S. B.; Jens, K.-J. *Energy Procedia* **2013**, *37*, 1770. (b) Gouedard, C.; Picq, D.; Launay, F.; Carrette, P.-L. *Int. J. Greenhouse Gas Control* **2012**, *10*, 244.

(10) Finkeenrath, M. *Cost and Performance of Carbon Dioxide Capture from Power Generation*; International Energy Agency, 2011.

(11) For selected reviews, see the following: (a) Yu, J.; Xie, L.-H.; Li, J.-R.; Ma, Y.; Seminario, J. M.; Balbuena, P. B. *Chem. Rev.* **2017**, *117*, 9674. (b) Lee, S.-Y.; Park, S.-J. *J. Ind. Eng. Chem.* **2015**, *23*, 1. (c) Sabouni, R.; Kazemian, H.; Rohani, S. *Environ. Sci. Pollut. Res.* **2014**, *21*, 5427. (d) Sumida, K.; Rogow, D. L.; Mason, J. A.; McDonald, T. M.; Bloch, E. D.; Herm, Z. R.; Bae, T.-H.; Long, J. R. *Chem. Rev.* **2012**, *112*, 724. (e) Liu, Y.; Wang, Z. U.; Zhou, H.-C. *Greenhouse Gases: Sci. Technol.* **2012**, *2*, 239. (f) Samanta, A.; Zhao, A.; Shimizu, G. K. H.; Sarkar, P.; Gupta, R. *Ind. Eng. Chem. Res.* **2012**, *51*, 1438. (g) D'Alessandro, D. M.; Smit, B.; Long, J. R. *Angew. Chem., Int. Ed.* **2010**, *49*, 6058.

(12) For selected examples, see the following: (a) Woerner, W. R.; Plonka, A. M.; Chen, X.; Banerjee, D.; Thallapally, P. K.; Parise, J. B. *J. Phys. Chem. C* **2016**, *120*, 360. (b) Mason, J. A.; McDonald, T. M.; Bae, T.-H.; Bachman, J. E.; Sumida, K.; Dutton, J. J.; Kaye, S. S.; Long, J. R. J. *J. Am. Chem. Soc.* **2015**, *137*, 4787. (c) Burtch, N. C.; Jasuja, H.; Walton, K. S. *Chem. Rev.* **2014**, *114*, 10575. (d) Liu, J.; Thallapally, P. K.; McGrail, B. P.; Brown, D. R.; Liu, J. *Chem. Soc. Rev.* **2012**, *41*, 2308. (e) Wang, Y.; LeVan, M. D. *J. Chem. Eng. Data* **2010**, *55*, 3189.

(13) Adsorbents lacking open metal sites tend to be more stable under humid conditions, although their CO_2 capacities under flue gas conditions are modest and their ability to capture CO_2 effectively under humid conditions remains uncertain (see ref 12b for further details). For selected examples, see the following: (a) Nandi, S.; Collins, S. P.; Chakraborty, D.; Banerjee, D.; Thallapally, P. K.; Woo, T. K.; Vaidhyanathan, R. *J. Am. Chem. Soc.* **2017**, *139*, 1734. (b) Bhatt, P. M.; Belmabkhout, Y.; Cadiau, A.; Adil, K.; Shekhah, O.; Shkurenko, A.; Barbour, L. J.; Eddaoudi, M. *J. Am. Chem. Soc.* **2016**, *138*, 9301. (c) Elsaidi, S. K.; Mohamed, M. H.; Schaef, H. T.; Kumar, A.; Lusi, M.; Pham, T.; Forrest, K. A.; Space, B.; Xu, W.; Halder, G. J.; Liu, J.; Zaworotko, M. J.; Thallapally, P. K. *Chem. Commun.* **2015**, *51*, 15530. (d) Nugent, P.; Belmabkhout, Y.; Burd, S. D.; Cairns, A. J.; Luebke, R.; Forrest, K.; Pham, T.; Ma, S.; Space, B.; Wojtas, L.; Eddaoudi, M.; Zaworotko, M. J. *Nature* **2013**, *495*, 80.

(14) (a) Ünveren, E. E.; Monkul, B. O.; Sarioğlan, S.; Karademir, N.; Alper, E. *Petroleum* **2017**, *3*, 37. (b) Kim, C.; Cho, H. S.; Chang, S.; Cho, S. J.; Choi, M. *Energy Environ. Sci.* **2016**, *9*, 1803. (c) Lin, Y.; Kong, C.; Chen, L. *RSC Adv.* **2016**, *6*, 32598. (d) Bollini, P.; Didas, S. A.; Jones, C. W. *J. Mater. Chem.* **2011**, *21*, 15100.

(15) For selected examples, see the following: (a) Didas, S. A.; Sakwa-Novak, M. A.; Foo, G. S.; Sievers, C.; Jones, C. W. *J. Phys. Chem. Lett.* **2014**, *5*, 4194. (b) Bacsik, Z.; Ahlsten, N.; Ziadi, A.; Zhao, G.; Garcia-Bennett, A. E.; Martín-Matute, B.; Hedin, N. *Langmuir* **2011**, *27*, 11118. (c) Sayari, A.; Belmabkhout, Y. *J. Am. Chem. Soc.* **2010**, *132*, 6312. (d) Serna-Guerrero, R.; Da'na, E.; Sayari, A. *Ind. Eng. Chem. Res.* **2008**, *47*, 9406.

(16) (a) Siegelman, R. L.; McDonald, T. M.; Gonzalez, M. I.; Martell, J. D.; Milner, P. J.; Mason, J. A.; Berger, A. H.; Bhown, A. S.; Long, J. R. *J. Am. Chem. Soc.* **2017**, *139*, 10526. (b) McDonald, T. M.; Mason, J. A.; Kong, X.; Bloch, E. D.; Gygi, D.; Dani, A.; Crocellà, V.; Giordanino, F.; Odoh, S. O.; Drisdell, W. S.; Vlaisavljevich, B.; Dzubak, A. L.; Poloni, R.; Schnell, S. K.; Planas, N.; Lee, K.; Pascal, T.; Wan, L. F.; Prendergast, D.; Neaton, J. B.; Smit, B.; Kortright, J. B.; Gagliardi, L.; Bordiga, S.; Reimer, J. A.; Long, J. R. *Nature* **2015**, *519*, 303. (c) McDonald, T. M.; Lee, W. R.; Mason, J. A.; Wiers, B. M.; Hong, C. S.; Long, J. R. *J. Am. Chem. Soc.* **2012**, *134*, 7056. See also the following: (d) Drisdell, W. S.; Poloni, R.; McDonald, T. M.; Pascal, T. A.; Wan, L. F.; Pemmaraju, C. D.; Vlaisavljevich, B.; Odoh, S. O.; Neaton, J. B.; Long, J. R.; Prendergast, D.; Kortright, J. B. *Phys. Chem. Chem. Phys.* **2015**, *17*, 21448. (e) McDonald, T. M.; D'Alessandro, D. M.; Krishna, R.; Long, J. R. *Chem. Sci.* **2011**, *2*, 2022. (f) Demessence, A.; D'Alessandro, D. M.; Foo, M. L.; Long, J. R. *J. Am. Chem. Soc.* **2009**, *131*, 8784.

(17) For the functionalization of Mg_2(dobpdc), see the following: (a) Jo, H.; Lee, W. R.; Kim, N. W.; Jung, H.; Lim, K. S.; Kim, J. E.; Kang, D. W.; Lee, H.; Hiremath, V.; Seo, J. G.; Jin, H.; Moon, D.; Han, S. S.; Hong, C. S. *ChemSusChem* **2017**, *10*, 541. (b) Lee, W. R.; Jo, H.; Yang, L.-M.; Lee, H.; Ryu, D. W.; Lim, K. S.; Song, J. H.; Min, D. Y.; Han, S. S.; Seo, J. G.; Park, Y. K.; Moon, D.; Hong, C. S. *Chem. Sci.* **2015**, *6*, 3697. (c) Lee, W. R.; Hwang, S. Y.; Ryu, D. W.; Lim, K. S.; Han, S. S.; Moon, D.; Choi, J.; Hong, C. S. *Energy Environ. Sci.* **2014**, *7*, 744. For the functionalization of other open-metal-site metal−organic frameworks with diamines, see the following: (d) Liao, P.-Q.; Chen, X.-W.; Liu, S.-Y.; Li, X.-Y.; Xu, Y.-T.; Tang, M.; Rui, Z.; Ji, H.; Zhang, J.-P.; Chen, X.-M. *Chem. Sci.* **2016**, *7*, 6528. (e) Darunte, L. A.; Oetomo, A. D.; Walton, K. S.; Sholl, D. S.; Jones, C. W. *ACS Sustainable Chem. Eng.* **2016**, *4*, 5761. (f) Yeon, J. S.; Lee, W. R.; Kim, N. W.; Jo, H.; Lee, H.; Song, J. H.; Lim, K. S.; Kang, D. W.; Seo, J. G.; Moon, D.; Wiers, B.; Hong, C. S. J. *J. Mater. Chem. A* **2015**, *3*, 19177. (g) Cao, Y.; Song, F.; Zhao, Y.; Zhong, Q. *J. Environ. Sci.* **2013**, *25*, 2081. (h) Hu, Y.; Verdegaal, W. M.; Yu, S.-H.; Jiang, H.-L. *ChemSusChem* **2014**, *7*, 734. (i) Lin, Y.; Lin, H.; Wang, H.; Suo, Y.; Li, B.; Kong, C.; Chen, L. J. *J. Mater. Chem. A* **2014**, *2*, 14658. (j) Choi, S.; Watanabe, T.; Bae, T.-H.; Sholl, D. S.; Jones, C. W. *J. Phys. Chem. Lett.* **2012**, *3*, 1136. (k) Montoro, C.; García, E.; Calero, S.; Pérez-Fernández, M. A.; López, A. L.; Barea, E.; Navarro, J. A. R. *J. Mater. Chem.* **2012**, *22*, 10155.

(18) Campbell, C. T.; Sellers, J. R. V. *Chem. Rev.* **2013**, *113*, 4106.

(19) Hefti, M.; Joss, L.; Bjelobrk, Z.; Mazzotti, M. *Faraday Discuss.* **2016**, *192*, 153.

(20) Song, H.-J.; Lee, S.; Park, K.; Lee, J.; Spah, D. C.; Park, J.-W.; Filburn, T. P. *Ind. Eng. Chem. Res.* **2008**, *47*, 9925.

(21) Merel, J.; Clausse, M.; Meunier, F. *Ind. Eng. Chem. Res.* **2008**, *47*, 209. This value was calculated from the approximate specific heat consumption resulting only from the adsorbent (adsorbent, desorption heat, heat losses) reported in this reference and not from the entire process (4.41 MJ/kg CO_2).

(22) (a) Datta, S. J.; Khumnoon, C.; Lee, Z. H.; Moon, W. K.; Docao, S.; Nguyen, T. H.; Hwang, I. C.; Moon, D.; Oleynikov, P.; Terasaki, O.; Yoon, K. B. *Science* **2015**, *350*, 302. (b) Joos, L.; Swisher, J. A.; Smit, B. *Langmuir* **2013**, *29*, 15936. (c) Liu, J.; Wang, Y.; Benin, A. I.; Jakubczak, P.; Willis, R. R.; LeVan, M. D. *Langmuir* **2010**, *26*, 14301.

(23) Comparing this uptake to the 40 °C water isotherm (Figure S29, SI) suggests that the partial pressure of water in the humidified stream is approximately 13 mbar, or 1.3%.

(24) One consequence of this effect is that slightly higher regeneration temperatures were found to be required under humid conditions, although regeneration at 100 °C was still sufficient to desorb CO_2 and water from dmpn−Mg_2(dobpdc) under an atmosphere of humid pure CO_2 (Figure S34, SI).

(25) The permanently adsorbed species (likely both CO_2 and water) could be more completely regenerated from the adsorbent by cycling with a higher regeneration temperature of 110 °C, leading to a higher cycling capacity after 100 cycles (15.2 g/100 g) with no deleterious

DOI: 10.1021/jacs.7b07612
J. Am. Chem. Soc. 2017, 139, 13541−13553

effect on the stability of the adsorbent (Figure S38, SI). In fact, dmpn−Mg_2(dobpdc) could be cycled with regeneration at temperatures as high as 150 °C, or held under flowing humid CO_2 for 12 h at temperatures as high as 200 °C, with minimal diamine loss. See section 7 of the Supporting Information for further details.

(26) Irving, H.; Williams, R. J. P. *J. Chem. Soc.* **1953**, *637*, 3192.

(27) Because of the low natural abundance of ^{13}C in CO_2, long acquisition times (6 h) were required to obtain ^{13}C NMR spectra with nonisotopically enriched CO_2. This led to pressure changes over the course of the acquisition due to gas leakage from the rotor.

(28) (a) Mafra, L.; Čendak, T.; Schneider, S.; Wiper, P. V.; Pires, J.; Gomes, J. R. B.; Pinto, M. L. *J. Am. Chem. Soc.* **2017**, *139*, 389. (b) Pinto, M. L.; Mafra, L.; Guil, J. M.; Pires, J.; Rocha, J. *Chem. Mater.* **2011**, *23*, 1387. (c) Moore, J. K.; Sakwa-Novak, M. A.; Chaikittisilp, W.; Mehta, A. K.; Conradi, M. S.; Jones, C. W.; Hayes, S. E. *Environ. Sci. Technol.* **2015**, *49*, 13684. (d) Foo, G. S.; Lee, J. J.; Chen, C.-H.; Hayes, S. E.; Sievers, C.; Jones, C. W. *ChemSusChem* **2017**, *10*, 266.

(29) (a) Vlaisavljevich, B.; Odoh, S. O.; Schnell, S. K.; Dzubak, A. L.; Lee, K.; Planas, N.; Neaton, J. B.; Gagliardi, L.; Smit, B. *Chem. Sci.* **2015**, *6*, 5177. (b) Planas, N.; Dzubak, A. L.; Poloni, R.; Lin, L.-C.; McManus, A.; McDonald, T. M.; Neaton, J. B.; Long, J. R.; Smit, B.; Gagliardi, L. *J. Am. Chem. Soc.* **2013**, *135*, 7402.

(30) (a) Fracaroli, A. M.; Furukawa, H.; Suzuki, M.; Dodd, M.; Okajima, S.; Gándara, F.; Reimer, J. A.; Yaghi, O. M. *J. Am. Chem. Soc.* **2014**, *136*, 8863. (b) Aziz, B.; Hedin, N.; Bacsik, Z. *Microporous Mesoporous Mater.* **2012**, *159*, 42. (c) Bacsik, Z.; Atluri, R.; Garcia-Bennett, A. E.; Hedin, N. *Langmuir* **2010**, *26*, 10013. (d) Knöfel, C.; Martin, C.; Hornebecq, V.; Llewellyn, P. L. *J. Phys. Chem. C* **2009**, *113*, 21726. (e) Dibenedetto, A.; Pastore, C.; Fragale, C.; Aresta, M. *ChemSusChem* **2008**, *1*, 742.

(31) Danon, A.; Stair, P. C.; Weitz, E. *J. Phys. Chem. C* **2011**, *115*, 11540.

(32) (a) Bossa, J.-B.; Borget, F.; Duvernay, F.; Theulé, P.; Chiavassa, T. *J. Phys. Chem. A* **2008**, *112*, 5113. (b) Masuda, K.; Ito, Y.; Horiguchi, M.; Fujita, H. *Tetrahedron* **2005**, *61*, 213. (c) Khanna, R. K.; Moore, M. H. *Spectrochim. Acta, Part A* **1999**, *55*, 961.

(33) The formation of carbamic acid pairs upon exposure of dibenzylamine to CO_2 has been confirmed by single-crystal X-ray diffraction. See the following: Aresta, M.; Ballivet-Tkatchenko, D.; Dell'Amico, D. B.; Bonnet, M. C.; Boschi, D.; Calderazzo, F.; Faure, R.; Labella, L.; Marchetti, F. *Chem. Commun.* **2000**, 1099.

(34) The single-crystal X-ray diffraction structure of an amine-stabilized carbamic acid was disclosed during the preparation of the manuscript: Inagaki, F.; Matsumoto, C.; Iwata, T.; Mukai, C. *J. Am. Chem. Soc.* **2017**, *139*, 4639. However, the NMR and structural evidence could also be consistent with complete proton transfer to form an ammonium carbamate species.

(35) After this manuscript was accepted, an adsorbent was disclosed that NMR experiments suggest forms carbamic acids, although no crystallographic evidence was provided. See: Flaig, R. W.; Osborn Popp, T. M.; Fracaroli, A. M.; Kapustin, E. A.; Kalmutzki, M. J.; Altamimi, R. M.; Fathieh, F.; Reimer, J. A.; Yaghi, O. M. *J. Am. Chem. Soc.* **2017**, *139*, 12125.

DOI: 10.1021/jacs.7b07612
J. Am. Chem. Soc. 2017, 139, 13541−13553

Supporting Information for

A Diaminopropane-Appended Metal–Organic Framework Enabling Efficient CO_2 Capture from Coal Flue Gas via a Mixed Adsorption Mechanism

Phillip J. Milner,[†] Rebecca L. Siegelman,[†] Alexander C. Forse,[†,‡,#] Miguel I. Gonzalez,[†] Tomče Runčevski,[†] Jeffrey D. Martell,[†] Jeffrey A. Reimer,[#] Jeffrey R. Long*[,†,#,§]

[†]Department of Chemistry, [‡]Berkeley Energy and Climate Institute, and [#]Department of Chemical and Biomolecular Engineering, University of California, Berkeley, California 94720, United States

[§]Materials Sciences Division, Lawrence Berkeley National Laboratory, Berkeley, California 94720

* Correspondence to: jrlong@berkeley.edu

Table of contents **Page**

1. Procedures for large-scale preparations of M_2(dobpdc) (M = Mg, Mn, Co, Ni, Zn).

These procedures are adapted from the literature.[1,2]

Mg_2(dobpdc).[2] An Erlenmeyer flask was charged with $Mg(NO_3)_2 \cdot 6H_2O$ (5.75 g, 22.5 mmol, 1.24 eq.), 4,4′-dihydroxy-[1,1′-biphenyl]-3,3′-dicarboxylic acid (4.95 g, 18.0 mmol, 1.00 eq.), *N,N*-dimethylformamide (45 mL), and methanol (55 mL). The mixture was sonicated until all of the solids dissolved. The mixture was filtered through filter paper into a 300 mL screw-cap high pressure reaction vessel equipped with a stir bar. The reaction mixture was sparged with N_2 for 1 h. The reaction vessel was sealed, and the reaction mixture was allowed to stir slowly at 120 °C for 14 h, resulting in precipitation of a white solid from solution. The non-homogenous mixture was filtered, and the solid was quickly transferred to a Pyrex jar filled with *N,N*-dimethylformamide (250 mL). The jar was placed in an oven heated to 60 °C and allowed to stand for at least 3 h, at which time the jar was cooled to room temperature and the solvent was decanted and replaced with fresh *N,N*-dimethylformamide (250 mL). The jar was reheated to 60 °C, and this washing process was repeated a total of three times. Next, the *N,N*-dimethylformamide was replaced with methanol (250 mL), and the washing process was repeated an additional three times using methanol. A small portion of the solid was removed and placed in a vial under flowing N_2. The solid was activated under flowing N_2 at 180 °C for 24 h, transferred to a glass adsorption tube equipped with a Micromeritics *TransSeal*, and activated for an additional 24 h under high vacuum

---

[1] McDonald, T. M.; Mason, J. A.; Kong, X.; Bloch, E. D.; Gygi, D.; Dani, A.; Crocellà, V.; Giordanino, F.; Odoh, S. O.; Drisdell, W. S.; Vlaisavljevich, B.; Dzubak, A. L.; Poloni, R.; Schnell, S. K.; Planas, N.; Lee, K.; Pascal, T.; Wan, L. F.; Prendergast, D.; Neaton, J. B.; Smit, B.; Kortright, J. B.; Gagliardi, L.; Bordiga, S.; Reimer, J. A.; Long, J. R. *Nature* **2015**, *519*, 303.
[2] Siegelman, R. L.; McDonald, T. M.; Gonzalez, M, I. C.; Martell, J. D.; Milner, P. J.; Mason, J. A.; Berger, A. H.; Bhown, A. S.; Long, J. R. *J. Am. Chem. Soc.* **2017**, *Just Accepted* (DOI: 10.1021/jacs.7b05858).

(<10 μbar) at 180 °C. Activated Mg_2(dobpdc) was obtained as a white solid. Langmuir surface area (77 K, N_2): 3934 ± 19 m^2/g.

Mn_2(dobpdc).[1] An Erlenmeyer flask was charged with $MnCl_2 \cdot 4H_2O$ (990 mg, 5.00 mmol, 2.50 eq.), 4,4′-dihydroxy-[1,1′-biphenyl]-3,3′-dicarboxylic acid (548 mg, 2.00 mmol, 1.00 eq.), *N,N*-dimethylformamide (100 mL), and ethanol (100 mL). The mixture was sonicated until all of the solids dissolved. The mixture was filtered through filter paper into a 300 mL screw-cap high pressure reaction vessel equipped with a stir bar. The reaction mixture was sparged with N_2 for 1 h. The reaction vessel was sealed, and the reaction mixture was allowed to stir slowly at 120 °C for 14 h, resulting in precipitation of a pale yellow solid from solution. The non-homogenous mixture was filtered, and the solid was quickly transferred to a Pyrex jar filled with *N,N*-dimethylformamide (250 mL). The jar was placed in an oven heated to 60 °C and allowed to stand for at least 3 h, at which time the jar was cooled to room temperature and the solvent was decanted and replaced with fresh *N,N*-dimethylformamide (250 mL). The jar was reheated to 60 °C, and this washing process was repeated a total of three times. Next, the *N,N*-dimethylformamide was replaced with methanol (250 mL), and the washing process was repeated an additional three times using methanol. A small portion of the solid was removed and placed in a vial under flowing N_2. The solid was activated under flowing N_2 at 180 °C for 24 h, transferred to a glass adsorption tube equipped with a Micromeritics *TransSeal*, and activated for an additional 24 h under high vacuum (<10 μbar) at 180 °C. Activated Mn_2(dobpdc) was obtained as a pale yellow solid. Langmuir surface area (77 K, N_2): 3418 ± 13 m^2/g.

Co_2(dobpdc).[1] An Erlenmeyer flask was charged with $Co(NO_3)_2 \cdot 6H_2O$ (1.09 g, 3.75 mmol, 2.50 eq.), 4,4′-dihydroxy-[1,1′-biphenyl]-3,3′-dicarboxylic acid (411 mg, 1.50 mmol, 1.00 eq.), deionized water (50 mL), *N,N*-dimethylformamide (50 mL), and ethanol (50 mL). The mixture

was sonicated until all of the solids dissolved. The mixture was filtered through filter paper into a 300 mL screw-cap high pressure reaction vessel equipped with a stir bar. The reaction mixture was sparged with N_2 for 1 h. The reaction vessel was sealed, and the reaction mixture was allowed to stir slowly at 120 °C for 14 h, resulting in precipitation of a pink solid from solution. The non-homogenous mixture was filtered, and the pink solid was quickly transferred to a Pyrex jar filled with *N,N*-dimethylformamide (250 mL). The jar was placed in an oven heated to 60 °C and allowed to stand for at least 3 h, at which time the jar was cooled to room temperature and the solvent was decanted and replaced with fresh *N,N*-dimethylformamide (250 mL). The jar was reheated to 60 °C, and this washing process was repeated a total of three times. Next, the *N,N*-dimethylformamide was replaced with methanol (250 mL), and the washing process was repeated an additional three times using methanol. A small portion of the solid was removed and placed in a vial under flowing N_2. The solid was activated under flowing N_2 at 180 °C for 24 h, transferred to a glass adsorption tube equipped with a Micromeritics *TransSeal*, and activated for an additional 24 h under high vacuum (<10 μbar) at 180 °C. Activated Co_2(dobpdc) was obtained as a purple solid. Langmuir surface area (77 K, N_2): 3620 ± 14 m^2/g.

Ni_2(dobpdc).[1,3] An Erlenmeyer flask was charged with $Ni(NO_3)_2 \cdot 6H_2O$ (1.09 g, 3.75 mmol, 2.50 eq.), 4,4′-dihydroxy-[1,1′-biphenyl]-3,3′-dicarboxylic acid (411 mg, 1.50 mmol, 1.00 eq.), deionized water (50 mL), *N,N*-dimethylformamide (50 mL), and ethanol (50 mL). The mixture was sonicated until all of the solids dissolved. The mixture was filtered through filter paper into a 250 mL Pyrex jar. The jar was placed in an oven at 120 °C and allowed to stand for 14 h, resulting in precipitation of a bright green solid from solution. The non-homogenous mixture was filtered,

[3] Gygi, D.; Bloch, E. D.; Mason, J. A.; Hudson, M. R.; Gonzalez, M. I.; Siegelman, R. L.; Darwish, T. A.; Queen, W. L.; Brown, C. M.; Long, J. R. *Chem. Mater.* **2016**, *28*, 1128.

and the green solid was quickly transferred to a Pyrex jar filled with *N,N*-dimethylformamide (250 mL). The jar was placed in an oven heated to 60 °C and allowed to stand for at least 3 h, at which time the jar was cooled to room temperature and the solvent was decanted and replaced with fresh *N,N*-dimethylformamide (250 mL). The jar was reheated to 60 °C, and this washing process was repeated a total of three times. Next, the *N,N*-dimethylformamide was replaced with methanol (250 mL), and the washing process was repeated an additional three times using methanol. A small portion of the solid was removed and placed in a vial under flowing N_2. The solid was activated under flowing N_2 at 180 °C for 24 h, transferred to a glass adsorption tube equipped with a Micromeritics *TransSeal*, and activated for an additional 24 h under high vacuum (<10 μbar) at 180 °C. Activated Ni_2(dobpdc) was obtained as a brown solid. Langmuir surface area (77 K, N_2): 3215 ± 32 m^2/g.

Zn_2(dobpdc).[2] A Schlenk flask equipped with a stir bar was charged with $ZnBr_2 \cdot 2H_2O$ (8.35 g, 32.0 mmol, 3.20 eq.), 4,4′-dihydroxy-[1,1′-biphenyl]-3,3′-dicarboxylic acid (2.74 g, 10.0 mmol, 1.00 eq.), fresh *N,N*-dimethylformamide (250 mL), and ethanol (250 mL). The mixture was stirred under N_2 until all of the solids dissolved. The mixture was sparged with N_2 for 1 h. The Schlenk flask was sealed under positive N_2 pressure and placed in an oil bath that had been preheated to 120 °C and allowed to stir at this temperature for 14 h, resulting in precipitation of an off-white solid from solution. The reaction mixture was cooled to room temperature and the solid was allowed to settle. The solvent was carefully removed by cannulation under N_2 and replaced with fresh, degassed *N,N*-dimethylformamide (200 mL). The mixture was allowed to stand for at least 24 h, at which time the Schlenk flask was cooled to room temperature, the solid was allowed to settle, and the solvent was removed by cannulation and replaced with fresh, degassed *N,N*-dimethylformamide (200 mL). The flask was reheated to 60 °C, and this washing process was

repeated a total of three times. Next, the *N,N*-dimethylformamide was replaced with degassed methanol (200 mL), and the washing process was repeated an additional three times using methanol. The solvent was removed under high vacuum at 180 °C in the Schlenk flask. The flask was transferred to a N_2-filled glovebox, and the solid was transferred to a glass adsorption tube equipped with a Micromeritics *TransSeal*. The sample was activated for an additional 24 h under high vacuum (<10 μbar) at 180 °C to yield Zn_2(dobpdc) as an off-white solid. Langmuir surface area (77 K, N_2): 3091 ± 7 m^2/g.

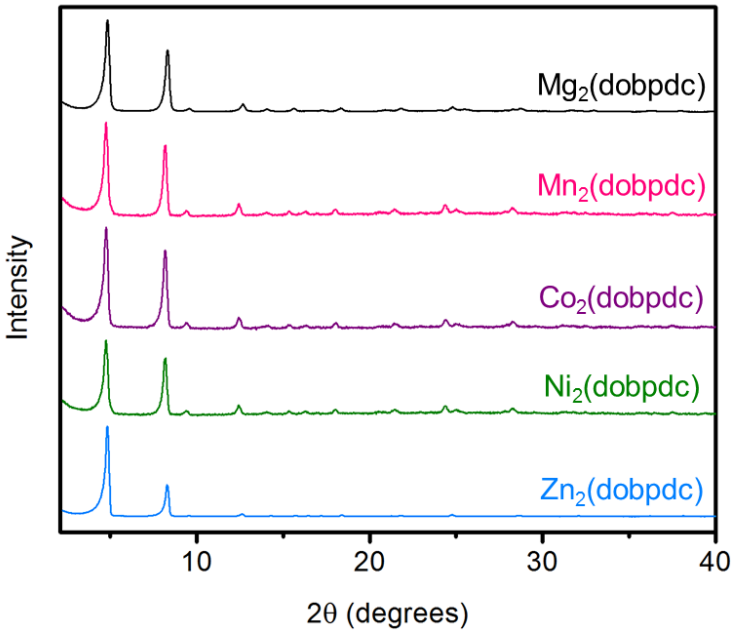

Figure S1. Powder X-ray diffraction patterns (CuKα radiation, λ = 1.5418 Å) of methanol-solvated Mg_2(dobpdc), Mn_2(dobpdc), Co_2(dobpdc), Ni_2(dobpdc), and Zn_2(dobpdc).

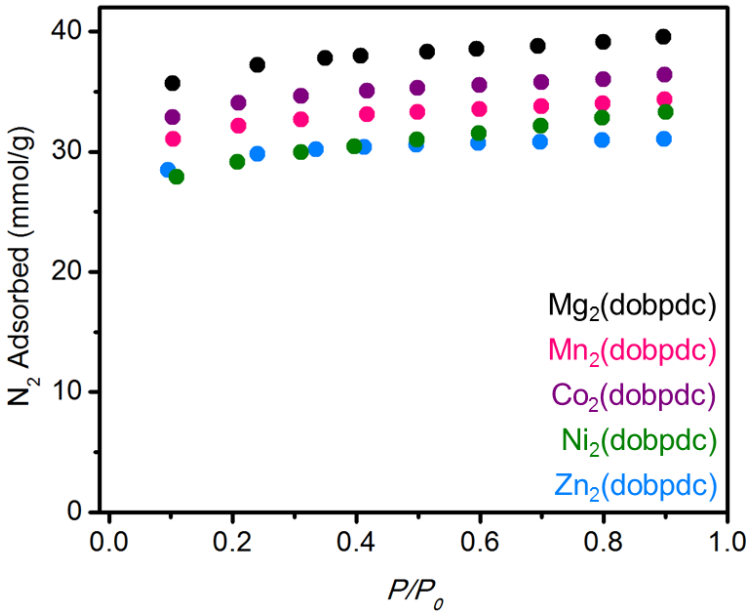

Figure S2. 77 K N_2 adsorption isotherms of activated Mg_2(dobpdc), Mn_2(dobpdc), Co_2(dobpdc), Ni_2(dobpdc), and Zn_2(dobpdc). The Langmuir surface areas calculated from these isotherms are indicated in the experimental procedures above.

2. Characterization and gas adsorption properties of pn–, mpn, and dmpn–Mg_2(dobpdc).

The diamine-appended frameworks pn–, mpn–, and dmpn–Mg_2(dobpdc) were prepared using the procedure outlined in the Experimental section.

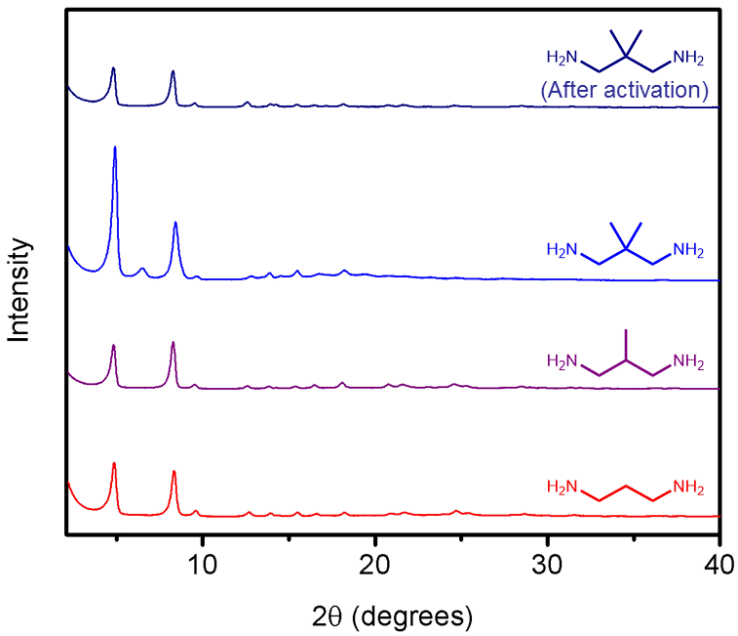

Figure S3. Powder X-ray diffraction patterns (CuKα radiation, λ = 1.5418 Å) of as-synthesized pn– (red), mpn– (purple), and dmpn–Mg_2(dobpdc) (blue), as well as dmpn–Mg_2(dobpdc) after removal of the excess solvated diamine by activation under flowing N_2 at 130 °C for 0.5 h (dark blue). Note that the reflection at approximately 6 degrees in the pattern of dmpn–Mg_2(dobpdc) disappears upon removal of the excess solvated diamine.

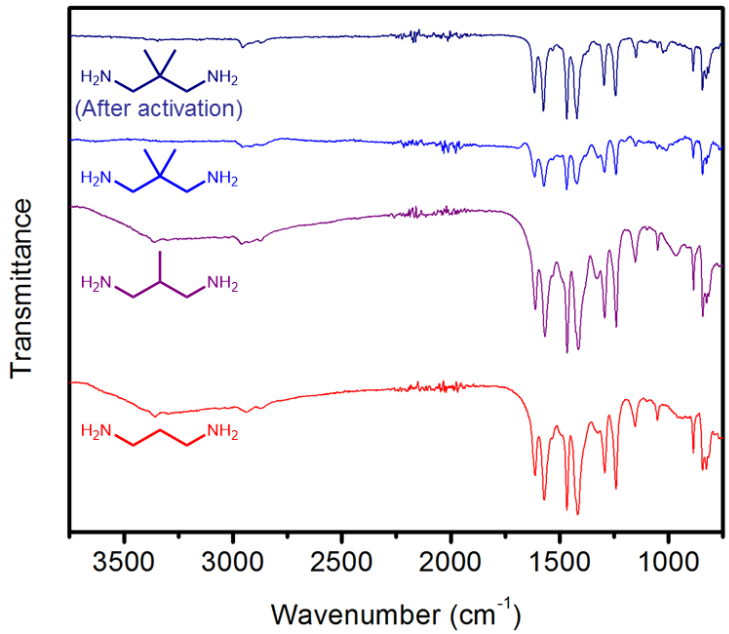

Figure S4. Infrared spectra of as-synthesized pn– (red), mpn– (purple), and dmpn–Mg_2(dobpdc) (blue), as well as dmpn–Mg_2(dobpdc) after removal of the excess solvated diamine by activation under flowing N_2 at 130 °C for 0.5 h (dark blue).

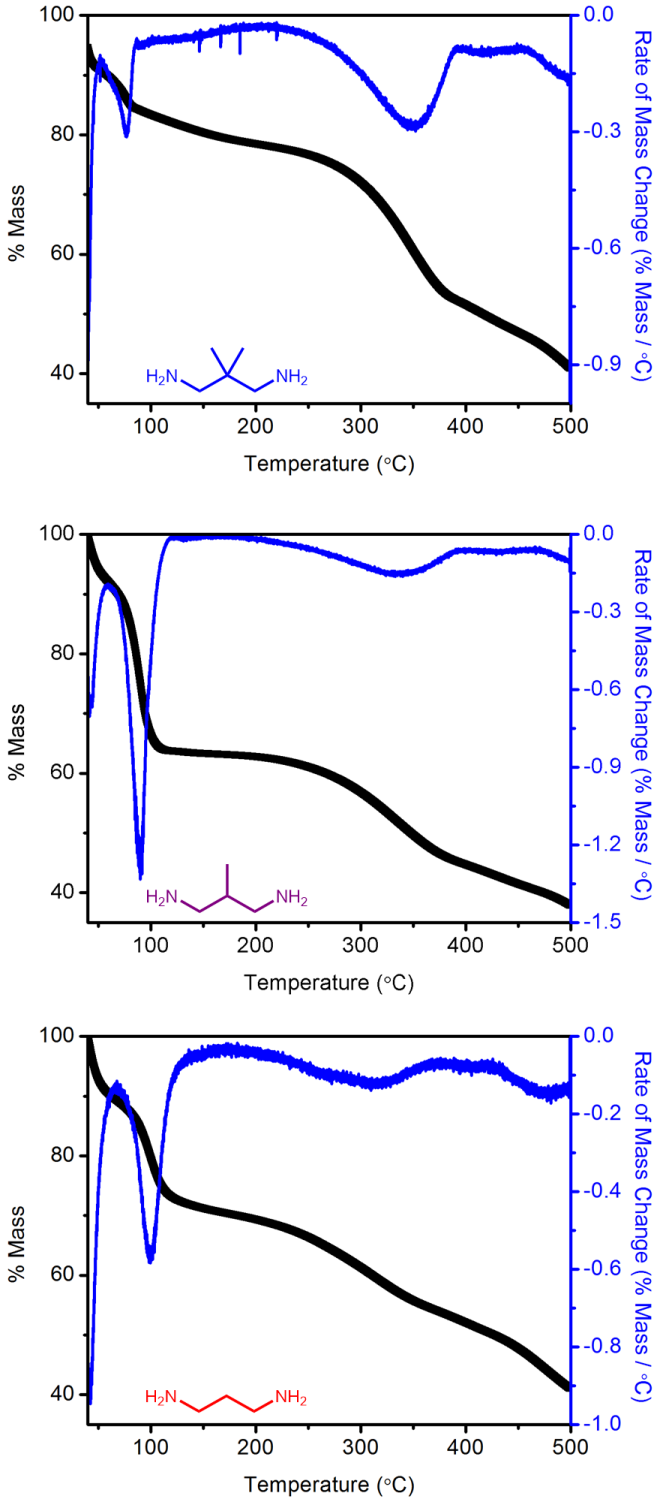

Figure S5. Dry N_2 decomposition profiles of dmpn– (top), mpn– (middle), and pn–Mg_2(dobpdc) (bottom). In each case, the first mass loss (<50 °C) corresponds to weakly adsorbed species (e.g., CO_2, water, toluene), the second mass loss (~100 °C) corresponds to excess diamine, and the third mass loss (max ~300–350 °C) corresponds to metal-bound diamine. A ramp rate of 1.5 °C/min was used.

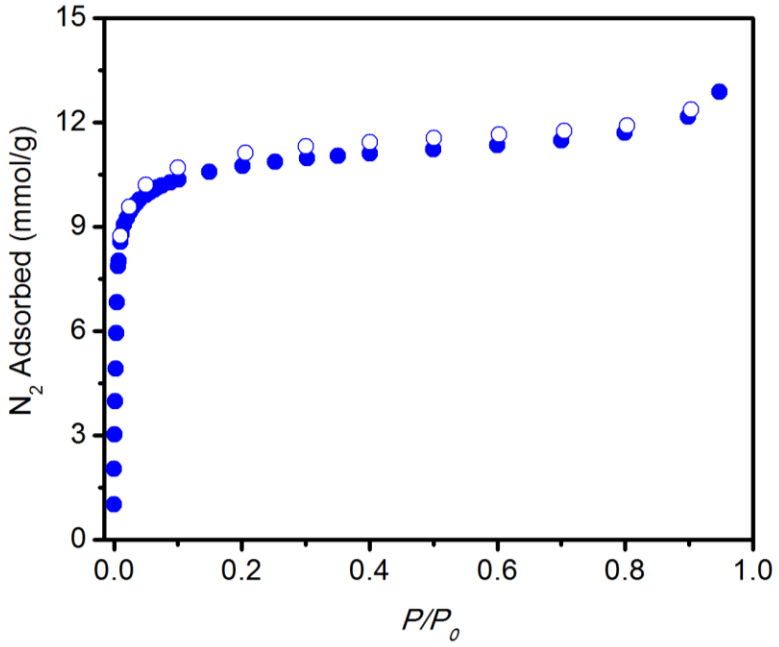

Figure S6. 77 K N_2 adsorption isotherm of activated dmpn–Mg_2(dobpdc). Desorption data are shown with open circles. Fitting these data yielded a Brunauer–Emmett–Teller (BET) surface area of 948 ± 3 m^2/g.

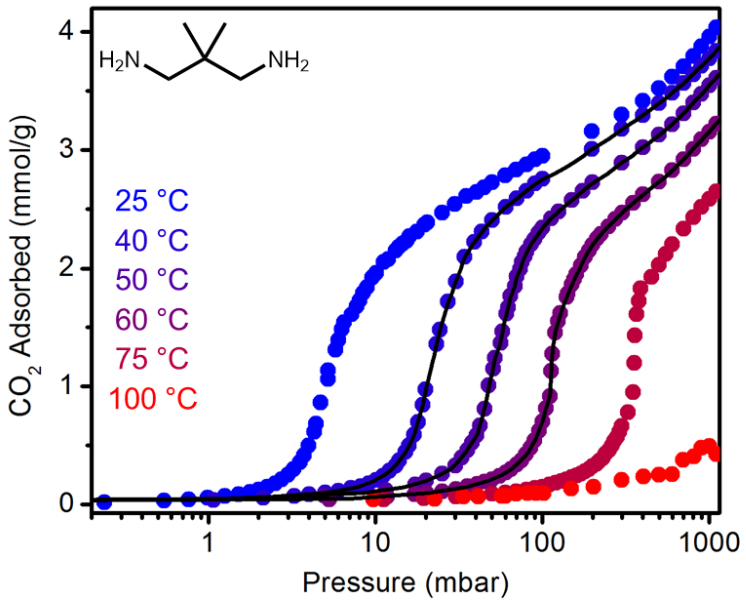

Figure S7. CO_2 adsorption isotherms at 25 °C, 40 °C, 50 °C, 60 °C, 75 °C, and 100 °C, for dmpn–Mg_2(dobpdc). The 40 °C, 50 °C, and 60 °C isotherms were fit by linear interpolation (these isotherms were chosen to match those fit for pn– and mpn–Mg_2(dobpdc)). One CO_2 per diamine corresponds to 3.8 mmol/g. The sample was activated under flowing N_2 at 150 °C for 0.5 h, followed by activation under high vacuum (<10 μbar) at 100 °C for 4 h. The sample was reactivated under high vacuum (<10 μbar) at 100 °C for 2–4 h between isotherms.

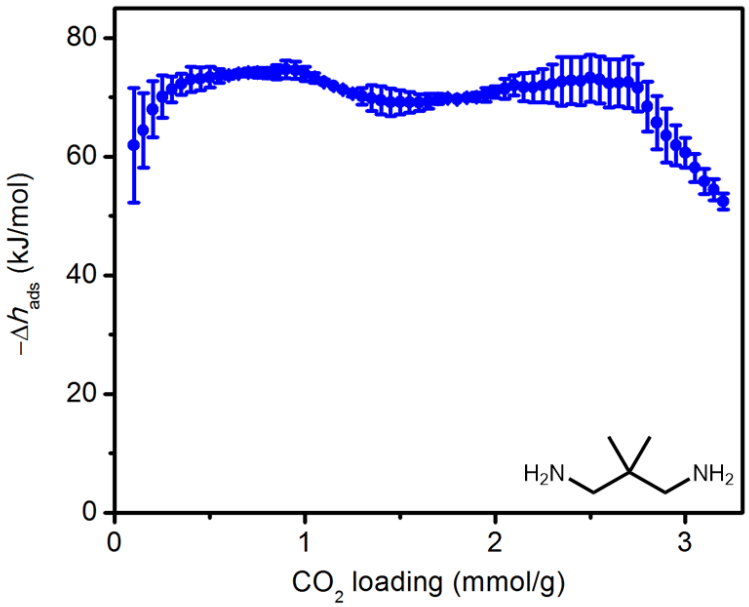

Figure S8. CO_2 differential heats of adsorption for dmpn–Mg_2(dobpdc), determined using the Clausius–Clapeyron equation and the fits shown in Figure S7. One CO_2 per diamine corresponds to 3.8 mmol/g.

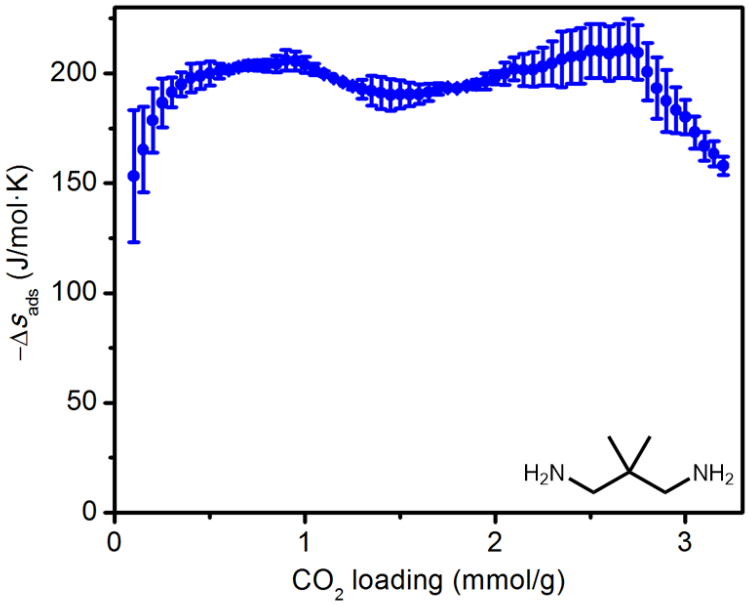

Figure S9. CO_2 differential entropies of adsorption for dmpn–Mg_2(dobpdc), determined from the *y*-intercepts of the linear fits of ln(*p*) vs 1/*T* at constant loadings using the fits shown in Figure S7. One CO_2 per diamine corresponds to 3.8 mmol/g.

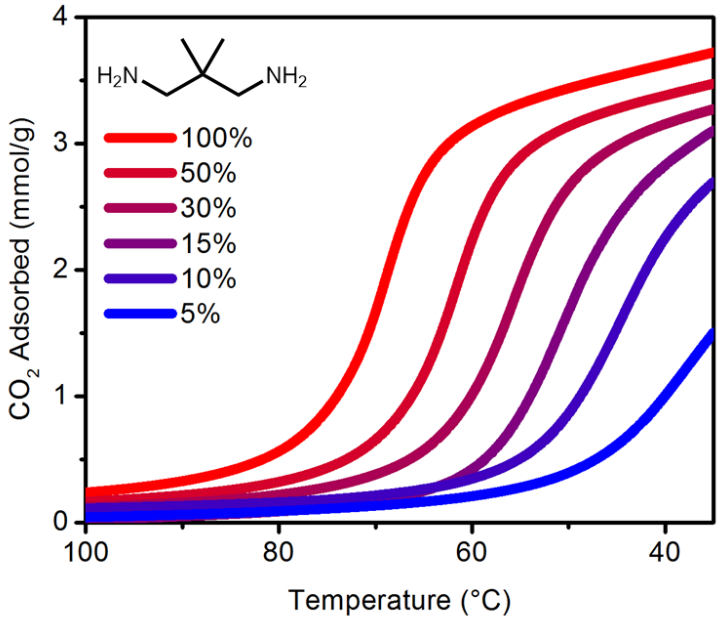

Figure S10. Isobars of dmpn–Mg_2(dobpdc) cooled under different mixtures of CO_2 and N_2, designated by %CO_2 in the gas stream. Samples were activated at 130 °C for 20 min and cooled at a rate of 2 °C/min under the indicated gas stream. One CO_2 per diamine corresponds to 3.8 mmol/g.

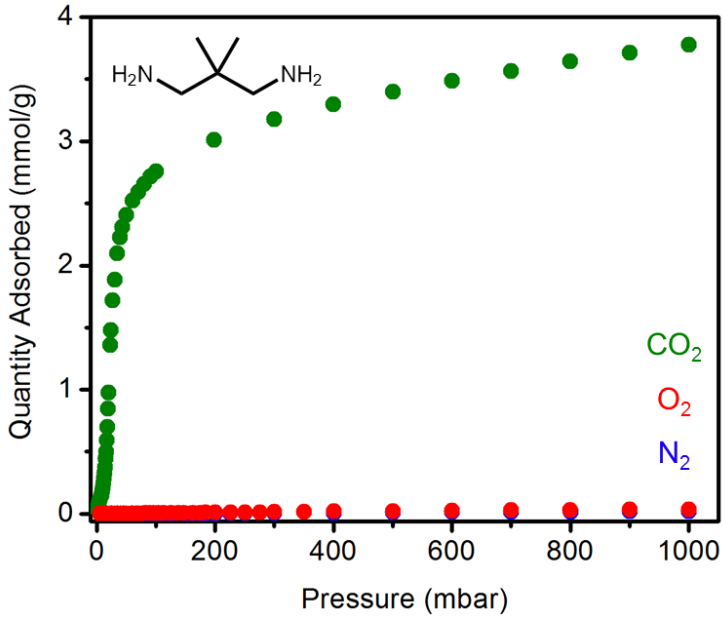

Figure S11. CO_2 (green), O_2 (red), and N_2 (blue) adsorption isotherms of dmpn–Mg_2(dobpdc) at 40 °C.

Table S1. Adsorption capacities and estimated noncompetitive selectivities for CO_2 over O_2 and N_2 in dmpn–Mg_2(dobpdc) at 40 °C.

Gas	Partial Pressure (mbar)[a]	Quantity Adsorbed (mmol/g)	Selectivity $(q_{CO_2}/q_{gas})/(p_{CO_2}/p_{gas})$
CO_2	150	2.91	-
O_2	40	0.0015	517
N_2	750	0.0165	882

[a]Approximate values in coal flue gas.

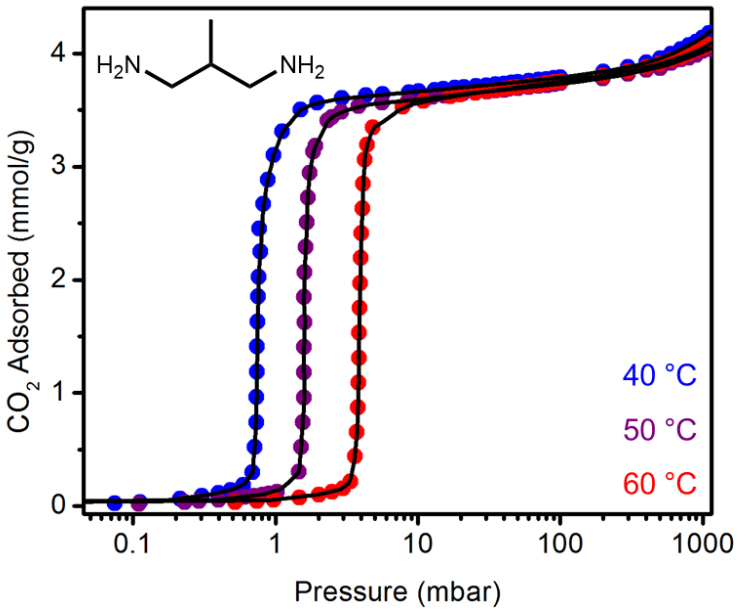

Figure S12. CO_2 adsorption isotherms at 40 °C (blue), 50 °C (purple) and 60 °C (red) for mpn–Mg_2(dobpdc). The shown fits were determined by linear interpolation. One CO_2 per diamine corresponds to 4.0 mmol/g. The sample was activated under flowing N_2 at 150 °C for 0.5 h, followed by activation under high vacuum (<10 μbar) at 100 °C for 4 h. The sample was reactivated under high vacuum (<10 μbar) at 100 °C for 2–4 h between isotherms.

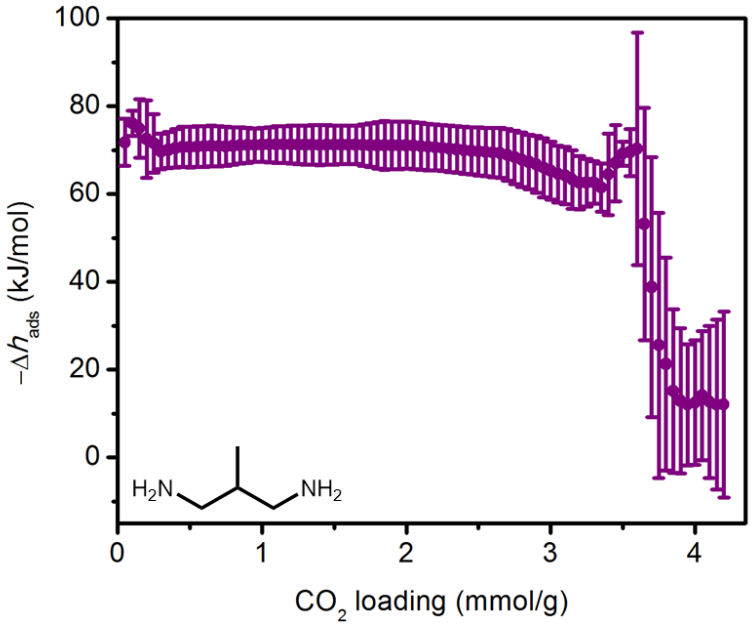

Figure S13. CO_2 differential heats of adsorption for mpn–Mg_2(dobpdc), determined using the Clausius–Clapeyron equation and the fits shown in Figure S12. One CO_2 per diamine corresponds to 4.0 mmol/g.

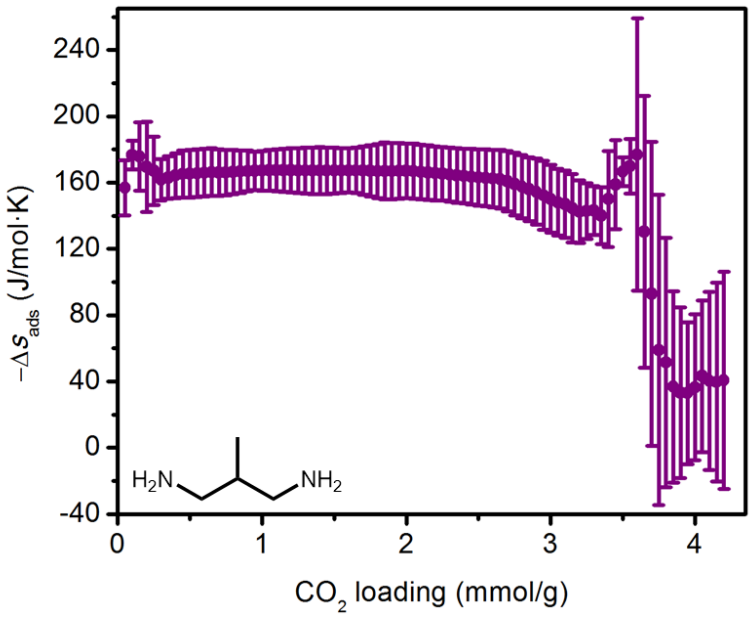

Figure S14. CO_2 differential entropies of adsorption for mpn–Mg_2(dobpdc), determined from the *y*-intercepts of the linear fits of ln(*p*) vs 1/*T* at constant loadings using the fits shown in Figure S12. One CO_2 per diamine corresponds to 4.0 mmol/g.

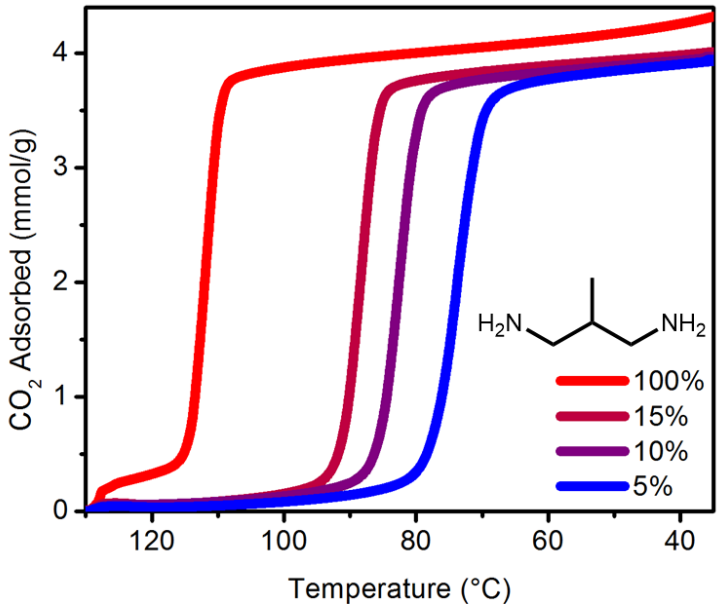

Figure S15. Isobars of mpn–Mg_2(dobpdc) cooled under different mixtures of CO_2 and N_2, designated by %CO_2 in the gas stream. Samples were activated at 130 °C for 20 min and cooled at a rate of 2 °C/min under the indicated gas stream. One CO_2 per diamine corresponds to 4.0 mmol/g.

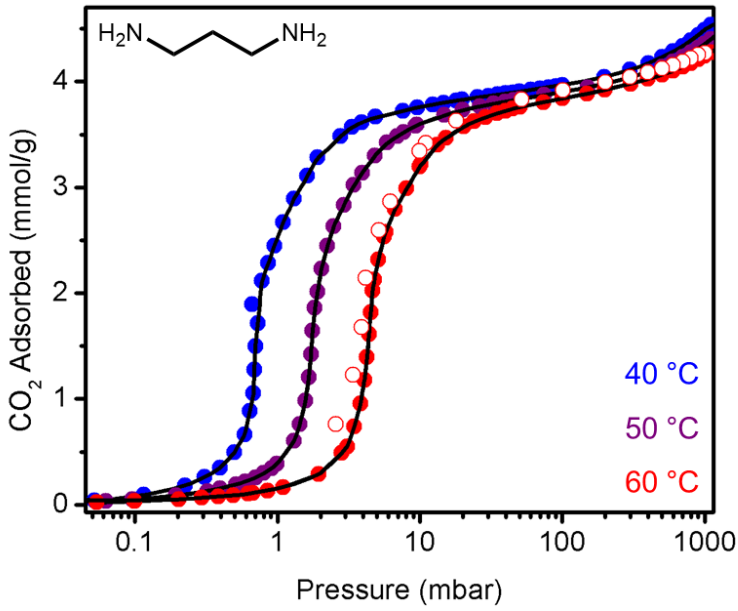

Figure S16. CO_2 adsorption isotherms at 40 °C (blue), 50 °C (purple) and 60 °C (red) for pn–Mg_2(dobpdc). The shown fits were determined by linear interpolation. Desorption data at 60 °C (open circles) are shown, confirming the lack of hysteresis upon CO_2 desorption in this material. One CO_2 per diamine corresponds to 4.3 mmol/g. The sample was activated under flowing N_2 at 150 °C for 0.5 h, followed by activation under high vacuum (<10 μbar) at 100 °C for 4 h. The sample was reactivated under high vacuum (<10 μbar) at 100 °C for 2–4 h between isotherms.

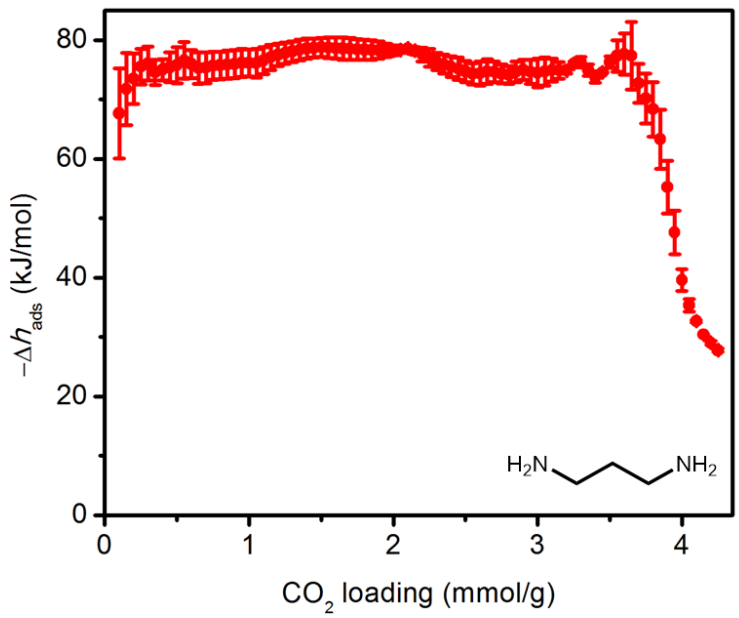

Figure S17. CO_2 differential heats of adsorption for pn–Mg_2(dobpdc), determined using the Clausius–Clapeyron equation and the fits shown in Figure S16. One CO_2 per diamine corresponds to 4.3 mmol/g.

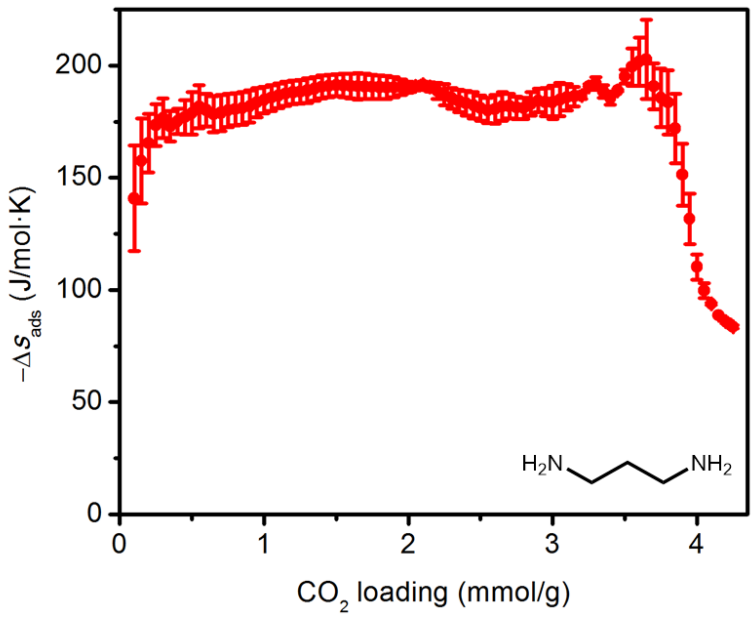

Figure S18. CO_2 differential entropies of adsorption for pn–Mg_2(dobpdc), determined from the *y*-intercepts of the linear fits of ln(*p*) vs 1/*T* at constant loadings using the fits shown in Figure S16. One CO_2 per diamine corresponds to 4.3 mmol/g.

3. Preparation and characterization of en–Mg_2(dobpdc), men–Mg_2(dobpdc), dmen–Mg_2(dobpdc), and dmen–Zn_2(dobpdc).

The previously reported diamine-appended frameworks en–Mg_2(dobpdc)[4] (en = 1,2-ethylenediamine), men–Mg_2(dobpdc)[4b] (men = 1-methyl-1,2-ethylenediamine), and dmen–Mg_2(dobpdc)[4b] (dmen = 1,1-dimethyl-1,2-ethylenediamine) were prepared using the procedure outlined in the Experimental section. The diamine-appended framework dmen–Zn_2(dobpdc) was prepared following a slightly modified procedure.[1] A 30 mL scintillation vial was charged with freshly-filtered methanol-solvated Zn_2(dobpdc) (~20 mg) under N_2. The vial was heated at 180 °C for 24 h under flowing N_2. Meanwhile, freshly-ground CaH_2 (~30 mg) was added to a solution of 1 mL of dmen and 4 mL of toluene in a 30 mL scintillation vial equipped with a stir bar. The mixture was stirred at 100 °C under flowing N_2 for 30 min, at which time it was allowed to cool to room temperature and settle overnight. The dried diamine solution and activated Zn_2(dobpdc) were transferred to a N_2-filled glovebag, and the diamine solution was carefully added *via* syringe to the Zn_2(dobpdc) sample, taking care not to disturb the CaH_2. The vial was swirled several times and allowed to stand at room temperature for 24 h. At this time, the mixture was filtered, and the resulting powder was thoroughly washed with successive aliquots of toluene (3 × 20 mL) and allowed to dry on the filter paper for several minutes, yielding ~30 mg of the diamine-appended metal–organic framework.

---

[4](a) Lee, W. R.; Hwang, S. Y.; Ryu, D. W.; Lim, K. S.; Han, S. S.; Moon, D.; Choi, J.; Hong, C. S. *Energy Environ. Sci.* **2014**, *7*, 744; (b) Jo, H.; Lee, W. R.; Kim, N. W.; Jung, H.; Lim, K. S.; Kim, J. E.; Kang, D. W.; Lee, H.; Hiremath, V.; Seo, J. G.; Jin, H.; Moon, D.; Han, S. S.; Hong, C. S. *ChemSusChem* **2017**, *10*, 541.

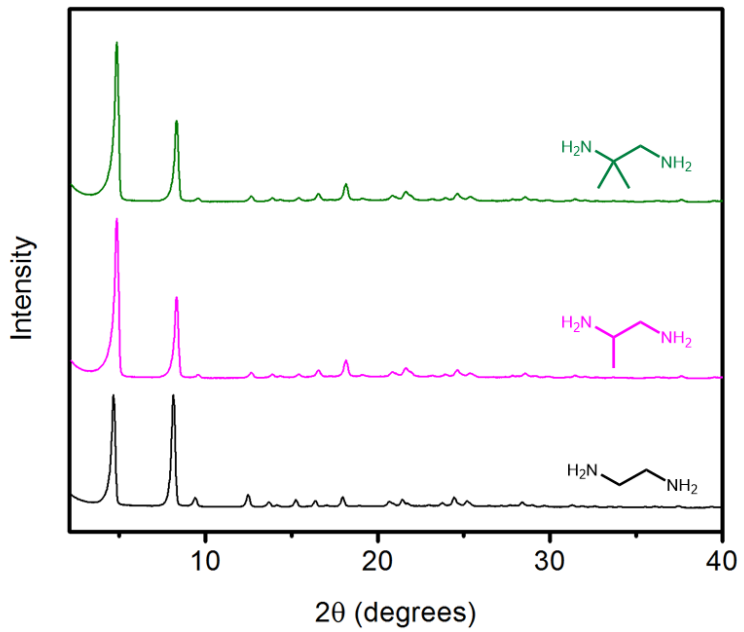

Figure S19. Powder X-ray diffraction pattern (CuKα radiation, λ = 1.5418 Å) of as-synthesized dmen–Mg_2(dobpdc) (green), men–Mg_2(dobpdc) (pink), and en–Mg_2(dobpdc) (black). These patterns are consistent with those reported in the literature.[4]

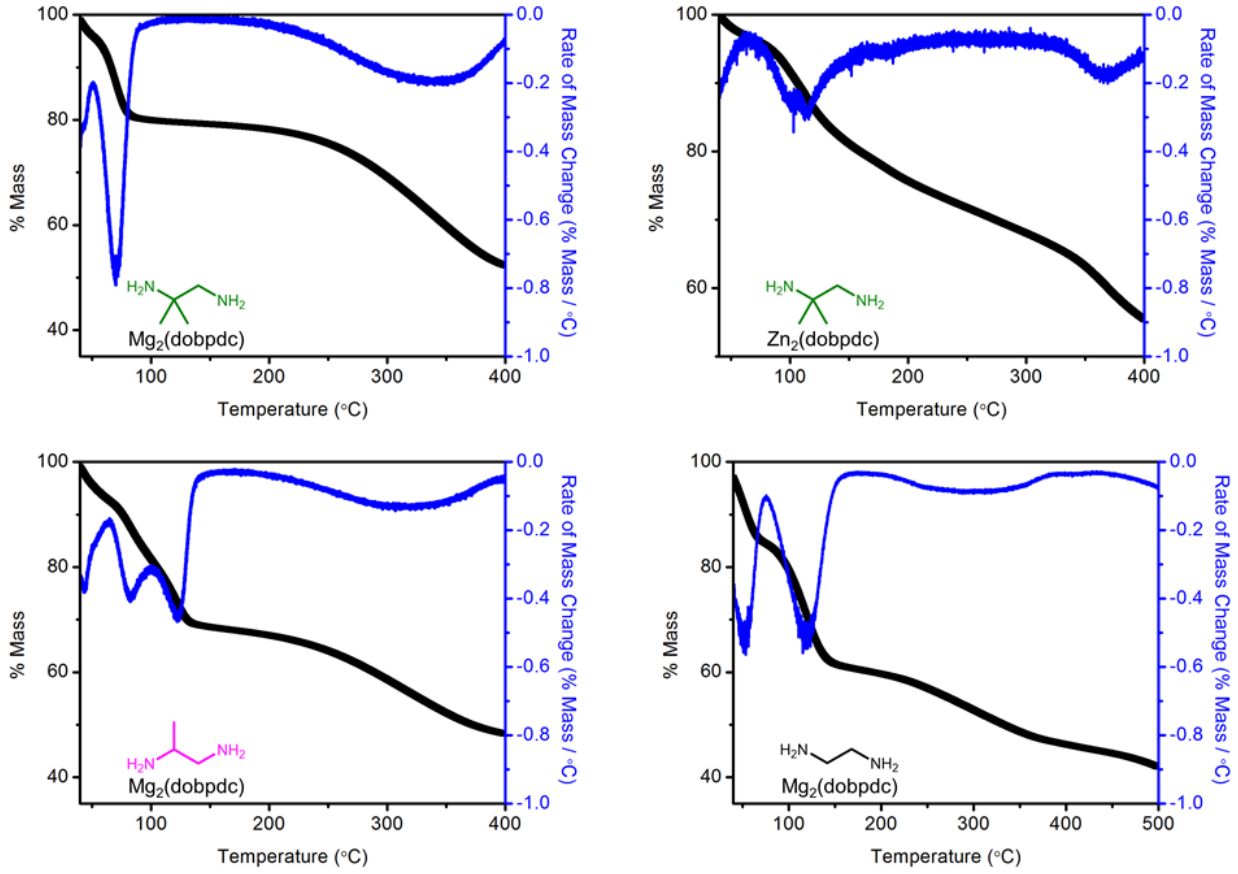

Figure S20. Dry N_2 decomposition profiles of dmen–Mg_2(dobpdc) (top left), dmen–Zn_2(dobpdc) (top right), men–Mg_2(dobpdc) (bottom left), and en–Mg_2(dobpdc) (bottom right). A ramp rate of 1.5 °C/min was used.

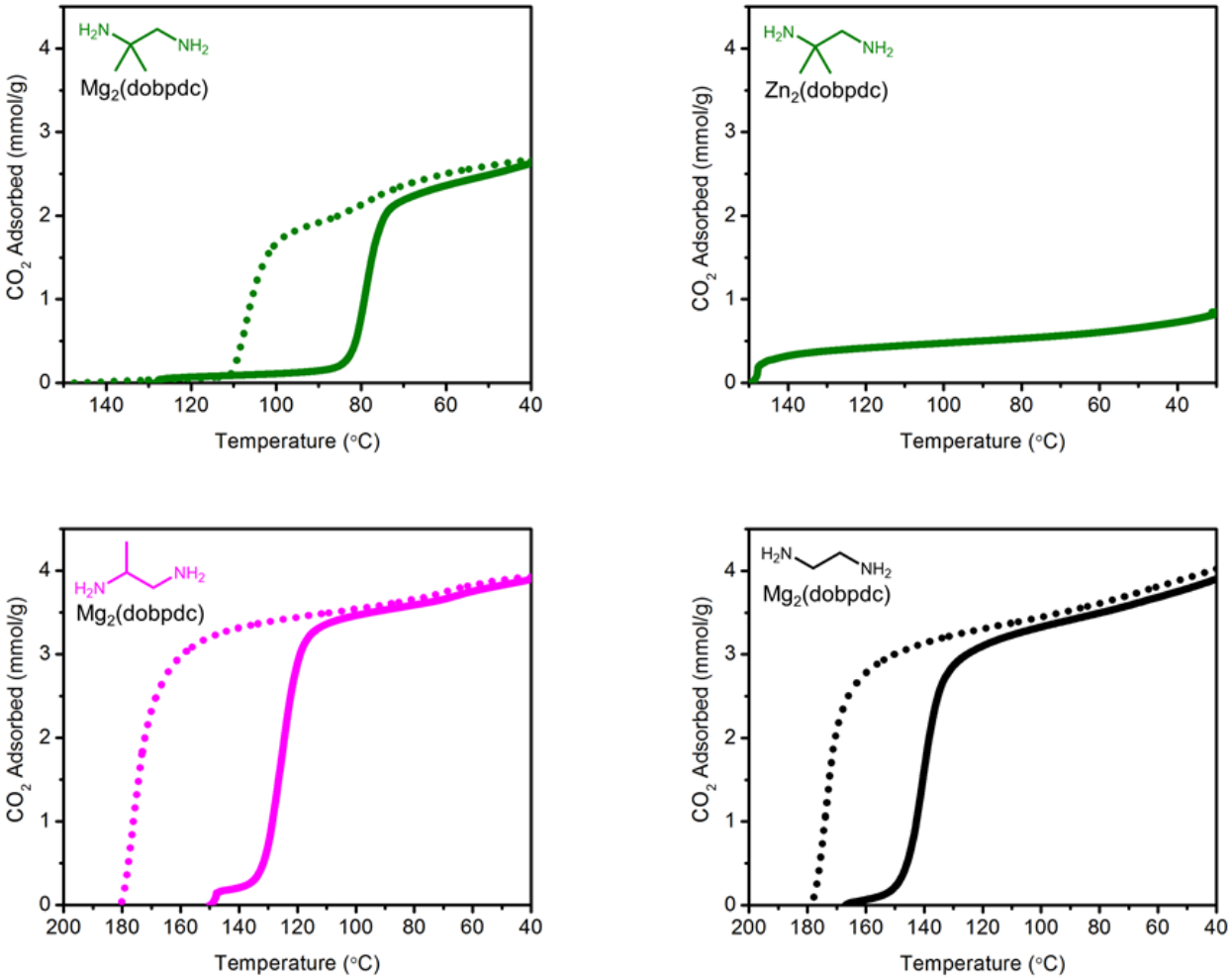

Figure S21. Pure CO_2 adsorption (solid line) and desorption (dotted line) isobars of dmen–Mg_2(dobpdc) (top left), dmen–Zn_2(dobpdc) (top right), men–Mg_2(dobpdc) (bottom left), and en–Mg_2(dobpdc) (bottom right). The pure CO_2 step temperature of dmen–Zn_2(dobpdc) is likely <30 °C and thus could not be reliably observed by thermogravimetric analysis. Note the significantly increased hysteresis upon desorption with these adsorbents compared to the corresponding 1,3-diaminopropanes (Figure 3b). A ramp rate of 1 °C/min was used.

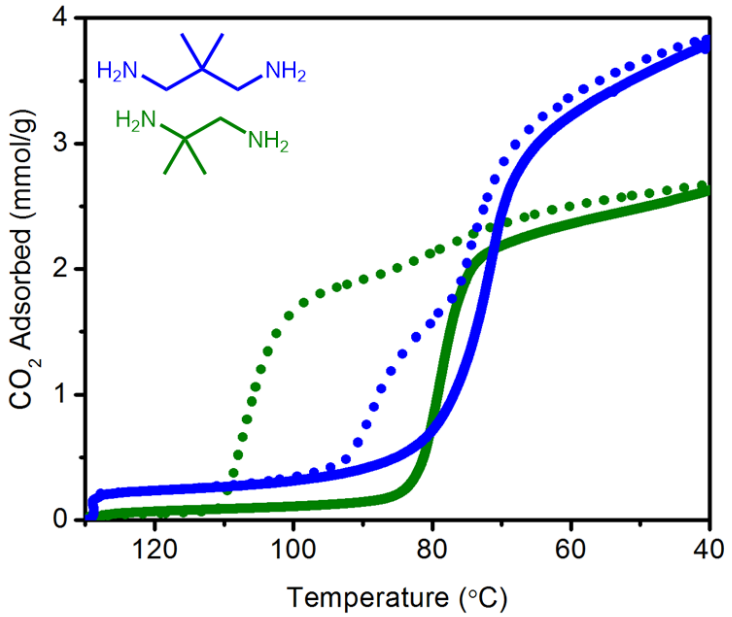

Figure S22. Comparison of pure CO_2 adsorption (solid line) and desorption (dotted line) isobars for dmpn–Mg_2(dobpdc) (blue) and dmen–Mg_2(dobpdc) (green). The material dmpn–Mg_2(dobpdc) possesses a higher CO_2 capacity (3.8 vs. 2.7 mmol/g at 40 °C) and lower pure CO_2 regeneration temperature (95 °C vs. 116 °C) than dmen–Mg_2(dobpdc). A ramp rate of 1 °C/min was used.

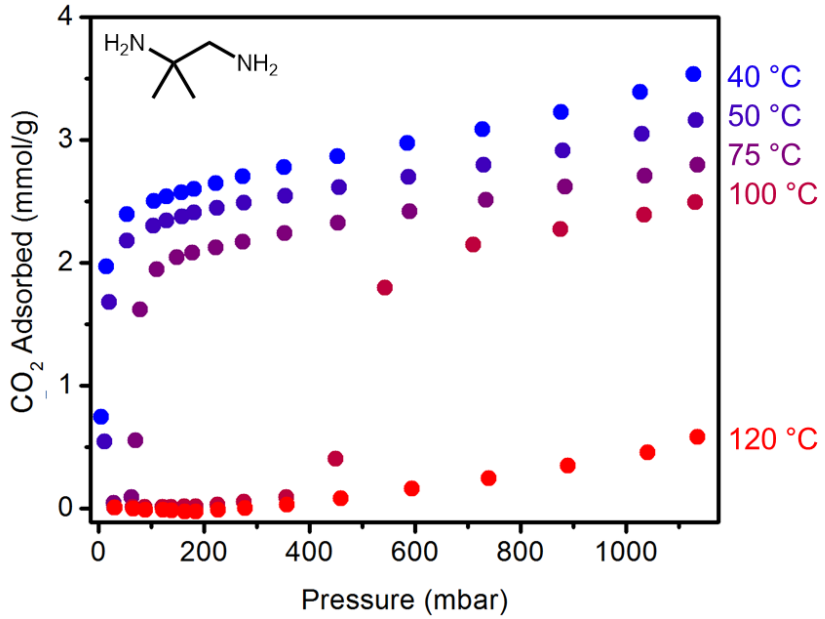

Figure S23. CO_2 adsorption isotherms at 40, 50, 75, 100, and 125 °C for dmen–Mg_2(dobpdc). One CO_2 per diamine corresponds to 4.0 mmol/g. The sample was activated under high vacuum (<10 μbar) at 100 °C for 12 h between isotherms. These isotherms confirm that dmen–Mg_2(dobpdc) possesses an adsorption step at approximately 400 mbar at 100 °C, in contrast to dmpn–Mg_2(dobpdc), which does not display an adsorption step at 100 °C at or below 1 bar (Figure 4).

4. Preparation and characterization of dmpn–Mn_2(dobpdc), Co_2(dobpdc), Ni_2(dobpdc), and Zn_2(dobpdc).

General procedure for preparing dmpn–appended samples of Mn_2(dobpdc), Co_2(dobpdc), and Zn_2(dobpdc).[1] A 30 mL scintillation vial was charged with freshly-filtered methanol-solvated M_2(dobpdc) (~20 mg) under N_2. The vial was heated at 180 °C for 24 h under flowing N_2. Meanwhile, freshly-ground CaH_2 (~30 mg) was added to a solution of 1 mL of dmpn and 4 mL of toluene in a 30 mL scintillation vial equipped with a stir bar. The mixture was stirred at 100 °C under flowing N_2 for 30 min, at which time it was allowed to cool to room temperature and settle overnight. The dried diamine solution and activated M_2(dobpdc) were transferred to a N_2-filled glovebag, and the diamine solution was carefully added *via* syringe to the M_2(dobpdc) sample, taking care not to disturb the CaH_2. Upon addition of the diamine solution, Mn_2(dobpdc) changed from pale yellow to light green, and Co_2(dobpdc) changed from purple to bright pink. The vial was swirled several times and allowed to stand at room temperature for 24 h. At this time, the mixture was filtered, and the resulting powder was thoroughly washed with successive aliquots of toluene (3 × 20 mL) and allowed to dry on the filter paper for several minutes, yielding ~30 mg of the diamine-appended metal-organic framework.

The framework dmpn–Ni_2(dobpdc) was prepared following the procedure outlined in the Experimental section.

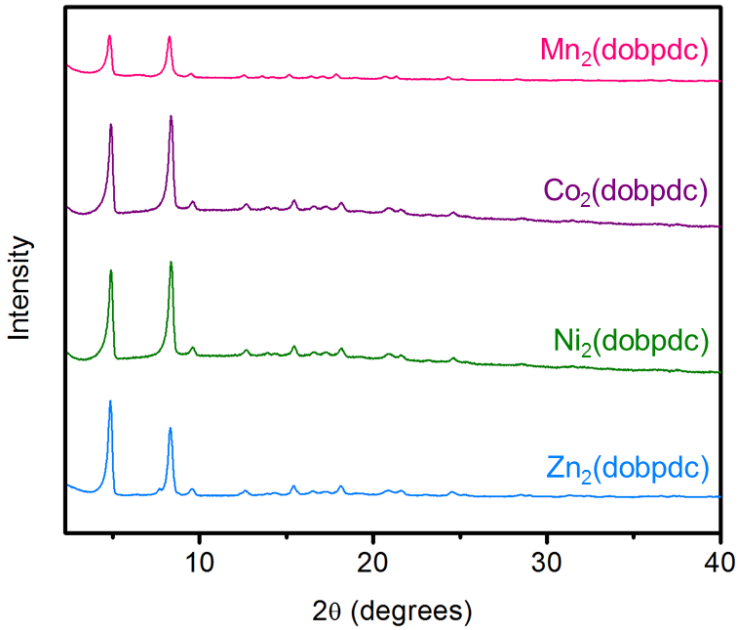

Figure S24. Powder X-ray diffraction patterns (CuKα radiation, λ = 1.5418 Å) of as-synthesized dmpn–Mn_2(dobpdc), Co_2(dobpdc), Ni_2(dobpdc), and Zn_2(dobpdc).

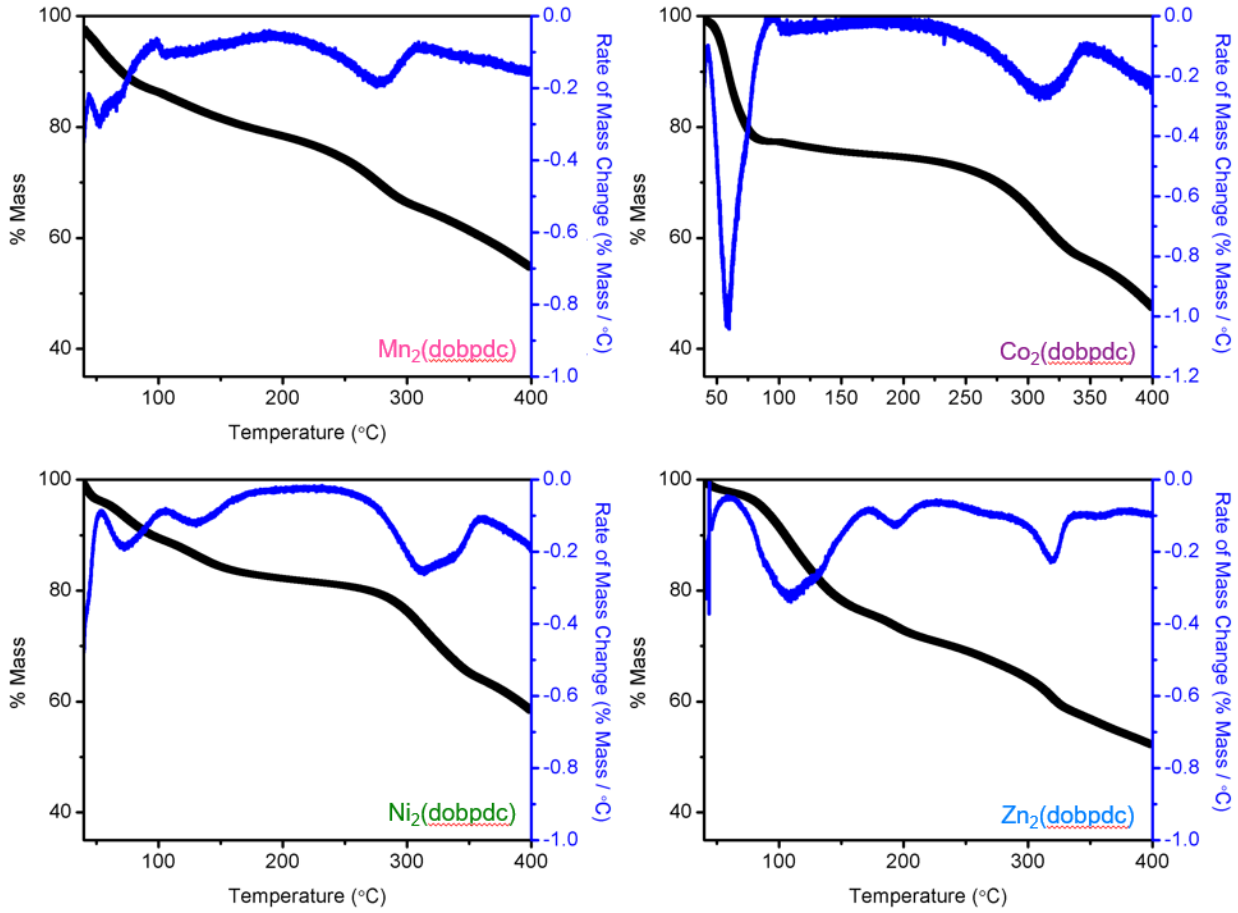

Figure S25. Dry N_2 decomposition profiles of dmpn–Mn_2(dobpdc), Co_2(dobpdc), Ni_2(dobpdc), and Zn_2(dobpdc). The rates of mass loss at each temperature are shown in blue. A ramp rate of 1.5 °C/min was used.

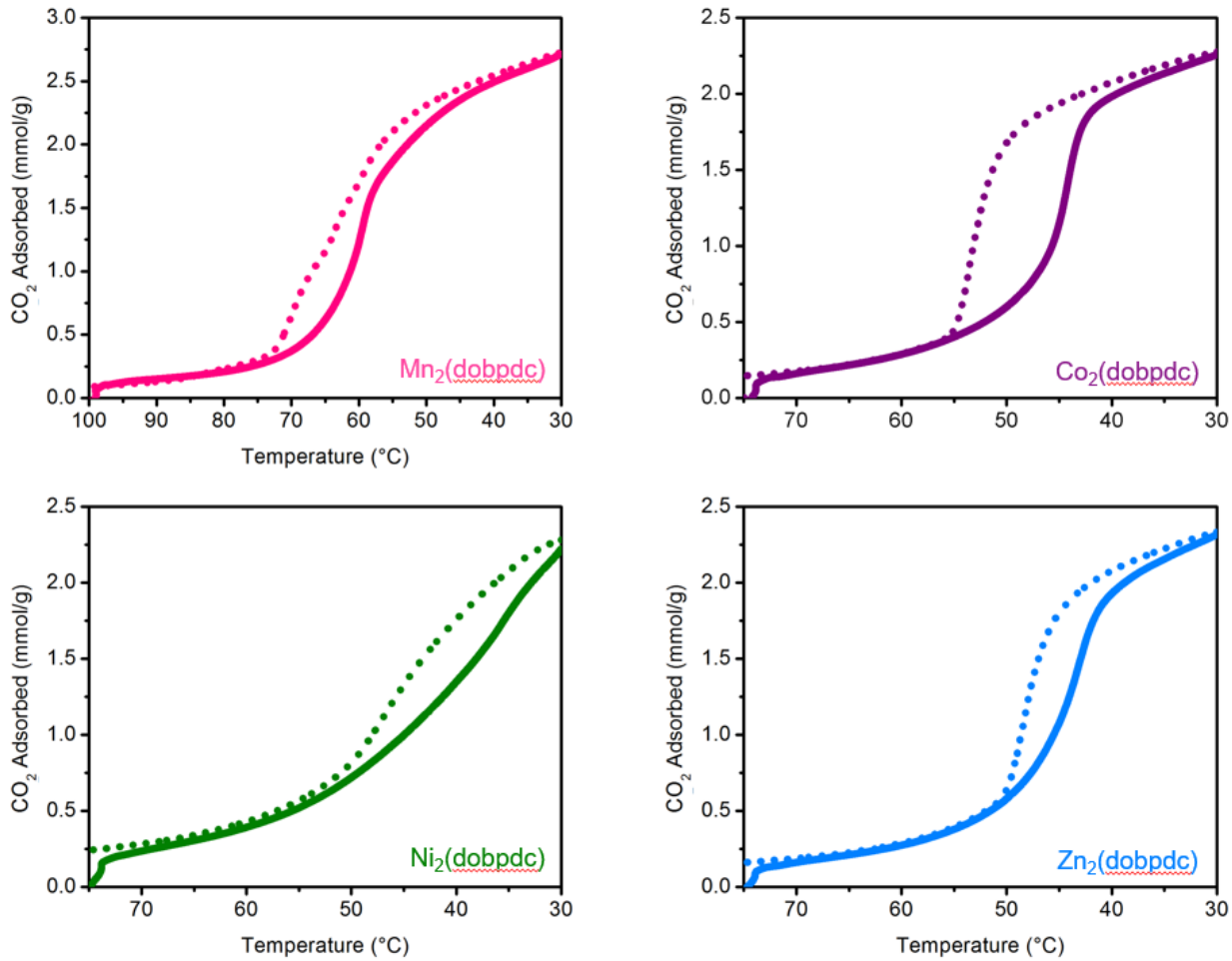

Figure S26. Pure CO_2 adsorption (solid line) and desorption (dotted line) isobars for dmpn–Mn_2(dobpdc), Co_2(dobpdc), Ni_2(dobpdc), and Zn_2(dobpdc). The frameworks dmpn–Zn_2(dobpdc) and Ni_2(dobpdc) were activated at 150 °C under flowing N_2 for 0.5 h, whereas dmpn–Mn_2(dobpdc) and Co_2(dobpdc) were activated at 130 °C under flowing N_2 for 0.5 h. Consistent with the CO_2 isotherms (Figure 9), dmpn–Mn_2(dobpdc), Co_2(dobpdc), and Zn_2(dobpdc) display step-shaped adsorption of CO_2. A ramp rate of 1 °C/min was used.

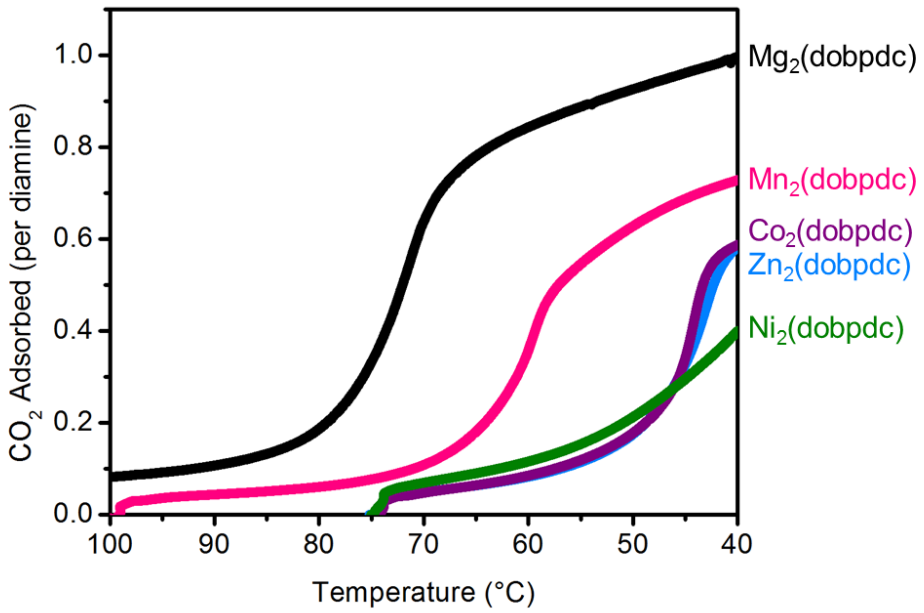

Figure S27. Comparison of pure CO_2 adsorption isobars for dmpn–Mg_2(dobpdc), Mn_2(dobpdc), Co_2(dobpdc), Zn_2(dobpdc), and Ni_2(dobpdc). A ramp rate of 1 °C/min was used.

5. Diamine loadings (Table S2) and CO_2 differential enthalpies and entropies for diamine-appended metal–organic frameworks (Table S3).

General procedure to determine diamine loadings. Approximately 5 mg of diamine-appended metal–organic framework was suspended in 1 mL of DMSO-d_6. Two drops of 35% DCl in D_2O were added, and the vial was sealed. The vial was heated using a heat gun until the solid fully dissolved. The resulting solution was analyzed by ^{1}H NMR (300 MHz) to determine the ratio of diamine to ligand.

Table S2. Typical diamine loadings and activation temperatures for diamine-appended M_2(dobpdc) variants.

Diamine Structure	Diamine Name	M_2(dobpdc)	% Diamine Loading	Activation Temperature (°C)
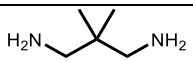	dmpn	Mg	115%[a]	130
	dmpn	Mn	N/d	130
	dmpn	Co	108%	130
	dmpn	Ni	121%	150
	dmpn	Zn	126%[b]	150
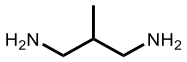	mpn	Mg	135%	150
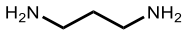	pn	Mg	151%	150
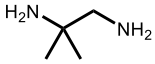	dmen	Mg	140%	130
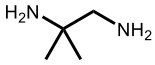	dmen	Zn	143%	150
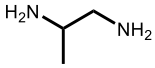	men	Mg	144%	150
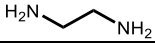	en	Mg	163%	150

N/d = not determined. [a]100% after activation under flowing N_2 at 130 °C for 0.5 h. [b]101% after activation under flowing N_2 at 150 °C for 0.5 h.

Table S3. Differential enthalpies and entropies of adsorption for a number of reported diamine-appended variants of Mg_2(dobpdc) at a loading of 1 mmol/g. The $-\Delta h_{ads}$ and $-\Delta s_{ads}$ for alkylethylenediamine-appended frameworks were reported previously.[2]

Diamine Structure	$-\Delta h_{ads}$ (kJ/mol)	$-\Delta s_{ads}$ (J/mol•K)	$-\Delta g_{ads}$ (kJ/mol) at 40 °C
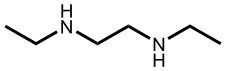	100 ± 4	228 ± 10	29 ± 5
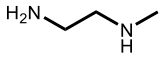	96 ± 3	227 ± 10	25 ± 4
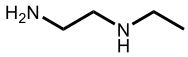	84 ± 3	186 ± 14	25 ± 5
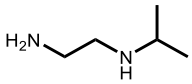	82 ± 3	203 ± 8	18 ± 4
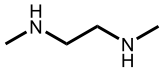	79 ± 1	187 ± 2	21 ± 1
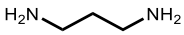	76 ± 2	185 ± 6	18 ± 3
	74 ± 1	204 ± 4	10 ± 2
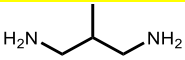	71 ± 4	167 ± 12	19 ± 5
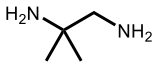	63 ± 4	161 ± 13	13 ± 6
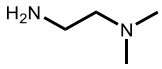	52 ± 1	146 ± 2	6 ± 1
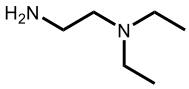	49 ± 4	141 ± 13	5 ± 6
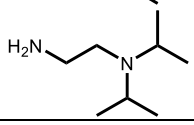	40	128	0

6. Calculation of the approximate regeneration energy of dmpn–Mg_2(dobpdc).

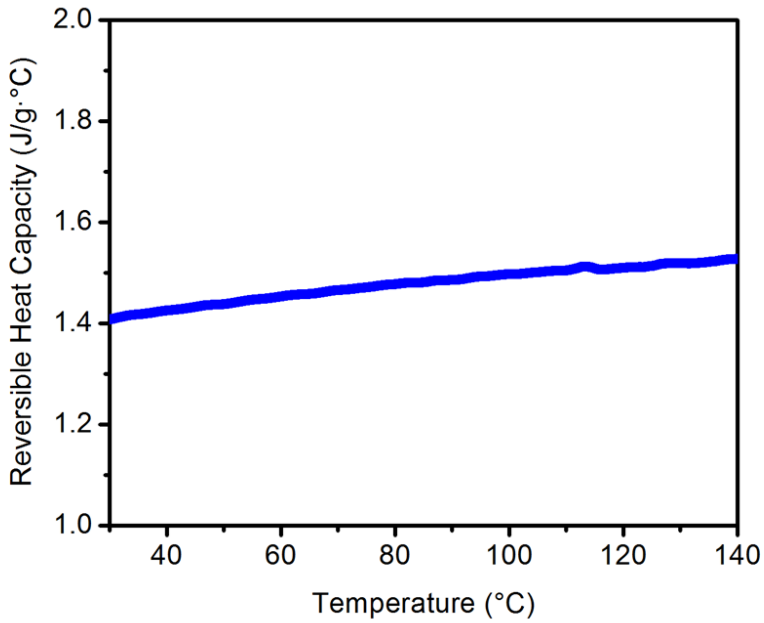

Figure S28. Reversible heat capacity of dmpn–Mg_2(dobpdc), determined by modulated differential scanning calorimetry (DSC) under an atmosphere of He. The ramp rate was 2 °C/min. A modulation frequency of 0.75 °C/80 s was used.

Average reversible heat capacity over the range 40–100 °C: 1.46 J/g•°C

Energy required to heat dmpn–Mg_2(dobpdc) from 40°C to 100 °C: 88 J/g

CO_2 working capacity: 2.42 mmol/g (2.91 mmol/g adsorbed at 150 mbar CO_2, 40 °C; 0.49 mmol/g adsorbed at 1 bar CO_2, 100 °C). This corresponds to 1.27 mol CO_2/mol_{MOF}.

Average isosteric heat from 2.91 to 0.49 mmol/g (determined from Figure S8): 71.5 kJ/mol = 136 kJ/kg. The isosteric heat at a loading of 1 mmol/g is 74.0 kJ/mol = 141 kJ/kg.

Therefore, the approximate energy required to heat dmpn–Mg_2(dobpdc) from 40 to 100 °C while desorbing 2.42 mmol/g of CO_2 is 224 kJ/kg. Using the slightly higher isosteric heat determined at a loading of 1 mmol/g step yields an approximate regeneration energy of 229 kJ/kg.

Cycling 1 kg (22.72 mol) of CO_2 requires 9.36 kg of dmpn–Mg_2(dobpdc). Therefore, the approximate regeneration energy needed to cycle 1 kg of CO_2 is (224 kJ/kgMOF) × (9.36 kg_{MOF}/kg CO_2) = **2.10 MJ/kg CO_2.** Using the isosteric heat at a loading of 1 mmol/g yields an approximate regeneration energy of **2.14 MJ/kg CO_2**.

7. Additional water co-adsorption and adsorption/desorption cycling experiments with dmpn–Mg_2(dobpdc).

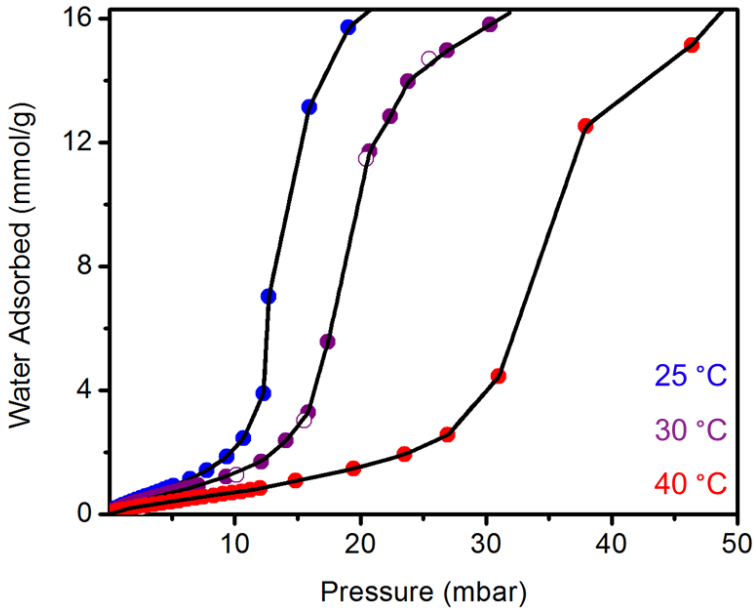

Figure S29. H_2O adsorption isotherms at 25 °C (blue), 30 °C (purple), and 40 °C (red), for dmpn–Mg_2(dobpdc). Desorption data at 30 °C are shown with open circles. The shown fits were determined by linear interpolation.

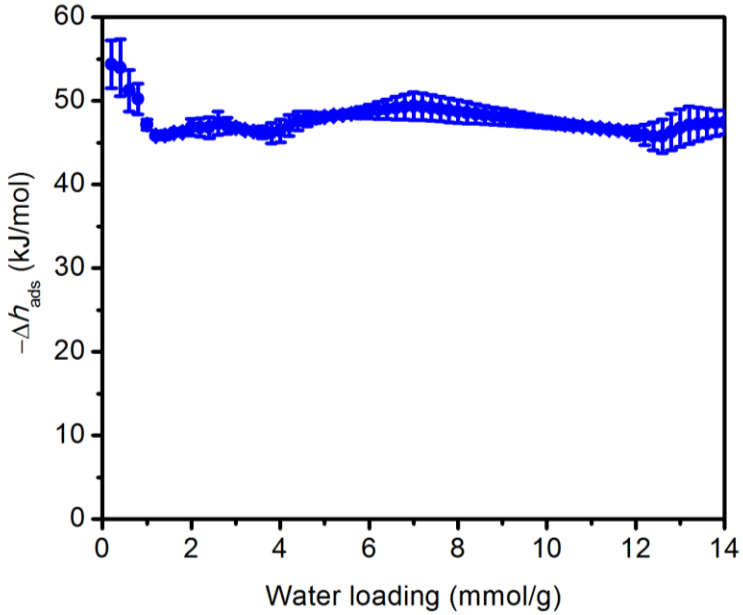

Figure S30. H_2O differential enthalpies of adsorption for dmpn–Mg_2(dobpdc), determined using the Clausius–Clapeyron equation and the fits shown in Figure S29.

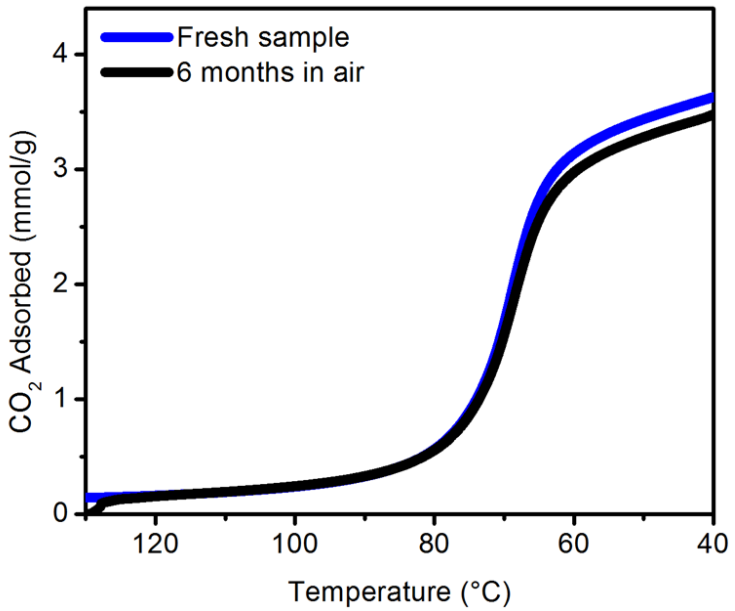

Figure S31. Comparison of the CO_2 isobars of dmpn–Mg_2(dobpdc) prepared as a fresh sample (blue) and after 6 months of air exposure (black). A ramp rate of 1 °C/min was used.

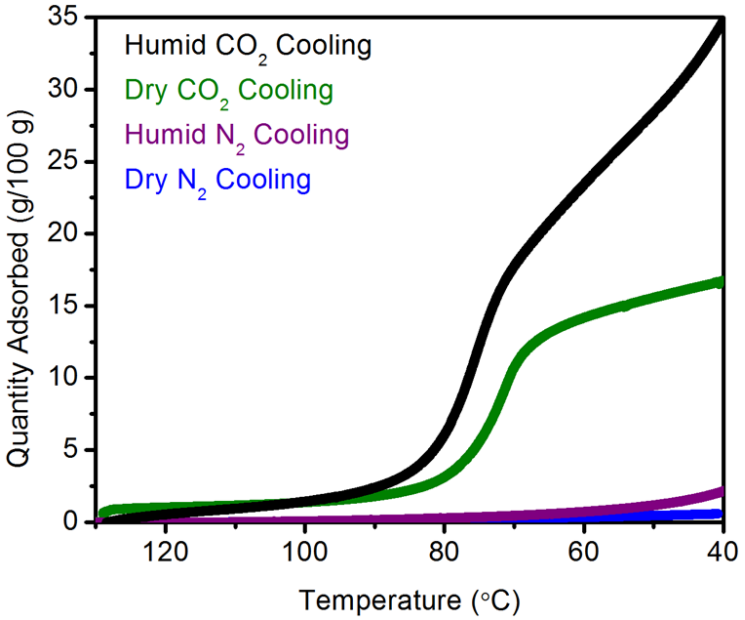

Figure S32. Humid CO_2 (black), dry CO_2 (green), humid N_2 (purple), and dry N_2 (blue) isobars of dmpn–Mg_2(dobpdc). A ramp rate of 1 °C/min was used.

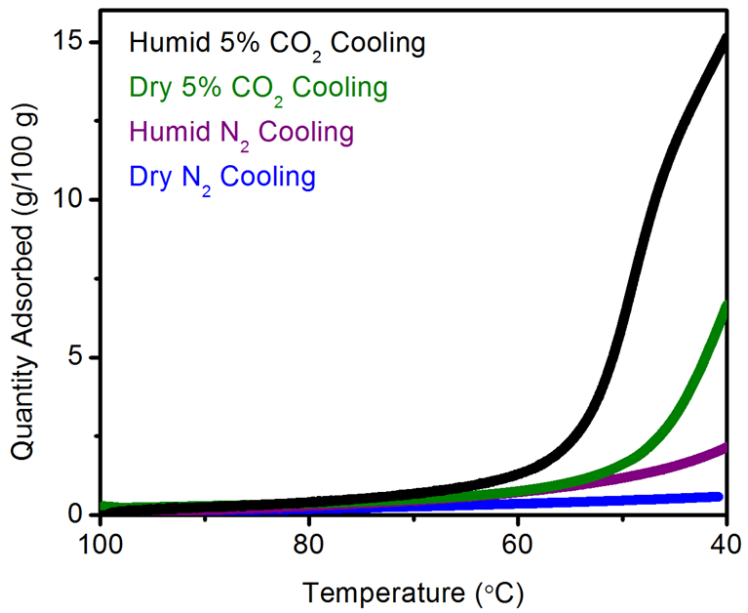

Figure S33. Humid 5% CO_2 in N_2 (black), dry 5% CO_2 in N_2 (green), humid N_2 (purple), and dry N_2 (blue) isobars of dmpn–Mg_2(dobpdc). A ramp rate of 1 °C/min was used.

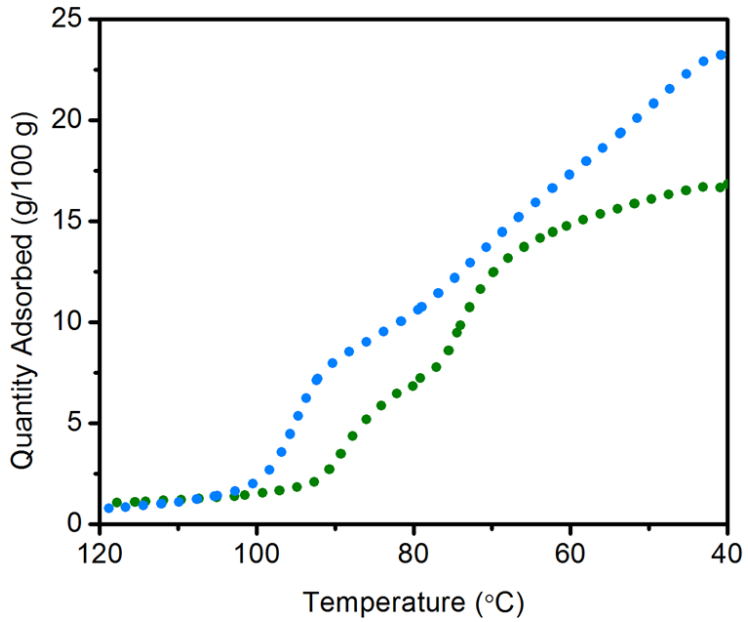

Figure S34. Humid CO_2 (light blue) and dry CO_2 (green) desorption isobars of dmpn–Mg_2(dobpdc), indicating that nearly full desorption of CO_2 and H_2O occurs upon heating to 100 °C. A ramp rate of 1 °C/min was used.

Details of breakthrough measurements. Semi-spherical pellets of dmpn–Mg_2(dobpdc) (approximately 350–700 μm in diameter) were prepared by repeatedly compressing the powdered material between two stainless steel disks and sieving the resulting tablet between 25 and 45 mesh

grids. This process did not have a significant effect on the CO_2 adsorption properties of the adsorbent (Figure S35).

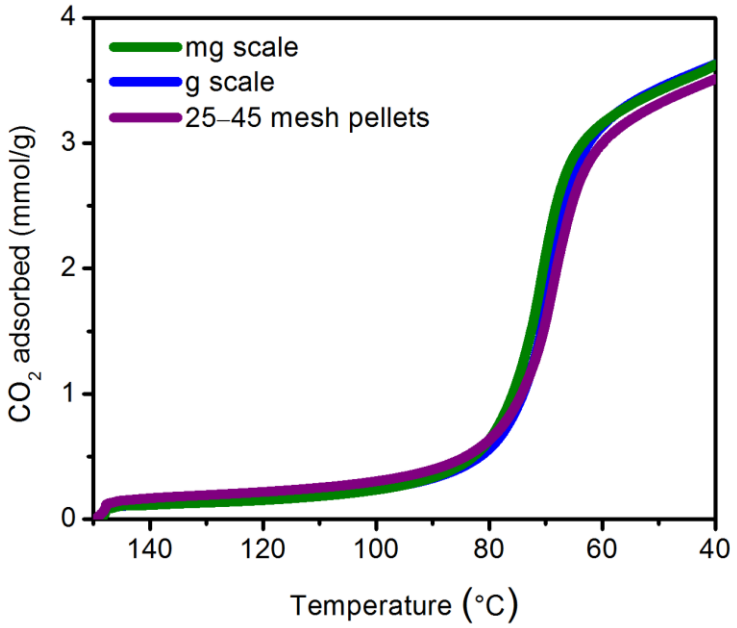

Figure S35. Comparison of the CO_2 isobars of dmpn–Mg_2(dobpdc) prepared on small scale (green) and 5 g scale (blue), and after pelletization on large scale (purple).

A 6″ stainless steel column (0.25″ OD, wall thickness 0.035″) was packed with 0.63 g of activated dmpn–Mg_2(dobpdc) pellets. The final length of packed material was 5.25″, and glass wool was added to the end of the column to secure the pellets. The column was fitted with quarter-turn Swagelok plug valves and attached to a U-shaped piece of 1/8″ stainless steel tubing with VCR fittings and 2 μm fritted stainless steel gaskets. The column inlet was attached to a manifold consisting of 1/8″ copper tubing fed by 4 individual Parker-Porter mass flow controllers. An SRI Instruments 8610V or 8610C GC equipped with a 6′ Haysep-D column and a TCD was used to monitor the breakthrough profile of the effluent at 1 min intervals. The GC was calibrated using a series of pre-mixed, Certified Standard tanks of varying percent CO_2 (5, 10, 15, 20, 30, and 50%) in N_2 purchased from Praxair as well as pure, research-grade CO_2 and N_2. The system deadspace was estimated by measuring the Ar breakthrough time after the system had been pre-equilibrated

under He. A total inlet flow rate of 10 sccm was used for all gases and gas mixtures in both experiments and calibrations. Flow rates were validated using an Agilent ADM200 Universal Flow Meter and were monitored every 0.5 s at the GC outlet over the course of each breakthrough experiment. The material was initially activated at 150 °C under 30 sccm of He flow for 30 min. Subsequent reactivation between breakthrough cycles was performed under 30 sccm of He or Ar flow at 100 °C for 30–60 min.

Dry breakthrough experiments were conducted with the column pre-equilibrated under flowing He. To begin the experiment, He flow to the column was stopped as a flow of 15% CO_2 in N_2 was simultaneously switched from a purge line (to equilibrate the flow rate) to the column inlet. Following complete breakthrough of CO_2, the capacity of each gas (q_i, mmol/g) was determined using the formula:

$$q_i = \left[\frac{Q}{22.414\frac{cc_{STP}}{mmol}}\int_0^t\left(1-\frac{F_i}{F_{0,i}}\right)dt - \varepsilon V\left(\frac{y_i P}{RT}\right)\right]\left(\frac{y_i}{m}\right)$$

where Q is the average total volumetric flow rate in sccm, t is the corrected time in min, F_i is the molar flow rate of species i at time t, $F_{0,i}$ is the inlet molar flow rate of species i, ε is the interparticle void fraction, V is the volume of pelletized adsorbent in cm^3, y_i is the mole fraction of species i, P is the total pressure, R is the universal gas constant, T is the column temperature during the experiment, and m is the mass of adsorbent.

The interparticle void fraction ε is calculated as:

$$\varepsilon = 1 - \frac{\rho_{bulk}}{\rho_{particle}}$$

where ρ_{bulk} is the bulk density in kg/m^3, calculated as m/V, and $\rho_{particle}$ is the particle density in kg/m^3 and is estimated as 1000 kg/m^3. Note that due to the small column size, the term

corresponding to the void volume accounted for less than 0.02% of the total adsorbed gas in a typical experiment.

In all experiments, N_2 breakthrough capacities were within error of zero, where the error was determined by the integrated breakthrough time corresponding to the time resolution set by the GC scan rate (1 min).

For humid breakthrough experiments, a water bubbler was inserted immediately before the column inlet. Critically, the bed was pre-saturated with H_2O using humid He prior to each experiment. *Note that this key step is frequently excluded from humid breakthrough experiments and often leads to erroneous conclusions regarding the CO_2 capacity of adsorbents in the presence of H_2O*. Without pre-saturation of H_2O in the bed, the front of the adsorbent bed will desiccate the incoming stream, and the observed CO_2 breakthrough capacity will correspond simply to the capacity of the remaining dry material for a dry CO_2 mixture. Pre-saturation of the adsorbent with H_2O was confirmed by placing a column of indicating Drierite at the adsorbent column outlet. The Drierite column was removed prior to each humid breakthrough experiment to avoid errors in breakthrough capacity resulting from adsorption of CO_2 by Drierite. It was further necessary to pre-saturate the water bubbler with CO_2 to maintain a constant partial pressure of CO_2 during humid breakthrough experiments. After sealing the column of H_2O-saturated material under He, the simulated flue gas mixture was flowed through the water bubbler to a bypass line fed directly to the GC until equilibration of the CO_2 peak integral was observed (indicating that saturation of the water with CO_2 had occurred). The breakthrough experiment was then begun. Between humid breakthrough cycles, the adsorbent was reactivated under a 30 mL/min flow of humid He for 30–60 min, and pre-saturation with H_2O was again verified using a Drierite column.

The volumetric concentration of water was estimated as 2–3% based on the measured differences between the dry and humid volumetric flow rates. Breakthrough capacities were calculated by subtracting the assumed volumetric flow rate of water in sccm from the total volumetric flow rate prior to integration. Data shown in Figure 7 correspond to the third humid breakthrough cycle.

Additional cycling results.

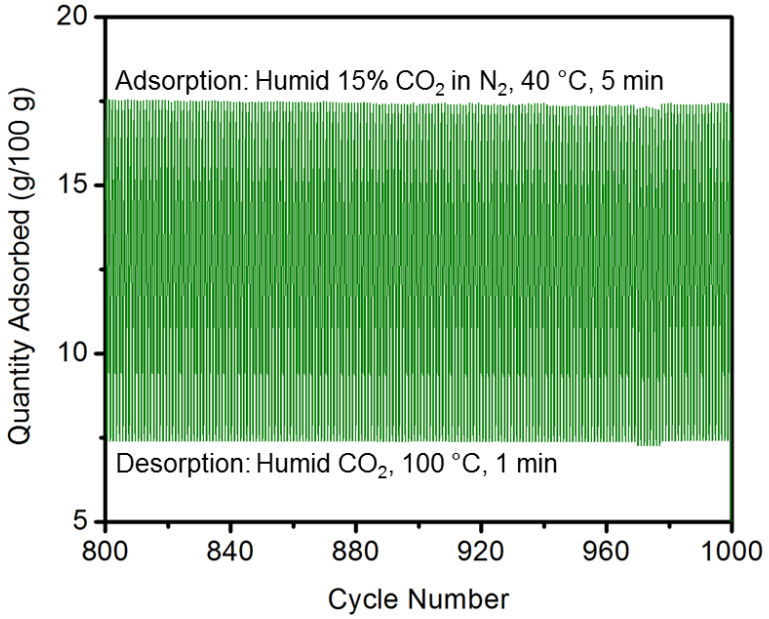

Figure S36. Raw data for the last 200 of 1000 humid adsorption/desorption cycles with dmpn–Mg_2(dobpdc) (Figure 8). Adsorption: humid 15% CO_2 in N_2, 40 °C, 5 min (correspond to maxima). Desorption: humid pure CO_2, 100 °C, 1 min (correspond to minima). The baseline value of 0 g/100 g is defined as the mass after activation under humid 15% CO_2 in N_2 for 20 min at 130 °C prior to the first cycle.

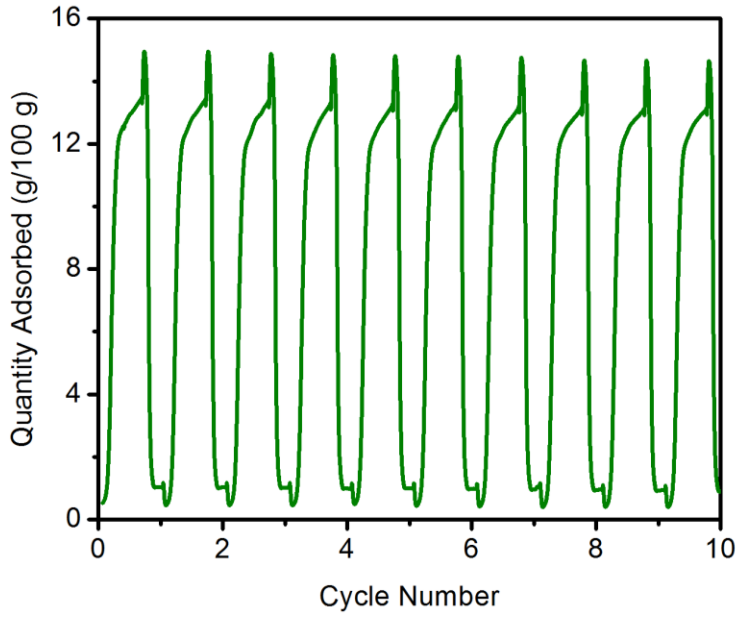

Figure S37. 10 dry adsorption/desorption cycles with dmpn–Mg_2(dobpdc). Adsorption: dry 15% CO_2 in N_2, 40 °C, 10 min; desorption: dry pure CO_2, 100 °C, 5 min. The observed spikes at the maxima are due to increased CO_2 adsorption upon switching the gas stream from 15% CO_2 in N_2 to pure CO_2. Considering the selective adsorption of CO_2 over N_2 in dmpn–Mg_2(dobpdc), the mass changes should correspond almost exclusively to CO_2 adsorption/desorption. The mass change in the final cycle (12.7 g/100 g) corresponds to 2.89 mmol/g if all CO_2, which closely matches the CO_2 capacity of dmpn–Mg_2(dobpdc) (2.91 mmol/g) at 150 mbar and 40 °C from the CO_2 isotherm (Figure 4). The baseline value of 0 g/100 g is defined as the mass after activation under 15% CO_2 in N_2 for 20 min at 130 °C prior to the first cycle.

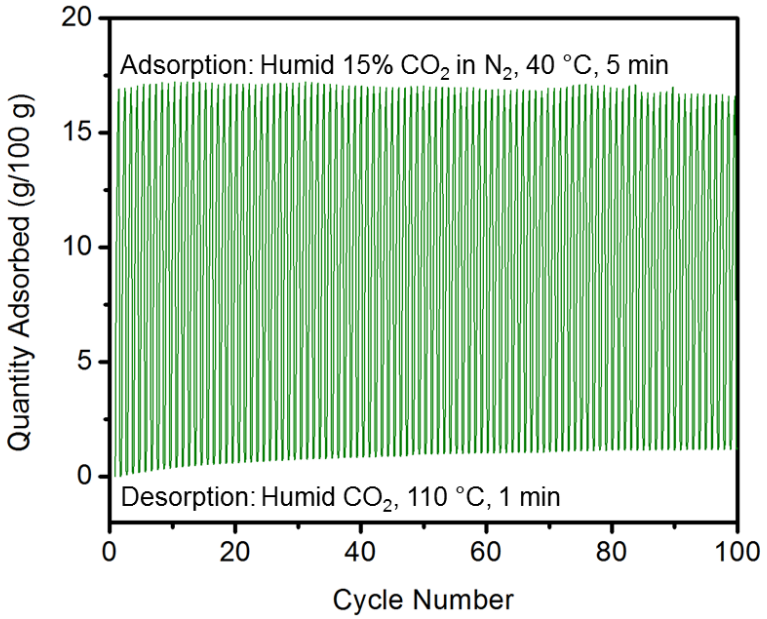

Figure S38. 100 humid adsorption/desorption cycles with dmpn–Mg_2(dobpdc) with desorption at 110 °C. Adsorption: humid 15% CO_2 in N_2, 40 °C, 5 min (correspond to maxima). Desorption: humid pure CO_2, 110 °C, 1 min (correspond to minima). The baseline value of 0 g/100 g is defined as the mass after activation under 15% CO_2 in N_2 for 20 min at 130 °C prior to the first cycle. The diamine loading was found to be 97% after this experiment.

Repeating this cycling experiment with desorption at 120 °C (98%), 130 °C (95%), 140 °C (97%), or 150 °C (94%) resulted in similar profiles over 100 cycles, with high diamine loadings (indicated in parentheses) still observed by ^{1}H NMR upon digestion of the material post-cycling. In addition, a sample of dmpn–Mg_2(dobpdc) held under flowing humid CO_2 at 150 °C for 12 h (to simulate hundreds of adsorption/desorption cycles under humid conditions) retained a high diamine loading after digestion of the material (93%). A similarly high diamine loading was observed upon holding dmpn–Mg_2(dobpdc) under flowing humid CO_2 for 12 h at even higher temperatures, such as 175 °C (93%), 200 °C (89%), and 225 °C (80%), reflecting its excellent thermal stability to diamine loss. At temperatures of 250 °C and above, significant degradation of the diamine and discoloration of the framework was observed.

8. Additional solid-state magic angle spinning ^{13}C NMR spectra and details.

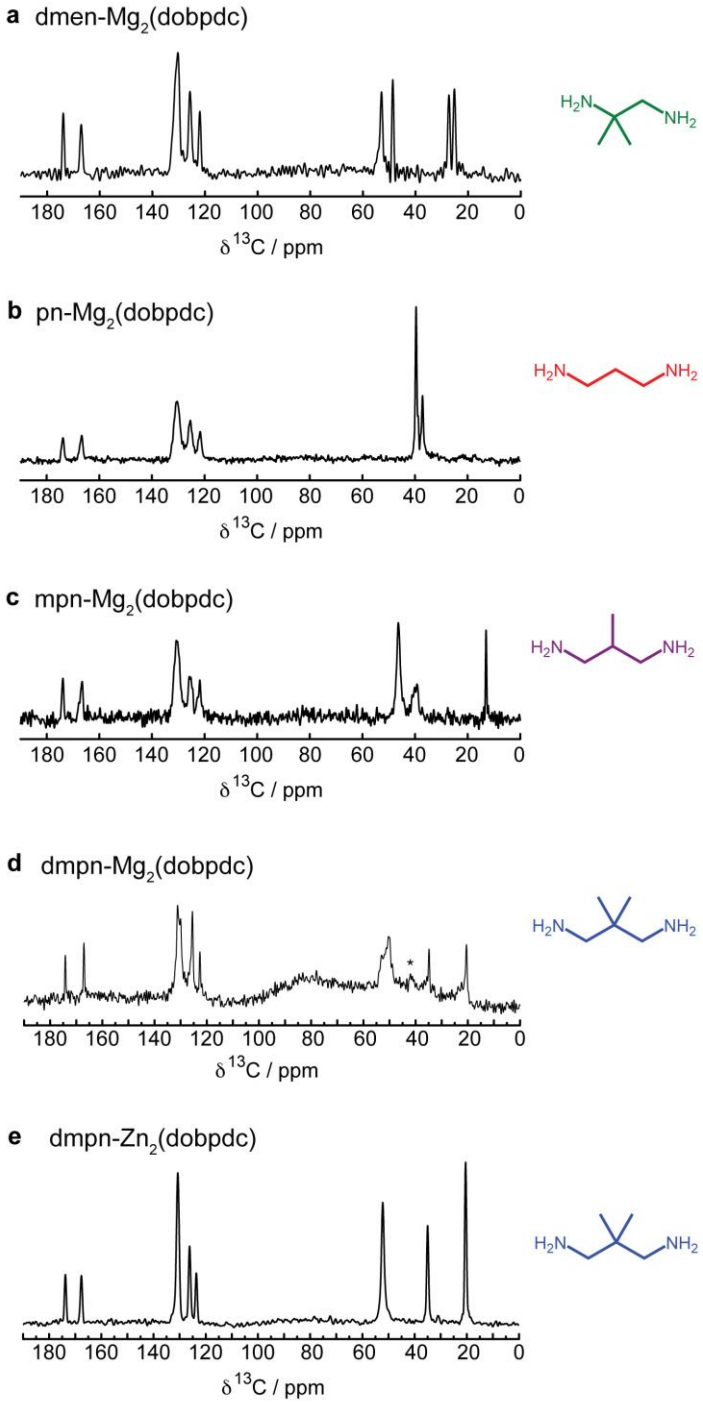

Figure S39. ^{13}C MAS NMR (7.1 T) spectra of activated samples of (a) dmen–, (b) pn–, (c) mpn–, (d) dmpn–Mg_2(dobpdc), and dmpn–Zn_2(dobpdc) in the absence of CO_2. In all cases, the observed resonances can be assigned to the framework (120–180 ppm) or diamine (10–60 ppm). These spectra were collected at ambient temperature.

Details of the dosing apparatus used for the spectra shown in Figures 10–11. Uncapped rotors were evacuated for at least 30 min inside a home-built gas dosing manifold before dosing with $^{13}CO_2$, after which the samples were allowed to equilibrate for 30 min. The rotor was then capped inside the gas manifold using a device similar to one previously reported.[5] A key feature of this manifold is a glass rod that can be maneuvered in and out of the manifold through an O-ring, which allows the rotor to be sealed under various pressures of $^{13}CO_2$. Pressure measurements were made using a capacitance manometer. Ambient temperature was used for dosing which was monitored to be between 23 and 25 °C for all experiments. Typical acquisition times for NMR spectra of $^{13}CO_2$ dosed samples ranged from 30 min to 1 h. It was confirmed by performing NMR experiments as a function of time that the rotor did not significantly leak on the timescale of one acquisition, although gas loss was observed after a period of ~15 h.

NMR calculations. NMR calculations were performed in the CASTEP density functional theory code,[6] using the gauge including projector augmented wave (GIPAW) approach.[7] The PBE (with a generalised gradient approximation) functional was used for the exchange-correlation term,[8] and ultrasoft psuedopotentials were used.[9] All calculations used planewave basis functions with an energy cut-off of 60 Ry, and a *k*-point spacing of 0.06 Å^{-1} was used. These parameters were found to give converged ^{13}C isotropic shielding values to within 0.1 ppm. Calculated isotropic chemical shifts, δ_{iso}, were obtained using; $\delta_{iso} = -(\sigma_{iso} - \sigma_{ref})$, where σ_{iso} is the calculated isotropic shielding,

---

[5] Zhang, W.; Ma, D.; Liu, X.; Liu, X.; Bao, X. *Chem. Commun.* **1999**, 1091.
[6] Clark, S. J.; Segall, M. D.; Pickard, C. J.; Hasnip, P. J.; Probert, M. I. J.; Refson, K. *Z. Krist.* **2005**, *220*, 567.
[7] Pickard, C. J.; Mauri, F. *Phys. Rev. B* **2001**, *63*, 245101.
[8] Perdew, J. P.; Burke, K.; Ernzerhof, M. *Phys. Rev. Lett.* **1996**, *77*, 3865.
[9] Yates, J.; Pickard, C.; Mauri, F. *Phys. Rev. B* **2007**, *76*, 24401.

and σ_{ref} is a reference value. We determined a σ_{ref} value of 170.6 ppm for ^{13}C. This value was the *y*-intercept of a plot of experimental isotropic chemical shift against calculated isotropic chemical shielding for activated dmpn-Zn_2(dobpdc). Geometry optimizations were carried out in CASTEP prior to NMR calculations. For the carbamic acid pair structure of dmpn-Zn_2(dobpdc), the X-ray single crystal structure (Figure 12b) was used as the starting point with the unit cell parameters fixed during geometry optimization. For the ammonium carbamate chain structure, we first constructed a putative model structure in Materials Studio. This was then geometry optimized in CASTEP with the unit cell parameters fixed to those obtained for the pair phase (Figure S40).

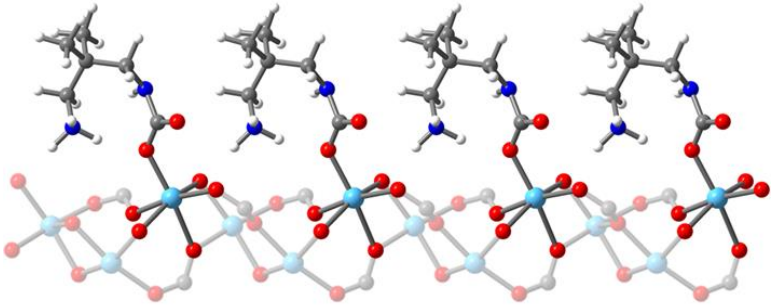

Figure S40. Density functional theory calculated structure of a potential structure for the ammonium carbamate chains of dmpn–Zn_2(dobpdc). The calculated ^{13}C NMR shift of the carbonyl carbon of ammonium carbamate is 165.3 ppm. Light blue, blue, red, gray, and white spheres represent Zn, N, O, C, and H, respectively

9. Activated and CO_2-dosed infrared spectra of diamine-appended metal–organic frameworks.

Dry N_2 attenuated total reflectance IR spectra were obtained by placing activated samples and the IR spectrometer into a N_2-filled glovebag that had been purged of air by three vacuum/N_2 refill cycles. After acquiring dry N_2 IR spectra, the glovebag was placed under vacuum and backilled with CO_2 from a cylinder; this process was repeated three times. The IR spectra were then obtained under an atmosphere of CO_2.

It has been established in the literature that ammonium carbamate and carbamic acid species possess diagnostic C=O stretches (1550–1700 cm^{-1}), and ammonium carbamate species possess an additional diagnostic C–N stretch at 1320 cm^{-1}.[10] Our previous work revealed that diamine-appended variants of Mg_2(dobpdc) that form ammonium carbamate chains possess diagnostic C=O (1650–1700 cm^{-1}) and C–N (1320–1340 cm^{-1}) stretches upon CO_2 adsorption.[1,2]

[10] Didas, S. A.; Sakwa-Novak, M. A.; Foo, G. S.; Sievers, C.; Jones, C. W. *J. Phys. Chem. Lett.* **2014**, *5*, 4194.

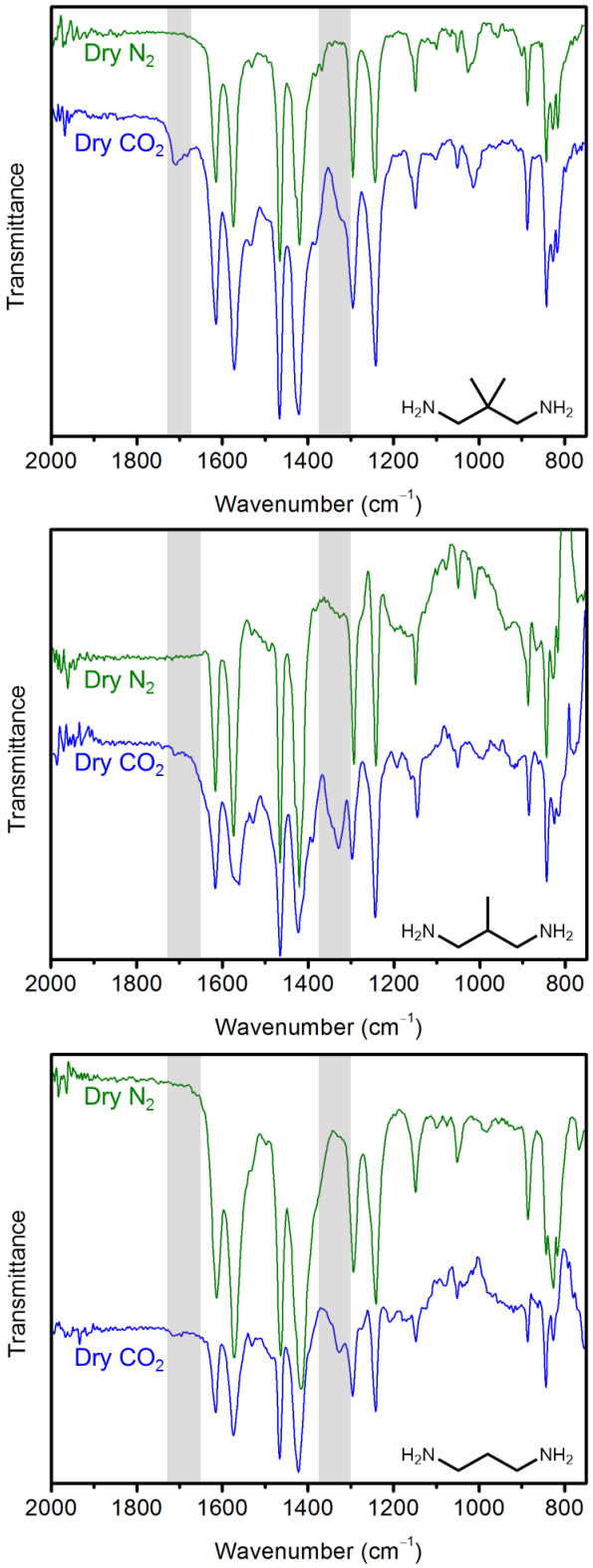

Figure S41. IR spectra of activated dmpn–, mpn–, and pn–Mg_2(dobpdc), under an atmosphere of dry N_2 (green) or dry CO_2 (blue).

The broad and intense peak at 1710 cm^{-1} in the IR spectrum of the CO_2-adsorbed phase of dmpn–Mg_2(dobpdc) corresponds to the C=O stretch of the adsorbed species. While the C=O stretches for the CO_2-adsorbed phases of mpn–Mg_2(dobpdc) and pn–Mg_2(dobpdc) are weaker in intensity, they are located at a similar frequency (1710 cm^{-1} for mpn–Mg_2(dobpdc), 1700 cm^{-1} for pn–Mg_2(dobpdc)). The C–N stretches for CO_2-adsorbed phases of mpn–Mg_2(dobpdc) and pn–Mg_2(dobpdc) are intense and evident at 1330 cm^{-1}; these stretches are indicative of ammonium carbamates.[1,10] The corresponding C–N stretch of the CO_2-adsorbed phase of dmpn–Mg_2(dobpdc) overlaps with the ligand stretch at 1295 cm^{-1} and is evident as a shoulder at 1330 cm^{-1}.

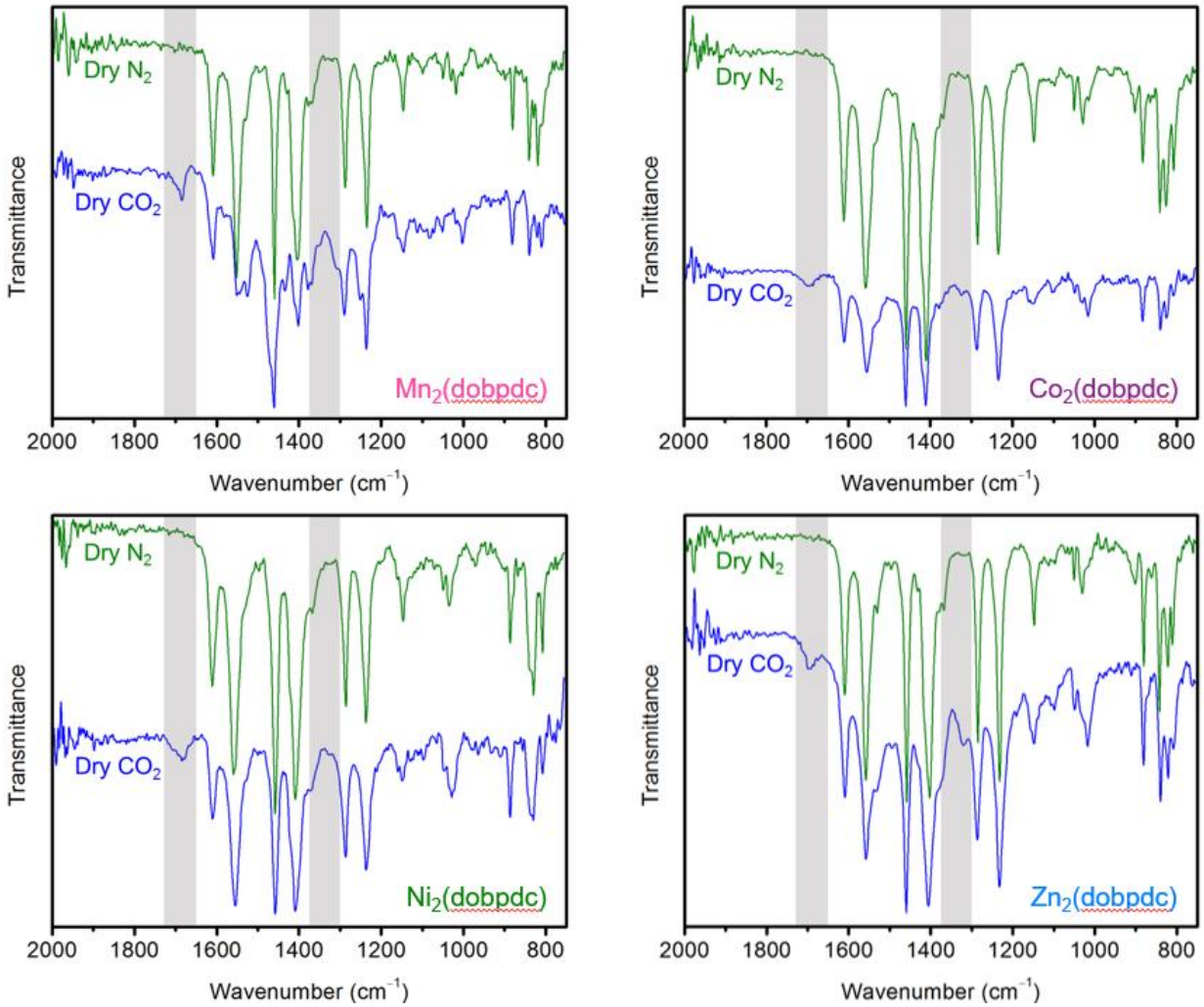

Figure S42. IR spectra of activated dmpn–Mn_2(dobpdc), Co_2(dobpdc), Ni_2(dobpdc), and Zn_2(dobpdc), under an atmosphere of dry N_2 (green) or dry CO_2 (blue).

The C=O stretches for the CO_2-adsorbed phases of dmpn–M_2(dobpdc) variants are at similar frequencies (Mg: 1710 cm^{-1}; Mn: 1690 cm^{-1}; Co: 1700 cm^{-1}; Ni: 1690 cm^{-1}; Zn: 1700 cm^{-1}). The C–N stretches for the CO_2-adsorbed phases of dmpn–Zn_2(dobpdc) (1320 cm^{-1}) and dmpn–Co_2(dobpdc) (1324 cm^{-1}) are similar to those shown in Figure S41, and a shoulder at 1310 cm^{-1} can be observed on the ligand stretch at 1290 cm^{-1} in the IR spectrum for the CO_2-adsorbed phase of dmpn–Mn_2(dobpdc). No C–N stretch was readily apparent when dmpn–Ni_2(dobpdc) was exposed to CO_2, consistent with our previous measurements with *N,N′*-dimethylethynediamine–Ni_2(dobpdc).[1]

10. Powder X-ray diffraction structures of dmpn–Mn_2(dobpdc) and dmpn–Mg_2(dobpdc).

Samples of dmpn–Mn_2(dobpdc) and dmpn–Mg_2(dobpdc) are crystalline and yield characteristic powder diffraction patterns (Figure S43). High-resolution X-ray powder diffraction patterns of the samples were collected with a synchrotron X-ray radiation, at the beamline 17-BM at the Advanced Photon Source at the Argonne National Laboratory. The average wavelength of the X-rays was set to 0.72768 Å. Scattered intensity was recorded by Perkin Elmer α-Si Flat Panel detector. Prior to collecting diffraction data, the samples were activated under flowing N_2 at 130 °C for 30 min, placed into borosilicate glass capillaries of 1 mm diameter (Hilgenberg glass No. 50), activated under dynamic vacuum at 100 °C for 30 min, and flame-sealed. Sample handling was carried out in a glovebox to avoid contact with atmosphere. Diffraction patterns were collected at room temperature and at 100 K. A cold-air blower was used for temperature control with an airflow focused on the borosilicate capillaries. Plastic foil was used to stop formation of ice crystals around the capillaries.

The analysis of the diffraction data (pattern indexing, profile fitting, crystal structure analysis and Rietveld refinement) was performed with the program TOPAS 4.1.[11] Initial data analysis was performed using Pawley fitting[12] of the diffraction patterns collected at 100 K. The fitting was performed using the trigonal space group $P3_121$ and the starting lattice parameters were set as determined by single-crystal X-ray diffraction for dmpn–Zn_2(dobpdc). The structure-less fitting converged quickly, accounting for all of the observed reflections in the patterns. The fitting provided accurate lattice parameters for both samples [a = 21.771(1) Å, c = 7.04(2) and V =

[11] Bruker AXS, Topas, version 4.1. **2007**.
[12] Pawley, G. S. *J. Appl. Cryst.* **1981**, *14*, 357.

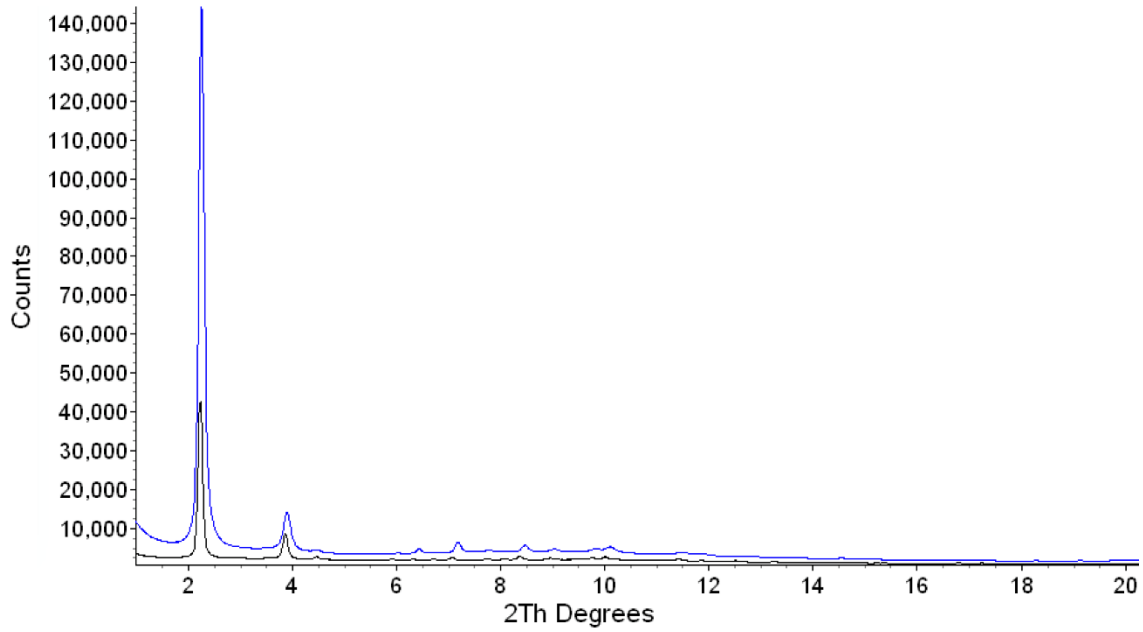

Figure S43. Powder diffraction patterns of dmpn–Mn_2(dobpdc) (blue) and dmpn–Mg_2(dobpdc) (black), respectively. The wavelength of X-ray radiation was set to 0.72768 Å.

2895.7(1) Å^3 for dmpn–Mn_2(dobpdc), and a = 21.624(1) Å, c = 6.93(4) Å and V = 2806.1(1) Å^3 for dmpn–Mg_2(dobpdc)]. Small changes in the unit cell parameters were observed at room temperature. Profile parameters (strain, stress, instrumental parameters, applied simple axial model, zero-error shift) and background (Chebychev polynomial of 10th order) were refined together with the values for the lattice parameters.

These values, as determined by the Pawley fitting, were used as initial values for the Rietveld analysis[13] of dmpn–Mn_2(dobpdc), which exhibited higher crystallinity than the corresponding Mg sample (Figure S43). Assuming similarity to the dmpn–Zn_2(dobpdc) crystal structure, the fractional coordinates for all atoms were taken from the Zn analogue. Due to pronounced thermal motion of the amines, together with the conformational disorder and the lower resolution compared to the single-crystal measurements, unconstrained refinement was not possible. Instead, the

[13] Rietveld, H. M. *J. Appl. Crystallogr*. **1969**, *2*, 65.

fractional coordinates were kept fixed during the Rietveld refinement, with all of the remaining parameters set free. The thermal displacement factors for the amine atoms reached relatively high values (*beq* ~ 10) indicating a pronounced thermal motion. Preferred orientation of the powder particles was detected along the [**001**] direction, and successfully treated with a single March–Dollase parameter (which resulted in a decrease of the R_{wp} figure-of-merit for less than 2%). The final Rietveld plot is given in Figure S44. The unit cell parameters were refined to a = 21.773(2) Å, c = 7.06(1) and V = 2895.7(2) Å^3. As can be seen from the difference curve and evidenced by the figures-of-merit (R_{exp} = 1.172 %, R_{wp} = 6.49 %, R_{Brgg} = 1.22 %), the Rietveld refinement confirms that dmpn–Mn_2(dobpdc) is isostructural to dmpn–Zn_2(dobpdc).

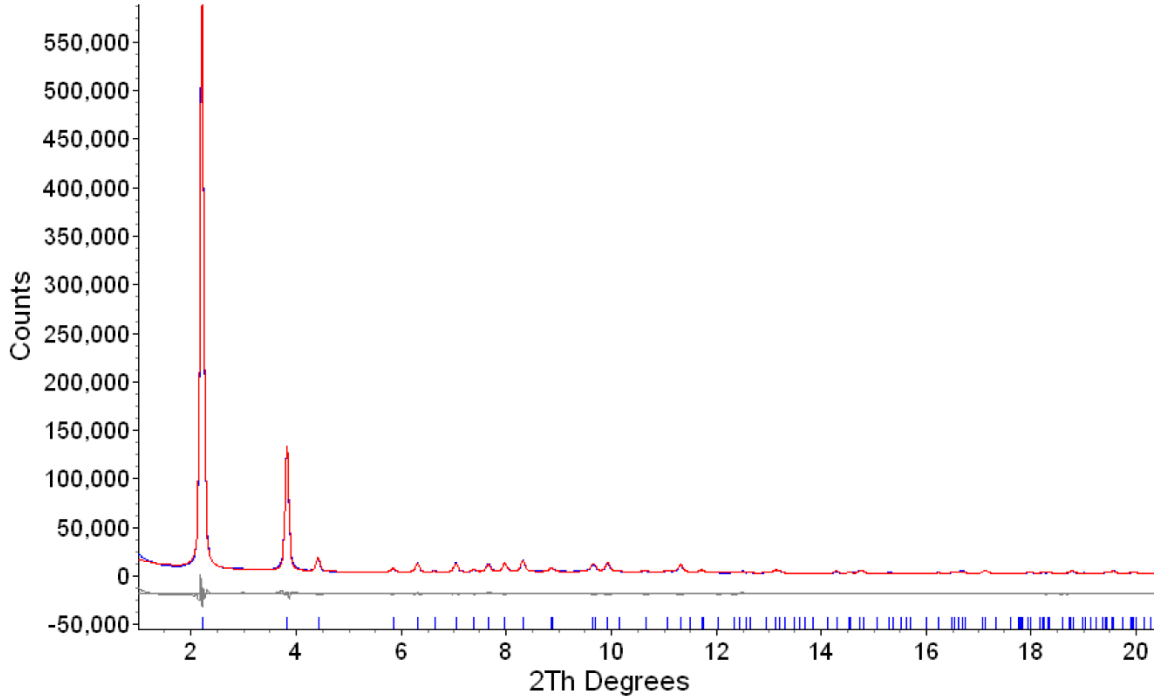

Figure S44. Rietveld refinement plot of dmpn–Mn_2(dobpdc) collected at 100 K. Measured scattered intensity is presented with a blue line, the best fit with a red line, and the corresponding difference plot with a gray line. The Bragg reflections are indicated with blue bars.

11. Single-crystal synthesis and X-ray diffraction structures of diamine-appended Zn_2(dobpdc) analogues.

Single crystals of Zn_2(dobpdc) and diamine-appended analogues were prepared following the previously reported procedure.[2] A slight modification to this procedure was made for the single-crystals of dmpn-appended Zn_2(dobpdc) without CO_2, for which diamine appending was performed in diethyl ether rather than toluene (though appending the diamine in either solvent was subsequently found to produce equivalent X-ray diffraction structures). For single-crystal structures of CO_2-bound dmen– and dmpn–Zn_2(dobpdc), the supernatant of the diamine-appended crystals was first exchanged three times with approximately 3 mL of fresh toluene after heating at 60 °C for 1 h per wash. The supernatant was then exchanged three times with approximately 3 mL of hexanes at room temperature. The crystals were then transferred by pipette to a glass measurement tube sealed with a Micromeritics *TranSeal* and heated *in vacuo* for 1 h at 100 °C. The sample was then transferred air-free to the analysis port of the instrument and dosed with 1100 mbar of CO_2. The tube was sealed under CO_2, removed from the manifold, and stored over dry ice for a minimum of 1 h. The single crystals were coated with Paratone oil immediately after the tube was opened, and a single crystal was rapidly mounted and flash-cooled to 100 K using an Oxford Cryosystems cryostream prior to data collection.

All single-crystal X-ray diffraction data were collected at Beamline 11.3.1 at the Advanced Light Source, Lawrence Berkeley National Laboratory, using synchrotron radiation (λ = 0.6888, 0.7749, or 0.8856 Å; see Table S4) and a Bruker AXS D8 diffractometer equipped with a Bruker PHOTON 100 CMOS detector. Single-crystal structures of diamine-appended Zn_2(dobpdc) frameworks were collected at 100 K using an Oxford Cryosystems cryostream 700 plus. All crystals were refined as inversions twins in space group $P3_221$ or $P3_121$ based on Flack parameter values near 0.5. Raw data were corrected for Lorentz and polarization effects using Bruker AXS

SAINT[14] software and were corrected for absorption using SADABS.[15] The structures were solved using SHELXT[16] and refined using SHELXL[17] operated in the OLEX2[18] interface. Thermal parameters were refined anisotropically for all non-hydrogen atoms. All hydrogen atoms were placed geometrically and refined using a riding model.

For toluene-solvated structures of dmen- (Figure S47) and mpn-appended Zn_2(dobpdc) (Figure S46) without CO_2, the diamine was found to be disordered over two positions. For diethyl ether-solvated Zn_2(dobpdc) single crystals appended with dmpn (Figure 12a), only a single conformation could be found, but the low overall occupancy of the diamine (0.65(2)) suggested that other disordered conformations may be present that could not be modeled. For all diamine-appended analogues, the reported formula and refinement were fixed to reflect the freely refined occupancy of each diamine. However, the nitrogen atom bound to the Zn(II) sites (N1) was fixed at full occupancy to account for solvent or water where the diamine was absent.

For CO_2-dosed crystals of dmen–Zn_2(dobpdc), formation of ammonium carbamate chains was observed and refined to an occupancy of 0.488(13) (Figure S47). Residual unreacted diamine was also refined in the structure at an occupancy of 0.379(17), leading to an overall formula of Zn_2(dobpdc)(dmen)$_{0.98}$(dmen–CO_2)$_{0.76}$. For CO_2-dosed crystals of dmpn–Zn_2(dobpdc), formation of carbamic acid pairs diagonally bridging the *a*-*b* plane was observed and refined to an occupancy of 0.387(10) (Figure 12b and Figure 13). Residual unreacted diamine was also identified in this structure and refined to an occupancy of 0.325(12), resulting in an overall formula of

---

[14] *SAINT, APEX2, and APEX3 Software for CCD Diffractometers*; Bruker Analytical X-ray Systems Inc.: Madison, WI, USA, 2014.
[15] Sheldrick, G. M. *SADABS*; University of Göttingen, Germany.
[16] Sheldrick, G. M. *Acta Crystallogr. Sect. Found. Adv.* **2015**, *71*, 3.
[17] Sheldrick, G. M. *Acta Crystallogr. Sect. C Struct. Chem.* **2015**, *71*, 3.
[18] Dolomanov, O. V.; Bourhis, L. J.; Gildea, R. J.; Howard, J. a. K.; Puschmann, H. *J. Appl. Crystallogr.* **2009**, *42*, 339.

Zn_2(dobpdc)(dmpn)$_{0.65}$(dmpn–CO_2)$_{0.77}$. For the CO_2-reacted structures, the occupancy of the bound carbamate oxygen atom (dmen) or nitrogen atom (dmpn) was fixed at 1 to account for CO_2, solvent, or water bound on sites where the diamine was absent, but the reported formula reflects the freely refined diamine and CO_2 content alone. Displacement parameter restraints (RIGU and SIMU) and distance restraints (SADI, and in select cases DFIX) were necessary to model the disorder of the free diamines, the ammonium carbamate chains (dmen), and the carbamic acid pairs (dmpn).

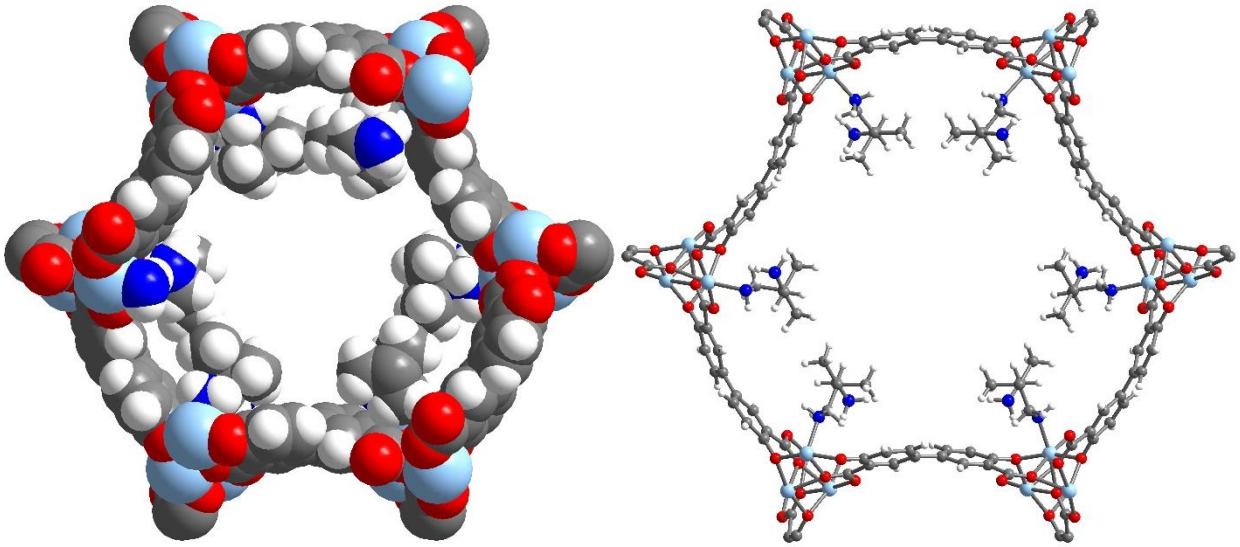

Figure S45. Space-filling (left) and ball-and-stick (right) views of one pore of diethyl ether-solvated dmpn–Zn_2(dobpdc) in the absence of CO_2 at 100 K. Light blue, blue, red, gray, and white spheres represent Zn, N, O, C, and H, respectively

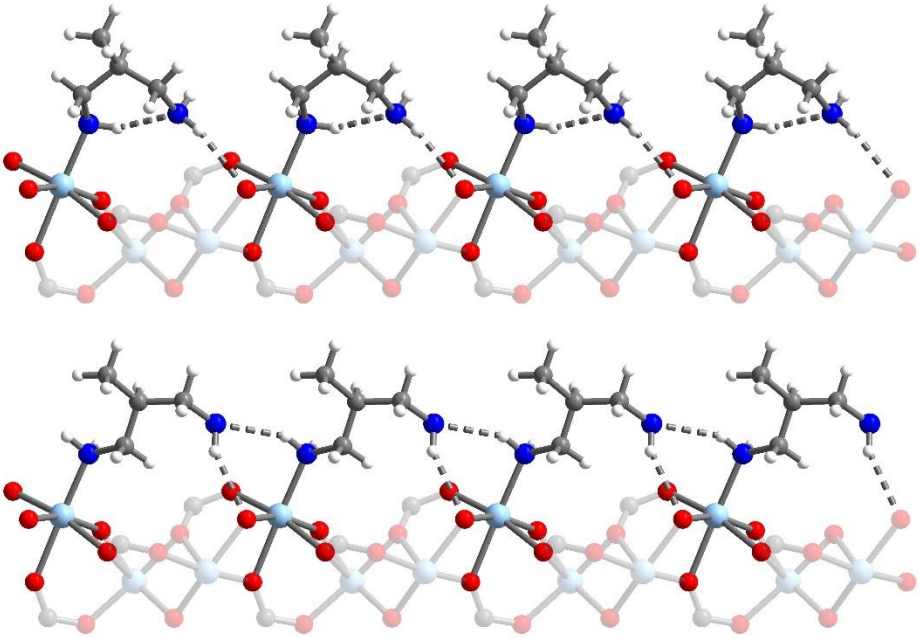

Figure S46. Single-crystal X-ray diffraction structures of the major (57.1(13)% occupancy, top) and minor (30.8(13)% occupancy, bottom) conformers of toluene-solvated mpn–Zn_2(dobpdc) at 100 K. The minor conformer is nearly identical to that observed for dmpn–Zn_2(dobpdc) (Figure 12a). Light blue, blue, red, gray, and white spheres represent Zn, N, O, C, and H, respectively

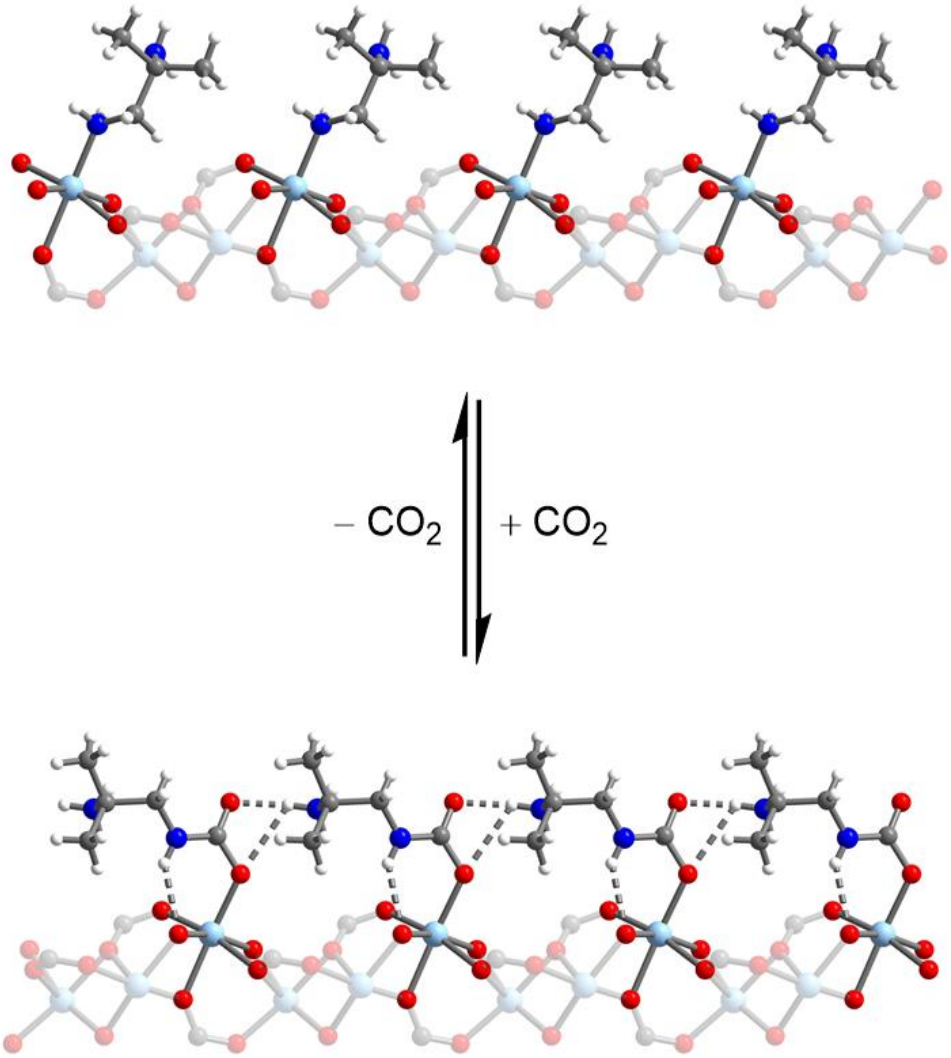

Figure S47. Single-crystal X-ray diffraction structures of dmen–Zn_2(dobpdc) in the absence (major conformer, 49.4(14)% occupancy, top) and presence (bottom) of CO_2, confirming the formation of ammonium carbamate chains upon adsorption of CO_2. Structures were obtained at 100 K. Light blue, blue, red, gray, and white spheres represent Zn, N, O, C, and H, respectively

Table S4. Crystallographic Data

	$Zn_2(dobpdc)(dmen)_{1.61}\cdot(H_2O)_{0.70}$	$Zn_2(dobpdc)(dmen)_{0.98}(dmen–CO_2)_{0.76}$	$Zn_2(dobpdc)(mpn)_{1.76}(C_7H_8)_{0.62}$	$Zn_2(dobpdc)(dmpn)_{1.3}$	$Zn_2(dobpdc)(dmpn)_{0.65}(dmpn–CO_2)_{0.77}$
Formula	$C_{20.44}H_{26.72}N_{3.22}O_{6.7}Zn_2$	$C_{21.91}H_{26.82}N_{3.47}O_{7.95}Zn_2$	$C_{25.39}H_{32.07}N_{3.52}O_6Zn_2$	$C_{20.5}H_{24.2}N_{2.6}O_6Zn_2$	$C_{21.89}H_{25.94}N_{2.85}O_{7.55}Zn_2$
Temperature (K)	100(2)	100(2)	100(2)	100(2)	100(2)
Crystal System	Trigonal	Trigonal	Trigonal	Trigonal	Trigonal
Space Group	$P3_121$	$P3_121$	$P3_121$	$P3_121$	$P3_221$
a, b, c (Å)	21.4217(8), 21.4217(8), 6.8386(3)	21.3008(9), 21.3008(9), 6.8770(3)	21.527(2), 21.527(2), 6.8199(8)	21.4559(7), 21.4559(7), 6.7954(3)	21.6530(11), 21.6530(11), 6.7873(4)
α, β, γ (°)	90, 90, 120	90, 90, 120	90, 90, 120	90, 90, 120	90, 90, 120
V, (Å^3)	2717.7(2)	2702.2(3)	2737.0(7)	2709.2(2)	2755.9(3)
Z	3	3	3	3	3
Radiation, λ (Å)	Synchrotron, 0.8856	Synchrotron, 0.7749	Synchrotron, 0.7749	Synchrotron, 0.7749	Synchrotron, 0.6888
2Θ Range for Data Collection (°)	4.738 to 72.388	4.170 to 67.200	6.304 to 70.556	4.780 to 61.258	4.210 to 61.908
Completeness to 2Θ	99.8% (2Θ = 64.194°)	99.9% (2Θ = 55.412°)	99.6% (2Θ = 55.412°)	99.9% (2Θ = 55.412°)	99.9% (2Θ = 48.822°)
Data / Restraints / Parameters	4495 / 72 / 214	5513 / 181 / 240	6333 / 184 / 256	4317 / 114 / 167	6402 / 215 / 231
Goodness of Fit on F^2	1.106	1.215	1.238	1.303	1.205
$R1^a$, $wR2^b$ (I>2σ(I))	0.0511, 0.1359	0.0728, 0.1762	0.0574, 0.1414	0.0955, 0.2221	0.0585, 0.1332
$R1^a$, $wR2^b$ (all data)	0.0588, 0.1401	0.0750, 0.1775	0.0583, 0.1418	0.1000, 0.2240	0.0652, 0.1358
Largest Diff. Peak and Hole (e Å^{-3})	1.026 and -1.107	1.571 and -2.196	1.117 and -2.818	1.191 and -3.317	0.838 and -1.821

$^aR_1 = \sum||F_o| - |F_c||/\sum|F_o|$. $^bwR_2 = \{\sum[w(F_o^2 - F_c^2)^2]/\sum[w(F_o^2)^2]\}^{1/2}$.